Structure and Mechanics of the Spasmoneme, a Biological Spring within the Protozoan *Vorticella convallaria*

by

Danielle Cook France

B.S. Biomedical Engineering
Washington University, 2001

SUBMITTED TO THE DEPARTMENT OF BIOLOGICAL ENGINEERING IN PARTIAL FULFILLMENT OF THE REQUIREMENTS FOR THE DEGREE OF

DOCTOR OF PHILOSOPHY IN BIOLOGICAL ENGINEERING

AT THE
MASSACHUSETTS INSTITUTE OF TECHNOLOGY

June 2007

MASSACHUSETTS INSTITUTE OF TECHNOLOGY
AUG 0 2 2007
LIBRARIES

© Massachusetts Institute of Technology. All rights reserved.

ARCHIVES

Signature of Author: _____
Department of Biological Engineering
May 24, 2007

Certified by _____
Paul T. Matsudaira
Professor of Biology and Biological Engineering
Thesis Supervisor

Accepted by _____
Alan J. Grodzinsky
Professor of Electrical, Mechanical, and Biological Engineering
Chair, Course XX Graduate Program Committee

Advisory Committee

Accepted by _____

Peter T. C. So
Professor of Mechanical and Biological Engineering
Committee Chair

Accepted by _____

Alexander van Oudenaarden
Associate Professor of Physics

Structure and Mechanics of the Spasmoneme, a Biological Spring within the Protozoan *Vorticella convallaria*

by

Danielle Cook France

Submitted to the Department of Biological Engineering on the 24th of May, 2007
in Partial Fulfillment of the Requirements for
the Degree of Doctor of Philosophy in Biological Engineering

ABSTRACT

Molecular springs have recently emerged as the basis for the fastest and most powerful movements at the cellular level in biology. The spasmoneme of the protozoan, *Vorticella convallaria*, is a model molecular spring, relying on energy stored in protein interactions to power contraction over a few hundred micrometers in a few milliseconds. While basic characteristics of *Vorticella* contraction are known, the underlying biochemical mechanism is unclear. The studies outlined here define and measure key parameters of spasmoneme performance which enable discrimination between proposed movement schemes and identification of new model parameters.

Recent work has classified the spasmoneme as a power-limited machine (Upadhyaya, Baraban et al. 2007), where increases in viscous load correspond to decreases in velocity; in this work the maxiumum load at minimum velocity (the stall force), is measured. Work done by the stalk in contraction is shown to be dependent on its fractional change in length. This energy dependence arises from the basic underlying mechanism, and a major goal of this thesis was to characterize that mechanism by imaging the underlying structure. In the case of the *Vorticella* spasmoneme, imaging methods like birefringence imaging and electron microscopy, which do not require preexisting knowledge of protein identity, are particularly helpful. High-speed measurements of live *Vorticella* movements show the persistence of birefringence throughout the contraction-extension cycle. Orientation-independent measurements taken with an LC Pol-Scope show strong birefringence with slow axis parallel to the stalk long axis in both the extended and contracted states. Quantification of textural differences between the two states reveals slight structural disordering upon contraction. Transmission electron micrographs show a correlation between nanometer-scale filaments and the distribution of birefringence within the spasmoneme. As a whole these measurements indicate that any model of the contractile mechanism should consider the interactions of filamentous proteins at high concentrations which lead to longitudinal microscopic alignment in both the extended and contracted states. Implications of a proposed model are considered in the context of how they may be tested *in vitro* with purified constituent and homologous recombinant proteins, and how they can inform the development of biomimetic, nanoscale actuators.

Thesis Supervisor: Paul Matsudaira
Title: Professor of Biology and Biological Engineering

Biographical Note

Danielle Cook attended Washington University in St. Louis, Missouri, on a Langsdorf Fellowship, earning her Bachelor of Science in Biomedical Engineering in 2001. While at Washington, she played on the varsity women's soccer team as well as co-founded a women's club soccer team. On the academic side, she served as treasurer of the Missouri Beta chapter of the Tau Beta Pi engineering honor society, and had the opportunity to perform summer research at the National Institutes of Health and the Mayo Clinic. Before and immediately after graduation, she worked with Dr. Sandor Kovacs at the Washington University Medical School in the field of cardiac biophysics. For the following year, she continued in the cardiac field with research on blood flow at the University of New South Wales in Sydney, Australia.

Danielle returned to the United States to begin graduate studies at MIT in the Biological Engineering (BE) Division in the fall of 2002. In the spring of 2003, she joined the Whitehead Institute laboratory of Professor Paul Matsudaira, focusing on new techniques for deciphering the contractile mechanism of the protozoan, *Vorticella convallaria.* In the summer of 2004, she completed the Physiology Course at the Marine Biological Laboratory in Woods Hole. From the experience grew a fruitful collaboration with members of the ADLC program at the MBL, namely Dr. Shinya Inoué, Dr. Michael Shribak, and Dr. Rudolph Oldenbourg.

In the spring of 2005, Danielle married Ryan France, and changed her name to Danielle Cook France. She was also awarded a Poitras Fellowship for the 2005 – 2006 academic year. While at MIT, Danielle was involved as a teaching assistant in two undergraduate biomechanics courses, 20.310 and 3.052. She also served on the BE Student Board, helping to organize a student-run lecture series and the 2006 annual retreat. However, perhaps her greatest service to BE was in captaining two intramural soccer championship teams.

Acknowledgements

I have received wonderful support throughout my thesis from several sources, not least of which is the Biological Engineering Department, which has absolutely been the best place at MIT for me to learn and grow as a scientist.

I would first like to thank my advisor, Paul Matsudaira, for the unqualified support that he has given me to pursue my own ideas from the very beginning of my thesis, and for teaching me to see the importance of my own work and how to effectively communicate it to other people. I would also like to thank my committee members, Alexander van Oudenaarden and Peter So. Along with L Mahadevan, they have given me outstanding and thoughtful advice over the past four years.

There have also been many other people who have helped along the way with this project. First of all, I'd like to thank all the members of the Matsudaira lab. We come from many different backgrounds and have very diverse projects, but I have always received great interest and advice from everyone along the way. Valeriya Baru was particularly patient in showing me the ropes of the wet lab and the biochemistry of *Vorticella*. Jonathan Tejada was a UROP who had a major role in the stall force project, although he also worked for quite some time on many of my (somewhat naïve) ideas at the protein level. A few other members of the lab were always helpful in letting me bounce ideas off them, including (but certainly not limited to) Alec Robertson, Barney Tam, Winston Timp, and Mike Murrell.

I am deeply indebted to what became my second lab, the ADLC group at the Marine Biological Laboratory at Woods Hole. The technical expertise in the lab is unparalleled, and it is because of Shinya Inoué, Mike Shribak, Rudolf Oldenbourg, and Grant Harris that I was able to produce the beautiful images shown in this thesis.

A major part of my decision in coming to MIT was excitement to work with students of the high caliber that I had met during my interviews. But, I had no idea how rewarding it would be to share both working and social lives with the amazing people who have been going through this process at the same time as me. I'd like to thank all of my classmates and I look forward to keeping them as friends and colleagues in the future.

Many thanks are due to my parents, Diane and Timothy Cook, who taught me from an early age that it was not acceptable to give up on understanding any concept before I had seriously applied myself to learning it. Thanks to my dad for all the physics lessons at the dinner table, and thanks to my mom, the ever-patient math teacher, for being the first person to show me step-by-step reasoning through tough problems.

Most of all I would like to thank my husband, Ryan. He has encouraged me every step of the way, while still reminding me of all the wonderful things in life outside of science. I can honestly say that I would not have made it this far without his love, support, and genuine interest in my work.

Structure and Mechanics of the Spasmoneme, a Biological Spring within the Protozoan *Vorticella convallaria*

Table of Contents

1. Introduction ..... page 9

1.1. Cell motility and molecular springs
1.2. *Vorticella* motility
1.2.1. Known structure
Contraction sequence with overlaid structural schematic: **Figure 1.1**
1.2.2. Early biomechanical work
1.2.3. Modeling spasmoneme mechanics
1.2.4. Calcium signal propagation
1.2.5. Recent work
1.3. Homologous systems
1.4. Proposed models
1.5. Specific aims of this thesis
1.6. Methods: *Vorticella* cell culture

2. Force production and energy dissipation ..... page 26

2.1. Introduction and background
2.1.1. Maximum power limitation
2.2. Contraction under centrifugal force
2.2.1. Methods
2.2.2. Results: *Live* Vorticella *can produce > 200 nNs of force during contraction.*
Live *Vorticella* in the CPM: **Figure 2.1**
Slowing of extension times in the CPM: **Figure 2.2**
2.3. Contraction under pipette loading
2.3.1. Methods
Pipette calibration data: **Figure 2.3**
2.3.2. Results: *The maximum stall force for live* Vorticella *is ~ 180 nNs.*
Contraction sequence under pipette loading: **Figure 2.4**
Pipette displacement data: **Figure 2.5**
Average displacements, velocities, and forces versus time: **Figure 2.6**
Maximum velocities and forces versus length: **Figure 2.7**

2.4. Energetics of contraction
Power and energy for different loading conditions: **Figure 2.8**
2.5. Conclusion: *Work performed by the spasmoneme during contraction is dependent on the amount it is allowed to shorten.*

3. Imaging for structural parameters ..... page 59

3.1. Introduction and background
3.1.1. Polarized light microscopy
3.2. Polarized light imaging of live cell contraction
3.2.1. Methods
3.2.2. Results: *Birefringence is retained throughout the cycle of contraction and re-extension.*
Contraction and extension sequences in the ULM: **Figure 3.1**
3.3. Orientation-independent polarized light imaging of static states
3.3.1. Methods
LC Pol-Scope image formation: **Figure 3.2**
3.3.2. Results: *Birefringence from both spasmoneme and sheath aligns with the stalk long axis in extension and contraction.*
Extended and contracted stalks in the LC Pol-Scope: **Figure 3.3**
3D projection of contracted stalk: **Figure 3.4**
Evidence for bâtonnet retardance: **Figure 3.5**
3.4. Ordering parameters
3.4.1. Methods
3.4.2. Results: *93% ordering in the extended state drops to 77% upon contraction.*
Slow axis angle histograms: **Figure 3.6**
3.5. Transmission electron microscopy
3.5.1. Methods
3.5.2. Results: *A fibrous substructure correlates with textural variation in birefringence images.*
TEM images of extended stalks: **Figure 3.7**
TEM images of contracted stalks: **Figure 3.8**
3.6. Conclusion: *Slight change in ordering indicates which models fit and which can be discarded.*

4. Biochemistry and testable hypotheses ..... page 87

4.1. Introduction and background

4.2. Capabilities of centrin alone
4.2.1. Methods
4.2.2. Results: *Centrin does not form fibers on its own.*
Centrin aggregates in high calcium: **Figure 4.1**
4.3. Search for an Sfi1p homolog in *Tetrahymena thermophila*
4.3.1. Methods and results: Tetrahymena *possesses a protein which has a similar sequence to yeast Sfi1p and colocalizes with centrin.*
Discovered homolog sequence from Tetrahymena genome: **Figure 4.2**
Colocalization of Sfi1p homolog and centrin: **Figure 4.3**
4.4. Testable hypotheses and future work
4.4.1. A proposed model for *Vorticella's* contractile mechanism
Surface charge of centrin-Sfi1p complexes: **Figure 4.4**
Proposed model schematic: **Figure 4.5**
4.4.2. Future Work
4.4.2.1. Testing the model i*n vitro* with proteins
Proposed experimental framework: order vs. concentration: **Figure 4.6**
4.4.2.2. Testing the model in nanoscale or microscale devices
Coaxial electrospinning: **Figure 4.7**
4.5. Conclusion: *Groundwork has been laid for testing image-derived hypotheses via* in vitro *protein systems.*

5. Conclusions ..... page 114

5.1. Important parameters for modeling and future work
5.2. Wider relevance

References ..... page 118

Appendix I: Electrospinning

Centrin in electrospun fibers: **Figure AI.1**

Appendix II: Sequences

1

Introduction

1.1. Cell motility and molecular springs

Nature has evolved a number of ingenious movement mechanisms, techniques by which cells use their internal biochemical machinery to change shape, generate force, or move into new environments. The mechanisms of cellular motility known to date fall into three major categories: motor proteins, polymerization reactions, and molecular springs. The first two categories are well understood, and have been explored in many different contexts, ranging from muscle (the motor protein myosin interacts with actin) to the brain (neurotransmitters are actively transported by the motor protein kinesin moving along microtubules) (Vale and Milligan 2000) to parasitic invasion (actin polymerization machinery is hijacked to propel *Listeria*) (Gouin, Welch et al. 2005). Movements falling into the third category, molecular springs, have long fascinated scientists but are only now becoming very well understood at the molecular level.

The general unifying principle behind the classification of molecular springs is the ability of a protein assembly to store energy in such a way that can be released quickly and powerfully after being chemically "unlatched". The acrosomal bundle of the horseshoe crab sperm cell, a stiff cross-linked bundle of actin fibers, has been established as an archetypal example of a molecular

spring. The actin bundle is stored at the base of the sperm cell in a twisted coil; as calcium binds to the actin cross-linking protein, scruin, the scruin molecule changes conformation. Such a conformation change propagates along the bundle as the entire length gets extruded from the sperm cell in order to penetrate and fertilize the horseshoe crab egg. The 60 μm long bundle extends in only five seconds, a speed which is significantly faster than most polymerization or motor protein-driven movements (Shin, Mahadevan et al. 2003; Shin, Tam et al. 2007). The acrosome demonstrates how energy stored in the conformation of the twisted bundle can be quickly released by calcium binding to generate fast and powerful cellular movements. Similar principles are believed to underlie the even faster and more powerful contractile mechanism of the protozoan *Vorticella convallaria.*

Table 1.1 outlines the performance characteristics of several different biological engines, ranging from single proteins on the nanometer size scale to larger motile assemblies on the cellular scale. A typical passenger car engine is also included to illustrate the scaling concept of specific power, which divides the power output of an engine by its mass. In terms of specific power, molecular engines are more powerful than the cellular level structures into which they are assembled to produce larger-scale movements. For example, the specific power of myosin II is two orders of magnitude greater than the specific power of striated muscle, even though striated muscle, as a microscale assembly, is able to generate significantly more force. By the same token, although the *Vorticella* spasmoneme is a microscale assembly three to five orders of magnitude larger than the molecular engines listed, its specific power is only one to two orders of magnitude lower.

Table 1.1 Performance characteristics of biological engines (Mahadevan and Matsudaira 2000).

Engine	Velocity [$\mu m\ s^{-1}$]	Force [dynes]	Specific power [$erg\ s^{-1}\ g^{-1}$]
k_BT (thermal energy)	-	4×10^{-7} dyne·nm	
Actin polymerization	1	1×10^{-6}	1×10^{9}
Microtubule polymerization	0.02	4×10^{-7}	5×10^{8}
Myosin II	4	1×10^{-6}	2×10^{8}
Kinesin	1	6×10^{-7}	7×10^{7}
Vorticellid spasmoneme	**8×10^{4}**	**1×10^{-3}**	**4×10^{7}**
Typical passenger car engine			3×10^{6}
Striated muscle			2×10^{6}
Bacterial flagellar motor	100 Hz	4.5×10^{-11} dyne·cm	1×10^{6}
Thyone acrosomal reaction	6-9	5×10^{-4}	1×10^{5}
Limulus acrosomal reaction	10	1×10^{-6}	1×10^{4}
Eukaryotic flagellum			3×10^{2}
Mitotic spindle	2	1×10^{-5}	

Understanding the molecular spring mechanism in *Vorticella* is important for understanding the mechanisms of homologous proteins and structures in other eukaryotes ranging from the excision of flagellar roots in green algae (Salisbury 1984; Salisbury 1998) to the duplication of the microtubule organizing center in budding yeast (Li, Sandercock et al. 2006). On a broader level, however, biological springs represent highly evolved actuators that use nanoscale structures (proteins) to generate remarkable speeds and power at the microscale. Engineered systems, such as stimulus-sensitive polymer gel actuators, are several orders of magnitude slower when manufactured at microscale dimensions* (van der Linden, Herber et al. 2003). The engineering of nanoscale actuators could benefit greatly from precise definitions of how biology has been able to evolve spring-like movement mechanisms. While any type of cell motility could potentially become useful inspiration for engineered nanoscale actuators, the fact that *Vorticella's* movement mechanism is powered by a simple change in chemical gradient makes it

* van der Linden *et al.* give a time constant of three seconds for swelling of a one μm spherical hydrogel actuator.

more amenable to mechanochemical machinery than motor protein or polymerization mechanisms which consume a nonrenewable fuel source (ATP)[†].

This thesis builds on the important studies in the literature of *Vorticella*, its relatives, and its constituent components that have all begun to shed some light on the underlying phenomena driving *Vorticella* motility.

1.2. *Vorticella* motility

The first recorded sighting of *Vorticella* dates back to the 17th century, when van Leeuwenhoek placed a drop of pond water under his newly invented light microscope. (van Leeuwenhoek 1676). He described first the ciliary beating by which *Vorticella* feeds on bacteria, and then the contraction of the stalk:

> *In structure these little animals were fashioned like a bell, and at the round opening they made such a stir, that the particles in the water thereabout were set in motion thereby. . . And though I must have seen quite 20 of these little animals on their long tails alongside one another very gently moving, with outstretched bodies and straightened-out tails; yet in an instant, as it were, they pulled their bodies and their tails together, and no sooner had they contracted their bodies and tails, than they began to stick their tails out again very leisurely, and stayed thus some time continuing their gentle motion: which sight I found mightily diverting.* (Waggoner quoting van Leeuwenhoek 1996)

[†] ATP = adenosine tri-phospate.
The same is true of the acrosome of the horseshoe crab sperm cell, which is also activated by calcium. However, the acrosome is slower than *Vorticella* and it is not known if its length change in response to calcium is reversible.

We now know that the contraction van Leeuwenhoek described is complete in a matter of milliseconds [Figure 1.1], while the "leisurely" extension which follows lasts around one second. It is also now known that the mechanism of *Vorticella* motility must be fundamentally distinct from paradigmatic types of cell motility driven by motor proteins or polymerization reactions. However, the exact molecular mechanism by which *Vorticella* is able to produce such remarkable movement remains unclear.

Vorticella is a single-cell eukaryotic organism, a member of the family of ciliated protozoa which are found in fresh and salt water, in independent, parasitic, and in colonial forms. The cell body can exist in a freely swimming (telotroch) form which, upon finding a suitable attachment substrate, secretes the materials to grow a stalk and convert to sessile form (the form pictured in Figure 1.1). Reproduction is by asexual budding and the occasional sexual conjugation; conversion of a newly budded cell or one dissatisfied with its sessile environment to the telotroch form is accomplished by the beating of a distal ring of cilia whose beating (in conjunction with powerful contractions of the cell body) can break the attachment between the cell body and the stalk. *Vorticella* subsists on ingestion of bacteria via its oral opening, which is circled by another ring of cilia (Buhse and Clamp 2001).

1.2.1. Known structure

The *Vorticella* stalk consists of a large contractile organelle, the spasmoneme, enclosed in a plasma membrane continuous with the cell body membrane. Early observations with the transmission electron microscope revealed hundreds of filaments in the contracted spasmoneme; each filament is roughly 2-4 nm in diameter but with unknown protein composition. These filaments are interspersed with tubules which are roughly 50 nm in diameter with ~ 250 nm

spacing. Adjacent to the spasmoneme and within the membrane are membranous sacs believed to be the source of Ca^{2+} for contraction in live cells, as well as numerous mitochondria. Outside the plasma membrane is a thick extracellular sheath, punctuated by bundled filaments (bâtonnets) arranged helically along the length (Amos 1972; Allen 1973).

Coiling of the stalk involves the mechanical interplay of at least three different elements – the spasmoneme, which actively contracts inside a sheath consisting primarily of a matrix of tiny fibers (the fibrillar matrix) that is stiffened by rod-like bundles of filaments (the bâtonnets). The composition of these extracellular fibers, or whether they are made of the same material, is not known. The spasmoneme runs through the sheath as a left-handed helix, apparently attached to the sheath along its length[‡], while the bâtonnets run as a right-handed helix, always located on the opposite side of the sheath from the spasmoneme. As the stalk shortens, the spasmoneme takes the shorter inside path through the coil while its extended elliptical cross-section becomes more circular. The bâtonnets remain on the outside of the coil (which does not change contour length between extension and contraction), corresponding to the areas of the sheath undergoing the least compression (Amos 1972), and indicating that the bâtonnets define the least deformable part of the sheath and stalk. The cell body also rotates at the end of contraction; this indicates relaxation of some strain stored in the spasmoneme, which must itself twist during the course of contraction.

The major protein component of the stalk was identified in the late 1970s by Routledge, who was the first to run stalk proteins on an SDS gel and identify the major (40-60% of dry weight) 20 kilodalton component, which he termed spasmin. Spasmin demonstrated a slowed anodal

[‡] This is based on observations that local spasmoneme contractions, for example, those caused by local calcium electrospray, induce local bending (Ochiai *et al.*, 1983).

electrophoretic mobility upon binding Ca^{2+}, and is negatively charged at neutral pH ($4.7 < pI < 4.8$) (Routledge 1978). Based on the fibrous structure seen in TEM images (Amos 1972; Allen 1973), and lack of success in coercing centrin to form fibers on its own (Salisbury 1998), components additional to centrin have been hypothesized. Asai's group undertook a study of chemical modifications to the spasmoneme, finding that modifications to tryptophan, methionine, and histidine residues can abolish contractility even though those residues are rare in the centrin sequence (Kono, Ochiai et al. 1997). The observation that centrins are soluble, while the spasmoneme as a whole is not, also supports the hypothesis that other proteins, likely of high molecular weight, are involved in forming the structure of the contractile mechanism of the spasmoneme.

1.2.2. Early biomechanical work

Although Hoffman-Berling was the first to examine *Vorticella* from a mechanical point of view in the 1950s (Hoffmann-Berling 1953), most early biomechanical work was conducted at the University of Cambridge by WB Amos, LM Routledge, T Weis-Fogh, and colleagues on glycerinated *Vorticella* collected from ponds & streams. In 1971 Amos defined the Ca^{2+} threshold*: *Vorticella* remain extended at less than 10^{-8} M free Ca^{2+} and fully contract at greater than 10^{-6} M free Ca^{2+}. From this he was able to calculate the chemical potential energy, E, available to the spasmoneme operating around this threshold and compare it to the amount of work, W, done in moving the cell body against Stokes' drag in a fluid; i.e.,

* Yokoyama and Asai later measured the contractility of the spasmoneme induced by various other divalent metal and lanthanide ions, finding that Mg^{2+} does not effectively induce contraction, although Nd^{3+} and Eu^{3+} induce length vs. concentration curves very similar to those induced by Ca^{2+}. Ca^{2+}, Nd^{3+}, and Eu^{3+} have very similar ionic radii (0.99, 1.04, and 0.98 angstroms, respectively) (Yokoyama 1987).

$$E = RT\ln(\frac{a_1}{a_2}) \quad \text{and} \quad W = 6\pi r\eta\upsilon d \quad \text{where}$$

R = gas constant
T = temperature
η = viscosity of water
a_1 = high $[Ca^{2+}]$
r = cell body radius
υ = velocity
d = distance contracted
a_2 = low $[Ca^{2+}]$

The amount of Ca^{2+} that must be bound is then W/E = 6.9 x 10^{-17} g ions/spasmoneme, a small, feasible quantity (Amos 1971). The same group used microprobe measurements to verify that the spasmoneme does bind that much Ca^{2+}, and that each Ca^{2+}-binding molecule captured between 1.4 and 2.1 ions (Routledge, Amos et al. 1975). These calculations led to the suggestion that the mechanochemical cycle of the spasmoneme be used to produce work in a biologically-based machine (Weis-Fogh and Amos 1972).

A Japanese research group headed by Hiroshi Asai picked up mechanical experiments on *Vorticella* in the late 1970s, providing the first curves showing stalk length and tension developed as a function of pCa, with a kind of hysteresis showing between contraction (increasing pCa) and extension (decreasing pCa) curves. They concurrently described the Ca^{2+} binding process by treating it as a cooperative binding equilibrium; i.e., for the binding of *n* moles of Ca^{2+} to an extended spasmoneme element S, bringing about the contraction of that element, the following equations apply:

$$[S] + n[Ca^{2+}] \leftrightarrow [S{\cdot}Ca^{2+}{}_n]$$

$$K = [S][Ca^{2+}]^n / [S{\cdot}Ca^{2+}{}_n] = K_m{}^n$$

K_m is the dissociation constant in molar units; *n* is known as the Hill parameter and is indicative of the number of cooperative binding sites on the spasmoneme element. K_m and n were different

values depending on whether the stalk was contracting or extending, and whether length or isometric tension was measured. For fractional length vs. pCa, $K_{m,ext}$ = 0.35 μM, n_{ext} = 2, and $K_{m,contr}$= 0.75 μM, n_{contr} = 2 (Ochiai, Asai et al. 1979). For isometric tension vs. pCa, $K_{m,ext}$ = 0.16 μM, n_{ext} = 2.5, and $K_{m,contr}$= 0.40 μM, n_{contr} = 3.2 (Moriyama, Yasuda et al. 1996). One reason for the difference in values is that the method of measuring isometric tension eliminates the passive effects of the extracellular sheath, which in the past has been proposed to be anything from a slightly assisting element to completely responsible for extension. Mechanics of the sheath have yet to be definitively investigated.

1.2.3. Modeling spasmoneme mechanics

In the Asai group, Moriyama has undertaken two studies attempting to model spasmoneme mechanics. One of these proposed that the spasmoneme behaves like a rubber, and measured the volume change of the spasmoneme upon contraction along with tension-extension relationships of spasmonemes in EGTA and Ca^{2+}. Applying the theory of rubber elasticity, they found that the number of segments in a "chain" of contracted spasmoneme was >100, indicating its random jumbled configuration. The number of segments in a chain of extended spasmoneme was 3.3, indicating that such chains would be almost straight. According to the model, the total number of chains and cross-links was unchanged by the Ca^{2+} concentration, indicating that Ca^{2+} induces contraction via folding of chains and not drastic changes in chain structure (Moriyama, Okamoto et al. 1999).

The second Moriyama modeling study observed the contraction of live cells and modeled it as an over damped spring (Moriyama, Hiyama et al. 1998). The model fits contraction velocity data well after an initial acceleration period of 2-3 milliseconds; however, recent experiments which

observed the viscosity dependence of the contraction force and velocity show that the simple spring model cannot fully describe the contraction mechanism.

These recent experiments, conducted by Arpita Upadhyaya and others at MIT, put cells through solutions of increasing viscosity, thereby probing the dynamics of the stalk under higher loads. Interestingly, it was found that given greater loads, *Vorticella* exerts larger forces but at lower speeds. The product of force and velocity, power, was found to be independent of solution viscosity (Upadhyaya, Baraban et al. 2007).

1.2.4. Calcium signal propagation

Another long-standing question involving *Vorticella* contraction is the origin of the contraction impulse. Due to the high speed of contraction (8 cm/s) and the mechanosensitivity of the cell body[§], many investigators have proposed that a mechanically triggered electrical signal originates in the cell body and travels down the stalk, depolarizing membranes and releasing calcium along the way. Shiono and Naitoh measured such membrane depolarization in the cell body and found that cell body contraction actually precedes depolarization of the cell membrane, and following that, the stalk coils (Shiono and Naitoh 1997). The implications of such a sequence of events are that the cell body contraction is a response to mechanical perturbation and is able to depolarize the cell membrane with the stress induced by its drastic shape change. That depolarization could then travel through the cell body-stalk junction and into the stalk, becoming the trigger for calcium release to the contractile proteins within the spasmoneme.

An alternative mechanism to the electrical impulse trigger is calcium-induced calcium release (CICR). Katoh and Naitoh investigated CICR in *Vorticella* by subjecting cells to various drugs

[§] *Vorticella* can be induced to contract by simply poking the cell body (Katoh and Naitoh, 1992).

known to affect calcium release in muscle cells. They found that contraction in live cells could be achieved by addition of caffeine, which induces Ca^{2+} release from the sarcoplasmic reticulum in muscle cells, while it could be inhibited by addition or procaine or ruthenium red, which inhibit CICR in muscle cells. Furthermore, live cells injected with ruthenium red, then Ca^{2+}, yielded the same degree of contraction vs. pCa curve as Triton-X 100 extracted cells; this showed that when the proposed CICR mechanism was inhibited, contraction proceeded similarly as when extracellular calcium only was provided to the spasmoneme via diffusion (Katoh and Naitoh 1994). These experiments presented a good argument for the feasibility of CICR in *Vorticella* contraction. However, Upadhyaya's recent work also addressed signal propagation, measuring the signal wavefront by placing beads along the *Vorticella* stalk and measuring their relative movement. Measured this way, the wave of onset of movement travels from the cell body down the stalk at about 14.9 cm/s (Upadhyaya, Baraban et al. 2007). This is much faster than the speeds seen in CICR which are generally around 100 μm/s (Keizer, Smith et al. 1998).

1.2.5. Recent work

The spasmin molecule first described by Routledge has been investigated in much more detail by Suzanne McCutcheon and other members of the Buhse laboratory at the University of Illinois at Chicago. It turns out that there are seven similar calcium binding molecules within *Vorticella* – one is spasmin and the other six are members of the centrin family (McCutcheon and Buhse 2005). Centrins are 20 kilodalton calcium binding proteins with four EF hands each; they are similar in structure to calmodulin. The N-termini of centrins differentiate them from calmodulins as well as from each other (Wiech, Geier et al. 1996).

Immunofluorescence work by Valeriya Baru in the Matsudaira lab has verified that spasmin, centrin 4, and centrin 5 are found in the *Vorticella* stalk. The significance of slight differences seen in localization is under investigation in the Buhse group via immunoelectron microscopy (McCutcheon and Buhse 2005).

1.3. Homologous systems

Centrins, the major calcium-binding proteins found in the spasmoneme, are found in a vast range of eukaryotic cells. Several protozoa have already been highlighted as exhibiting centrin-based Ca^{2+}-dependent motility; these include *Vorticella* and its close relatives *Carchesium* and *Zoothamnium*, *Stentor*, *Eudiplodinium*, and *Acantharia* (Huang and Pitelka 1973; Febvre 1981; David and Vigues 1994). *Vorticella* remains the most remarkable example of centrin-based movement, closely followed by *Stentor*, and as a result they have been most studied. Centrin was discovered by JL Salisbury in 1984 as a component of the striated flagellar roots of the green alga *Tetraselmis striata*, which also contract in response to Ca^{2+} (Salisbury 1984).

Centrins are also found associated with the microtubule-organizing center (MTOC) of the eukaryotic cell and are critical for cell division (Kilmartin 2003). Recent work in budding yeast has uncovered a binding partner to yeast centrin (cdc31). This sequence of this protein, Sfi1p, consists of twenty-one 33-mer conserved repeats evenly spaced over 946 amino acids [see Figure 4.2 for repeat logos]. Each repeat is able to bind a molecule of centrin. Sfi1p homologs exist in several different organisms, including fungi and humans; each of these homologs retains the conserved repeat structure and many of them can bind centrins from other organisms (Kilmartin 2003; Li, Sandercock et al. 2006).

1.4. Proposed models

Feasible models, which have been proposed by various past investigators but not definitively tested, include an electrostatic entropic spring (Mahadevan and Matsudaira 2000), a cross-linked rubber-like polymer network (Moriyama, Okamoto et al. 1999), and a fiber that coils actively due to conformational changes in centrin upon binding Ca^{2+} (Salisbury 2004).

The electrostatic entropic spring model, which was proposed for *Vorticella* as well as for muscle, states that the extended state is stabilized by electrostatics while the contracted state is stabilized by entropy (Hoffmann-Berling 1953). Fibrous elements within the stalk are negatively charged, causing them to be held apart by electrostatic repulsion in the extended state. As calcium ions flow into the stalk, the charges are neutralized and the fibrous elements are driven by entropy to collapse. As calcium is pumped away after contraction, the stalk extends, again due to electrostatics.

Two pieces of evidence provided major support for the electrostatic entropic spring model. In the 1970s, Brad Amos and colleagues examined the stalk with polarized light and saw a strong birefringence signal which disappeared when the cell contracted (Amos 1971). This was considered an order-to-disorder transition that could support the entropic portion of the model. The net negative charge on spasmin (Routledge 1978) was also evidence for the electrostatic mechanism of the model.

Despite its attractiveness as a model, there were a few inconsistencies within the electrostatic entropic spring model formulation. Most problematic was that the fibrous spasmoneme substructure seen by TEM in contracted cells could apparently not be birefringent, since birefringence was lost upon contraction. While it could be possible that the fibers might not have strong birefringence, or that their birefringence might be masked by some other effect, there was

no apparent structure that could account for the birefringence seen in the extended state**. Another sticking point of the model was the specificity seen for Ca^{2+} over other charged ions. Monovalent salts might be expected to screen charges on the charged proteins making up the spasmoneme, thereby inducing the same collapse as induced by calcium. However, high ionic strengths do not cause or affect contraction (Amos, Routledge et al. 1975). Other multivalent ions can cause contraction; the most effective of these, Eu^{3+} and Tb^{3+}, have ionic radii very close to that of Ca^{2+} (Yokoyama and Asai 1987).

The cross-linked rubber model follows the same reasoning and parameters of the entropic spring model, but specifies that the constituent subunits are flexible long-chain polymers (Moriyama, Okamoto et al. 1999). The electrostatic entropic spring model can work for either flexible long-chain polymers or semi-rigid rods.

The coiling fiber model was first proposed in *Stentor* (Huang and Pitelka 1973) but has been recently advanced for contraction of centrin-containing filaments by Salisbury (Salisbury 2004). The 3-4 nm myoneme filaments in *Stentor* appear to change to tubular 10-12 nm filaments with 3-4 nm wall thickness upon contraction (Huang and Pitelka 1973). Salisbury proposed that the filaments are made of Sfi1p decorated by centrin; conformational changes within the centrin molecule upon binding calcium would induce torsion in the Sfi1p backbone, causing the whole fibrous complex to coil. Such shortening of each spasmoneme subunit would lead to affine shortening of the spasmoneme overall.

** Amos and Allen did not obtain good TEM images of extended cells because the cells invariably collapsed upon exposure to fixative.

1.5. Specific aims of this thesis

The picture that emerges from past work is one of a spring-like mechanism, powered specifically by Ca^{2+}, and having a fibrous substructure. The mechanism is sequentially activated by a traveling calcium wave which is in turn triggered by some unknown mechanism. The major protein component is a calcium-binding protein and is therefore likely to be a reactive element; however it does not appear capable of serving as the structural fibrous element.

While important basic structural elements are known, the exact structure of the contractile mechanism, and how it changes from the extended to the contracted state, has yet to be rigorously identified. No significant correlation has been made between the fibrous substructure seen by electron microscopy and the cellular-level movement. The capabilities of the live cell have not been fully characterized. The various models which have been proposed are still speculative and contain some inconsistencies.

With these open questions in mind, the major aims for this thesis can be outlined. First, the full capabilities of the cell were examined; in particular, a stall force was obtained and considered in the context of the energetics of contraction [Chapter 2]. Second, rigorous imaging of the underlying structure was undertaken with improved methods in polarization and transmission electron microscopy [Chapter 3]. Finally, explorations into the interactions of constituent proteins were undertaken [Chapter 4]. In short, data from cellular-level imaging studies and dynamics of the real-time contraction constrain the parameters of a proposed model for the movement mechanism. That model, which implicates concentration-dependent interactions of centrin filaments, is ready to be tested on the protein level using recombinant yeast homologs to the *Vorticella* proteins.

1.6. Methods: *Vorticella* cell culture

The following methods were used to obtain samples for all live cell experiments. *Vorticella* cultures obtained from Suzanne McCutcheon and Howard Buhse (Vacchiano, Kut et al. 1991) were maintained in the lab via weekly feedings of 500 mL of boiled wheat grass medium [PINES International, Inc., Lawrence, KS] in 4 L Erlenmeyer flasks. When required for experiments, freely swimming cells were poured into Petri dishes containing a substrate for attachment – this substrate was usually a #1½ glass cover slip. Before any observations, cover slips were generally rinsed with sterile spring water [Poland Spring, Wilkes Barre, PA] and then constructed into the relevant slide or chamber for observation.

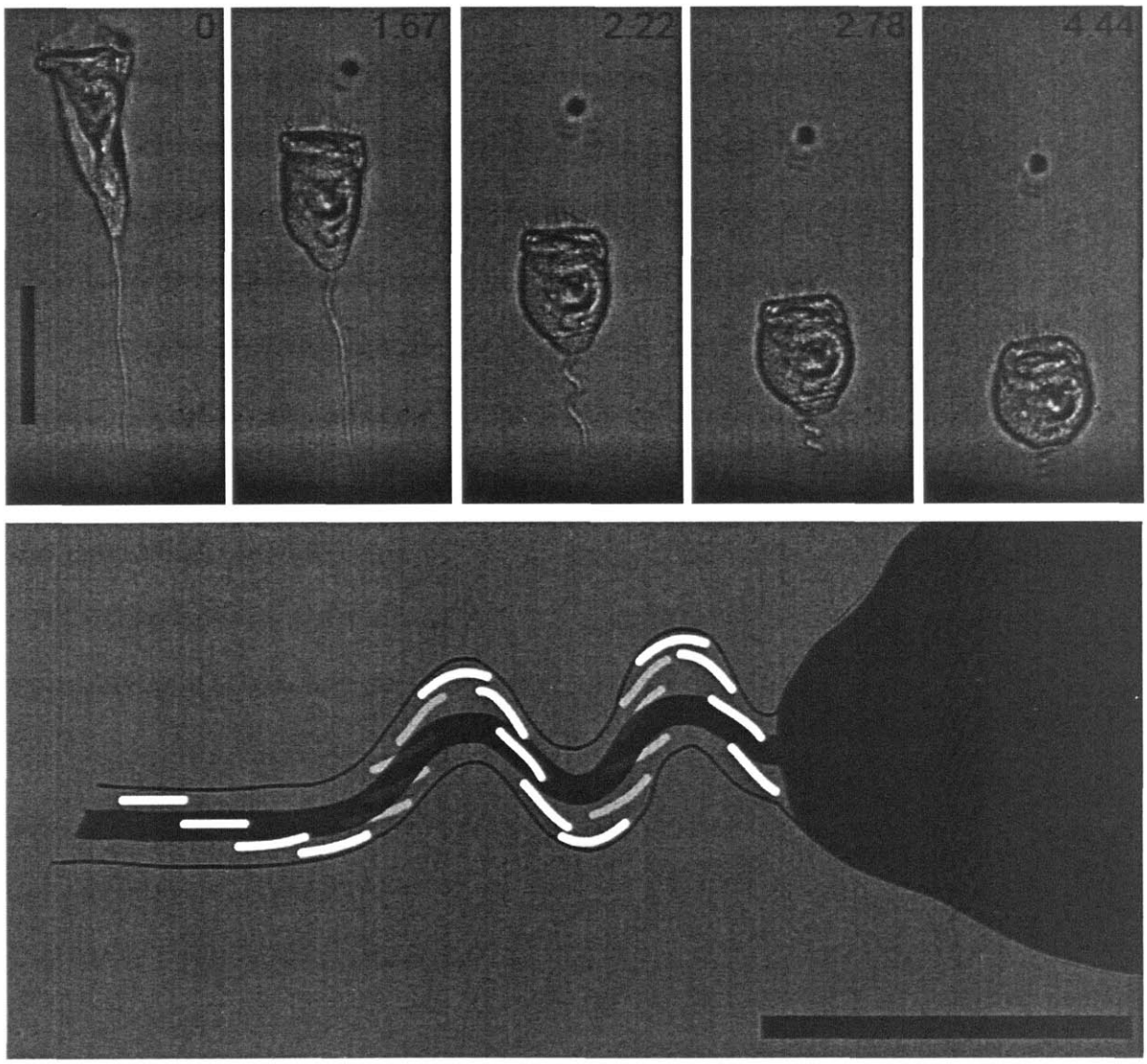

Figure 1.1 **(top)** Time sequence of live *Vorticella* contraction in spring water. Taken with DIC optics at 40X and 10000 frames per second. Time from the start of contraction is shown for each frame in milliseconds. Scale bar = 50 μm. **(bottom)** Schematic showing structures of the *Vorticella* stalk in mid-contraction. The spasmoneme runs as a left-handed helix within the extracellular sheath, which is punctuated with stiffening proteins, called bâtonnets (white rods) arranged in a right-handed helix. Scale bar = 25 μm.

2

Force production and energy dissipation

2.1. Introduction and background

Although *Vorticella* contraction is one of the fastest and most powerful movements witnessed on the microscopic scale, the maximum capabilities of the *Vorticella* stalk in terms of force and power production have yet to be defined. The best way to explore *Vorticella*'s capabilities is to subject the contraction to an additional load. However, imposition of a load on the microscopic scale is not a trivial matter and each different method of imposing load has its own constraints and implications for interpretation of the cell's behavior while under the load.

Three different methods for imposing load will be discussed here. One applies load through an increase in viscosity of the media surrounding the *Vorticella* cell; this increases the viscous drag force which opposes the motion of the cell as it contracts. A second method holds the cell by suction into the tip of a micropipette; the cell then has to bend the pipette in order to contract. The final method applies a centrifugal force in the direction opposing contraction by placing the cell in a spinning chamber. This third method is fundamentally different from the first two in that the force it applies is present at all times, whether the cell is in the process of contracting or not. In contrast, the first two imposed loads, being proportional to velocity and displacement, respectively, only apply when the cell is actively contracting.

Analysis of force measurements by these various methods is best undertaken by considering the sources of energy development and energy dissipation during the course of contraction. The source of energy for cell contraction is presumed to be the chemical potential arising from the change in calcium concentration available to the contractile mechanism, since by conservative estimates this provides more energy than is dissipated during contraction (Amos 1971) (see Introduction). The dominant mode of energy dissipation depends on the specific experiment and method of applying an increased load; i.e., energy is dissipated through viscous drag in the first case, through work against the opposing centrifugal force in the second case, and through the work involved in bending a pipette away from its equilibrium position in the third case. The various modes of energy dissipation can in turn be examined through inspection of the time course of power expenditure during contraction.

Power, as the product of force and velocity, is more comparable across different modes of energy dissipation than are measurements of force and velocity. Recent work by Arpita Upadhyaya and colleagues at MIT work has shown that maximum power developed against varying levels of viscous drag is constant; the cell slows as it pulls more strongly against larger viscous loads (Upadhyaya, Baraban et al. 2007). This chapter will show that pipette-loaded contractions, as dictated by the nature of the load and its limitations on stalk shortening, generate lower maximum power than do viscosity-loaded contractions. In addition, the area under the power versus time curve, energy, reveals that the work performed during contraction has an inverse relationship to the amount the stalk is allowed to shorten. Therefore this chapter will discuss three limitations on *Vorticella* contraction: 1. maximum force, extrapolated from stall force experiments; 2. maximum power, determined from Upadhyaya's viscous drag experiments; and 3. total energy dissipated, determined by comparison across different loading conditions to

be dependent on degree of stalk shortening. These limitations provide important constraints which must be met by mechanistic models of spasmoneme contraction.

2.1.1. Maximum power limitation

The application of load to the *Vorticella* cell body through increased viscosity was recently performed and evaluated by Upadhyaya (Upadhyaya, Baraban et al. 2007). By adding poly(vinyl-pyrollidone) (PVP) in increasing amounts to the spring water surrounding the cells, they were able to increase the viscosity of the medium up to forty-five times that of water (45 centipoise). Viscous drag force on the cell was estimated by Stokes' drag on a sphere: $F = 6\pi r \eta \upsilon$, where r and υ are the radius and velocity of the cell body, respectively, and η is the viscosity of the medium. It was found that as viscous load increased, the cells slowed down but generated more force. The product of force and velocity attained by the cells was found to give a consistent maximum power of approximately one nanowatt.

2.2. Contraction under centrifugal force

The application of centrifugal forces to cells is commonplace, but the ability to observe cells under such conditions requires a specialized microscope. The Centrifuge Polarization Microscope was developed by Shinya Inoué and colleagues (Inoué, Knudson et al. 2001); it uses polarization optics in combination with a spinning stage, so that cells can be observed under the influence of centrifugal forces. Cells are enclosed in a sealed sample chamber which sits in the spinning stage. Each time the sample comes around to the same point in the rotation, with the

same alignment with the microscope optics, a laser pulse illuminates the sample, enabling its image to be captured on a CCD camera; camera, laser, and rotor are all synchronized so that the image resolution is better than one μm. Maximum rotational speed of the microscope is 11700 rotations per minute (rpm), but the laser illumination is limited to pulses at 30 Hz and therefore limits the maximum imaging rate. In practice, the laser is triggered to fire once per revolution up to 25 frames per second (fps), which occurs at 1500 rpm. After that, the laser fires once for every two revolutions until 3000 rpm, then once for every three revolutions until 4500 rpm, and so on. These frame rates mean that the smallest time interval between observations of *Vorticella* under centrifugal force in the CPM is 1 / 25 fps, or 40 milliseconds.

2.2.1. Methods

Live *Vorticella* were allowed to attach to small fragments of glass cover slips overnight. The fragments were then placed into the CPM sample chamber with ~ 10 μL of sterile spring water and sealed into the microscope stage. Spontaneous contractions of the same cell were observed at 40X over a range of speeds up to the maximum rpm or to the point where the cell body broke away from the stalk, whichever came first. Observations were recorded directly to DVD in video format for later analysis. In many recordings, frames were averaged to obtain a more stable image.

Cell density was measured by Valeriya Baru, a colleague in the Matsudaira Lab at MIT, by centrifugation through a Percoll density gradient. By this method *Vorticella* cell density is in the range of 1.035 – 1.052 g/cm^3.

2.2.2. Results

Vorticella cells were able to contract at the maximum rotational speed attainable on the CPM (11700 rpm or 11477g). Force, F, is calculated from the centrifugal acceleration, a, experienced by the cell and the density difference, $\Delta\rho$, between the cell and the medium:

$$F = a \cdot V \cdot \Delta\rho$$

V is the volume of the cell body and the acceleration, a, is given by

$$a = v^2/R$$

The angular velocity, υ, of the cell is determined by the rotational speed, s (in units of rpm), and radius of the stage, R:

$$v = 2\pi R s / 60$$

For a cell of approximate density between 1.035 and 1.052 g/cm^3, this corresponds to between 236 and 351 nanonewtons of force in aqueous medium, in the direction opposing contraction*. Although the cell is clearly affected by this amount of force (organelles within the cell body separate by density, the stalk lengthens, and extension is drastically slowed), the contractile mechanism is still in working order.

Video sequence from the CPM: **Figure 2.1**

In water, the force calculated above is the maximum opposing force obtainable, due to the low density difference between the cell body and the surrounding medium. Different experimental setups were considered to increase $\Delta\rho$. For instance, a 50% sucrose medium would

* It should be noted that all other forces normally affecting *Vorticella* contraction are still at play; for example we can safely add at least the viscous Stokes' drag to this number, although we cannot calculate what the Stokes' drag is exactly without a measurement of contraction velocity. Fluid drag should also be even greater than Stokes' drag due to the fact that the experimental geometry forces the cell to lie along and contract at a close parallel to the coverslip surface, where drag can be much higher than in the bulk fluid.

enable centrifugal forces up to ~1300 nanonewtons. Unfortunately, due to osmotic pressures, the cells remain alive for only a few minutes in 50% sucrose. It may be possible to label the cells with heavier microparticles to increase the overall cell density; however, the number of 250 nm gold nanoparticles necessary to achieve forces on the order of 1000 nanonewtons would occupy an area greater than the cell surface area.

Since exact magnitude of the applied centrifugal force is determined by the density difference between the cell body and the medium, accuracy of the force measurement relies on the accuracy of measuring this density difference. Therefore the force magnitudes calculated here should not be considered definitive.

Although the CPM cannot stall *Vorticella* contraction, and cannot image the process due to the 25 fps frame rate limitation, it is possible to perform a consistency check on the observations in the CPM to make sure that they fit within the power limitation defined by Upadhyaya's work. If we assume the same constant power (~1 nW) as determined from contractions in varying viscosities, then the maximum forces we observed (~ 250 nN) we would have only slowed the cell down to ~ 0.4 cm/s, or 25 milliseconds per contraction. At 25 fps, or 40 milliseconds between frames, we could not have caught more than one frame during any one contraction. We never did observe more than one frame during any one contraction; therefore the CPM measurements are still within the bounds of the constant power constraint.

Speed of extension after contraction of live cells in the CPM was markedly slowed at high centrifugal forces, as compared to extension in the absence of force [Figure 2.2]. This happens despite the fact that the centrifugal forces are applied in the same direction as the cell's extending motion and can be presumed to assist stalk extension. One possible explanation is that the centrifugally applied strain on the stalk translates to strain within the membranes of interior

organelles and tubules. Tubules which store calcium within the stalk and have ATP-dependent calcium pumps within their membranes may be stretched to a point that mechanical strain on the pumping proteins affects their ability to re-establish the low calcium concentrations needed to extend the spasmoneme. This is another reason why a globally applied load such as centrifugal force complicates the investigation of *Vorticella's* contractile capabilities.

Slowing of extension times in the CPM: **Figure 2.2**

2.3. Contraction under pipette loading

Neither increased viscous drag nor opposing centrifugal force has been able to apply a large enough load to stall *Vorticella* in the middle of contraction, but for different reasons. Increased viscous drag should in theory never be able to actually stop contraction; since the viscous drag force depends on velocity, the cell can always slow down enough to keep the drag force below its maximum capabilities[†]. An opposing centrifugal force should be able to stop the contraction, but the small density difference between the cell and its medium make it very difficult to observe application of forces that are large enough to stall contraction. For these reasons it became necessary to apply greater and more direct mechanical loads to the cell body in order to find the force necessary to stop the stalk in mid-contraction, the stall force.

[†] In practice, in a live cell, viscous drag may be able to slow the cell down enough that it would not complete its contraction in the time before ATPase pumps are able to remove calcium from the contractile apparatus. In such a case the cell would stop somewhere before coiling completely, reverse direction, and re-extend. This would not be a true "stall" but rather an artifact of the limited biological time available for the contraction to occur.

The method chosen to measure stall force was to attach a long, relatively stiff, hollow glass rod (a micropipette) to the cell body so that contraction therefore requires bending of the pipette. If the right match is made between the strength of the cell and the stiffness of the pipette, the cell will be able to bend the pipette to the point that bending it any further will require more force than the cell is able to produce, and contraction will stall. The set of experiments described here was able to use pipettes of appropriate stiffness, calibrated with known forces, to stop the cell in mid-contraction and thereby calculate the stall force of *Vorticella* contraction.

2.3.1. Methods

Pipettes were drawn from borosilicate glass pipettes with an outer diameter of 1.0 mm, inner diameter of 0.78 mm, and length 10 cm [Sutter Instrument, Novato, CA], using a Flaming/Brown Micropipette Puller [model P-80, Sutter Instrument, Novato, CA]. After being drawn to a very fine tip, on the order of one μm in diameter, the pipettes were cleanly broken off and fire-polished in a microforge [model MF-900, Narishige International USA, Inc., East Meadow, NY]. The most effective method for breaking and polishing was to apply some low-melting point glass (in the form of small glass beads [106 μm and finer, G-4649, Sigma-Aldrich Co., St. Louis, MO]) to the microforge filament; when heated and placed into contact with the pipette tip, the molten glass runs up into the hollow channel of the pipette. When the heat is then turned off, the molten glass rapidly cools and the pipette breaks cleanly at the junction between the still hollow part of the pipette and the part filled with molten glass. Final end diameters of the pipettes used for experiments ranged from ~ 4 – 10 μm.

Pipettes were calibrated by applying a known force, F, measuring the observed deflection, Δy, and thereby calculating an effective stiffness, k, for the pipette. The known force was a point

load applied near the end of the pipette by means of the weight of a small piece of mylar [Duralar®, Grafix, Inc., Cleveland, OH]. From the measured area, known thickness (1 mil = 0.00254 cm), and known density (1.39 g/cm^3), the force due to each mylar weight was calculated. Pipette deflections under these known forces were measured in the same microforge used for pipette construction. The pipette was held horizontally in air and the end was observed through the microscope optics of the microforge. A mylar weight was slipped onto the end region of the pipette, and deflection of the pipette from its unweighted position was measured according to the lines on an eyepiece micrometer. It was difficult to place the mylar weight at the very tip of the pipette, so the weight was placed at a few different locations set back from the end of the pipette, and the recorded deflections at the point of the weight were used to calculate values of the spring constant, k. Those k values were plotted against distance from the tip, and a linear fit was used to extrapolate to the k value at the tip of the pipette. The process was repeated for two different weights and the average k was used to calculate forces exerted by cells on that pipette. Figure 2.3 shows the calibration methodology and spring constants for pipettes used for experiments.

Pipette calibration data: **Figure 2.3**

This calibration methodology is consistent with micropipette calibrations carried out by other investigators (Kojima, Ishijima et al. 1994; Tani, Allen et al. 2001). Kojima *et al.* were also able to use thermal fluctuations to calibrate their pipettes, which had spring constants between 0.5 and 5.4 pN/nm. The thermal fluctuation method for pipette calibration relies on the equipartition theorem, which states that the energy of a system at thermal equilibrium is split equally among the different forms of energy dissipation in the system. For the tip of a thin pipette vibrating due

to thermal bombardment, kinetic energy in each dimension is independent and is equal to ½ $k_t<x^2>$. The equipartition theorem sets this quantity equal to the corresponding portion of thermal input, ½ k_BT. This yields an equation for the pipette stiffness, k_t:

$$k_t = \frac{k_B T}{< x^2 >}$$

Stiffness can therefore be calculated from the time averaged squared displacement of the pipette tip as it fluctuates.

For the spring constants of the most flexible pipettes used in our experiments, the expected thermal fluctuations would be ~ one nanometer. Such displacements are detectable (for instance, as tracked by a photo diode array) but not by the camera detection used for these experiments. Since our mylar calibrations are consistent and within the same range as Tani, *et al.*, we believe that the mylar calibration methodology is reliable.

Measurements of pipette displacement by live *Vorticella* contraction were carried out in a Nikon Eclipse TE300 inverted microscope at 40X with DIC optics. A 100 watt mercury lamp was necessary for sufficient illumination at the high frame rates (10000 frames per second) used to capture contractions on a Phantom v7 high speed CCD camera [Vision Research, Inc., Wayne, NJ]. The pipette was mounted on a three-dimensional micromanipulator and attached to a hydraulic suctioning device [Cell Tram Air, Eppendorf, Hamburg, Germany]. The pipette was positioned close to a *Vorticella* cell grown on the edge of a glass cover slip, and suction was increased to make strong contact between the cell body and the pipette. Spontaneous contractions were captured at 10000 fps. The cell was then released from suction and an unloaded spontaneous contraction was observed to make sure that the cells had not been irreversibly damaged by the applied suction.

Videos of cell contractions and corresponding pipette displacements were tracked at the junction of the pipette and cell body using MATLAB [The MathWorks, Natick, MA] code written for the purpose. Tracking data for pipette displacement were smoothed by a three-point moving average filter before further analysis. Pipette displacements were then translated into forces using the calibrated pipette stiffness values described above; i.e., $F = k^*\Delta y_{\text{pipette}}$. Finally, power, P, was calculated as force times the displacement velocity: $P = F^*\Delta y_{\text{pipette}} / \Delta t$, where Δt was the time elapsed between tracked points. In total, data were taken from 15 cells tracked through 23 contractions on three different pipettes.

2.3.2. Results

Live *Vorticella* are able to contract through 20 to 40% of their length[‡] at 1 to 2.5 centimeters per second, generating in the range of 60 to 160 nanonewtons of force before being stalled by the stiffness of micropipettes used in this experiment. A representative image sequence taken from a stall force experiment is shown in Figure 2.4. Average data for 15 cells tracked through 23 contractions on three different pipettes are shown in the table below, along with values indicating 95% confidence intervals on the average.

Contraction sequence under pipette loading: **Figure 2.4**

Pipette displacement data: **Figure 2.5**

[‡] Length was measured as the distance from the junction between the suction pipette and the cell body to the attachment point of the stalk to its substrate.

Table 2.1 Measurements obtained from contraction under pipette loading.

	Minimum stalk length	Maximum force [nN]	Maximum velocity [cm/s]	Maximum power [nW]	Total energy [pJ]
Pipette 1: $k = 0.00246$ N/m					
Average	0.627	109	1.521	0.826	2.586
95% CI	± 0.031	± 11	± 0.213	± 0.200	± 0.513
Pipette 2: $k = 0.00266$ N/m					
Average	0.639	114	1.635	0.931	2.583
95% CI	± 0.024	± 13	± 0.371	± 0.373	± 0.647
Pipette 3: $k = 0.00558$ N/m					
Average	0.801	142	0.984	0.697	1.928
95% CI	± 0.011	± 18	± 0.249	± 0.195	± 0.465

Plots of average displacement, velocity, and force versus time for each pipette are shown in Figure 2.8. All data were aligned in time to set the point of maximum velocity of contraction to occur at t = 0 milliseconds.

Average displacements, velocities, and forces versus time: **Figure 2.6**

Maximum force developed by each cell is dependent on the stiffness of the pipette used [Table 2.1 and Figure 2.6]. When k is larger, the cell cannot deflect the pipette as far as it can for smaller values of k. However, at these smaller deflections, the cell is able to generate higher forces. This implies that the maximum stall force for contraction would be measured at zero deflection and is an isometric force. We cannot measure isometric forces in the current experiment due to the nature of the pipette force transducer; it relies on deflection to know force. However, we can extrapolate maximum force versus fractional shortening data to obtain a reasonable guess for the maximum stall force of the cell. This extrapolation is shown in Figure

2.7, and yields a maximum stall force for *Vorticella* contraction in the range of 180 nanonewtons.

Maximum velocities and forces versus length: **Figure 2.7**

Acknowledgement: Pipette calibrations and stall force recordings were performed by Jonathan Tejada, an MIT undergraduate working on the project with the author.

2.4. Energetics of contraction

All experiments which observe *Vorticella* contraction under increased loading conditions are probing the ability of the contractile mechanism to expend the energy made available to it by calcium binding. From this point of view, it becomes clear that the cell is ultimately limited in the energy it can dissipate; i.e., it is limited by the amount of energy available minus the energy lost to inefficiencies inherent in the contractile mechanism, as well as particular constraints of the applied load[§]. Comparison of energy dissipation across different loading conditions, including both Upadhyaya's viscous drag experiments and the pipette deflection experiments, reveals that the amount of energy dissipated by *Vorticella* contraction falls in the range of 2 – 3 picojoules [Figure 2.8]. Differences between dissipated energy, or work performed by the cell, in different loading conditions reveal that contractions which are stalled before completion by the

[§] For instance, a particular constraint of the pipette deflection experiments is that they prevent the stalk from fully shortening.

opposing force of a suction pipette do not generate as much work as cells which can fully contract under viscous loads.

Power development for different loading conditions: **Figure 2.8**

Areas under the power curves in Figure 2.8a are equal to the energy dissipated in contraction against different external loads. This energy must be less than the energy source, which is presumably derived entirely from the chemical potential energy of calcium binding. One can obtain a reasonable guess for the total energy by using the amount (moles) of calcium bound to the dry spasmoneme according to Routledge's microprobe measurements (Routledge, Amos et al. 1975). Volume of a spasmoneme 200 μm in length and 1.5 μm in diameter is approximately 353 x 10^{-12} mL (=V_s). Routledge also used an interference microscope to measure dry mass concentration of the spasmoneme, equal to 210 mg/mL (=C_s). The actual amount of calcium bound to the spasmoneme, at 1.7 grams of calcium bound per dry kilogram of spasmoneme is then V_s*C_s*1.7 g/kg = 12.6 x 10^{-12} g Ca^{2+} = 3.15 x 10^{-15} moles Ca^{2+}. This figure allows calculation of the total amount of energy available to the contractile apparatus, according to the same formulation used by Amos in 1971:

$$E = RT\ln(\frac{a_1}{a_2})\cdot b$$

R = gas constant
T = temperature
b = moles of Ca^{2+} bound
a_1 = high [Ca^{2+}]
a_2 = low [Ca^{2+}]

Total energy available to the spasmoneme is therefore ~ 35.9 picojoules. This available energy can be divided into three portions: 1. energy dissipated by inefficiencies of the contractile

mechanism, 2. energy dissipated in movement of the cell, and 3. energy that is never actually dissipated at all due to the inability of the loading condition to probe a force and velocity space which allows full dissipation. However, one could argue that the consistency of maximum power and energy dissipated across different viscosities in Upadhyaya's experiments indicates that *Vorticella* at least comes close to dissipating all available energy when contracting against viscous drag[**].

Upadhyaya's experiments probed the mechanics of increased viscosity as a loading condition, showing that maximum power dissipated by the spasmoneme under various levels of viscous drag was a consistent feature of spasmoneme performance (Upadhyaya, Baraban et al. 2007). In addition, her data for one cell contracting in different viscosities show that the energy, or area under the curve, of contraction is also constant. I digitized Upadhyaya's data and compared it to the average power versus time curves obtained for each pipette from the stall force experiments described above; the comparison is shown in Figure 2.8a. As pipette stiffness increases, the fractional length by which stalks can contract decreases, and the work they perform in shortening decreases. Figure 2.8b shows this downward trend with increasing final contracted fractional stalk length.

It is worthwhile at this point to consider the differences between energy dissipation by viscous drag and by pipette bending. Increased viscous load cannot stall *Vorticella* contraction because the cell can always reduce its velocity and thereby decrease the viscous drag force acting

[**] Interestingly, the efficiencies seen here, at approximately 2.8 pJ / 36 pJ = 7 %, are similar to those measured by Moriyama in sending the glycerinated *Vorticella* stalk through a Ca^{2+}-induced Carnot work cycle. The cycle which consisted of three processes: 1. the bath surrounding a stalk held at constant length was changed from pCa 8.0 to pCa 5.8, causing the stalk to generate tension (F); 2. the stalk was released and allowed to fully shorten (ΔL); 3. the bath was changed back to pCa 8.0, allowing the stalk to re-extend under zero tension and return to its initial state. Using the same available chemical potential energy as Amos (E, above), and work $W = \int F\Delta L$, the efficiency of the stalk is $\varepsilon = W/E = 7\%$ Moriyama, Y., K. Yasuda, et al. (1996). "Ca(2+)-induced tension development in the stalks of glycerinated *Vorticella* convallaria." Cell Motil Cytoskeleton **34**(4): 271-8..

against it; in this way it can always keep the opposing force below the value that would stall contraction. Contraction up to a stall force on the other hand, samples maximum force capabilities of the cell, since force increases directly with cell displacement in the pipette method. Viscous drag loading may show the maximum power attainable by *Vorticella* contraction, since a cell under viscous drag loading can in theory dissipate more energy than one stalled by a suction pipette. It does so by finding a balance between force and velocity, always contracting as quickly as possible without exceeding the maximum force it can expend. One way to visualize the difference between viscous drag and pipette loading is by considering the division of potential and kinetic energy during contraction. Potential energy at t = 0 comes from the energy of calcium binding minus the energy which will be lost to inefficiencies. At the time when the stall force is reached, kinetic energy is zero and only potential energy is left. At the time of stalling, potential energy of the cell is then equal to the potential energy at the start of the contraction minus the kinetic energy dissipated in the cell's movement up to that point:

$$PE \mid_{t=stall} = PE \mid_{t=0} - \int P \cdot dt \mid_{t=stall}$$

The cell stalled because the remaining potential energy cannot be used to exceed the loading force. Therefore maximum power occurs in the case where force is just below the stall force threshold at all times, enabling dissipation of all potential energy. This is essentially what happens in Upadhyaya's viscous drag experiments: the cell slows down to decrease force, continue its movement, and dissipate all available energy.

In the pipette loading experiments described here, the cell will be left with potential energy at the time of stalling; if one were able to release the cell at that moment, it would presumably be

able to continue to contract. The stalk is unable to expend all available energy because it is not allowed to fully contract. This implies that contraction is dependent on interactions of molecular entities within the spasmoneme which are prevented from achieving full interaction and power development by the extended length constraint imposed on the spasmoneme as a whole.

These observations are useful as constraints on both potential models of power development by *Vorticella*'s contractile mechanism and potential mimicry of the contractile mechanism in engineered actuators.

2.5. Conclusions

The set of experiments described here sought to explore the origins and limits of *Vorticella*'s spring-driven motion through the application of different loads in opposition to contraction. The differences and implications of different loading conditions were discussed, especially as they pertained to the energetics of contraction. While the application of centrifugal force could not stall *Vorticella* contraction, it did (through slowed extension velocities) reveal sensitivity of the contractile mechanism to a globally applied, deformative force. Application of load via a calibrated suction pipette was able to stall *Vorticella* contraction, uncovering a maximum stall force of about 180 nanonewtons. Energy dissipated through the course of contraction against pipette deflection was found to decrease with the decreased degree of shortening of stalks attached to stiffer pipettes.

This variation of energy dissipated during application of different increased loads reveals intrinsic properties that will be useful for designing appropriate models of the contraction mechanism. For instance, we now know that maximal power and total work produced in

contraction, as defined by viscous drag loading (Upadhyaya, Baraban et al. 2007), must be generated by interactions within the spasmoneme that are maximized at full shortening of the stalk. One approach which may be able to fit the shortening-dependent energy development seen in these experiments involves modeling the spasmoneme as a series of sequentially activated springs. The springs would be activated in series, starting from the cell body, by a calcium pulse running down the stalk at the velocity already measured via the movement of beads placed along the stalk (Upadhyaya, Baraban et al. 2007). After all calcium is released, and the activating signal has traversed the full length of the stalk, power development due to the component springs is zero, and power dissipation takes over. The overall shape of the power curve can then be described by the sum of power development by the springs and power dissipation through movement. The shape of power dissipation is particular to the external environment of the cell, specifically any inertial, viscous, or other loads seen by the cell as it contracts. According to the model, the overall shape of the curve could then match those seen in experiments, rising to peak power and then declining back to zero.

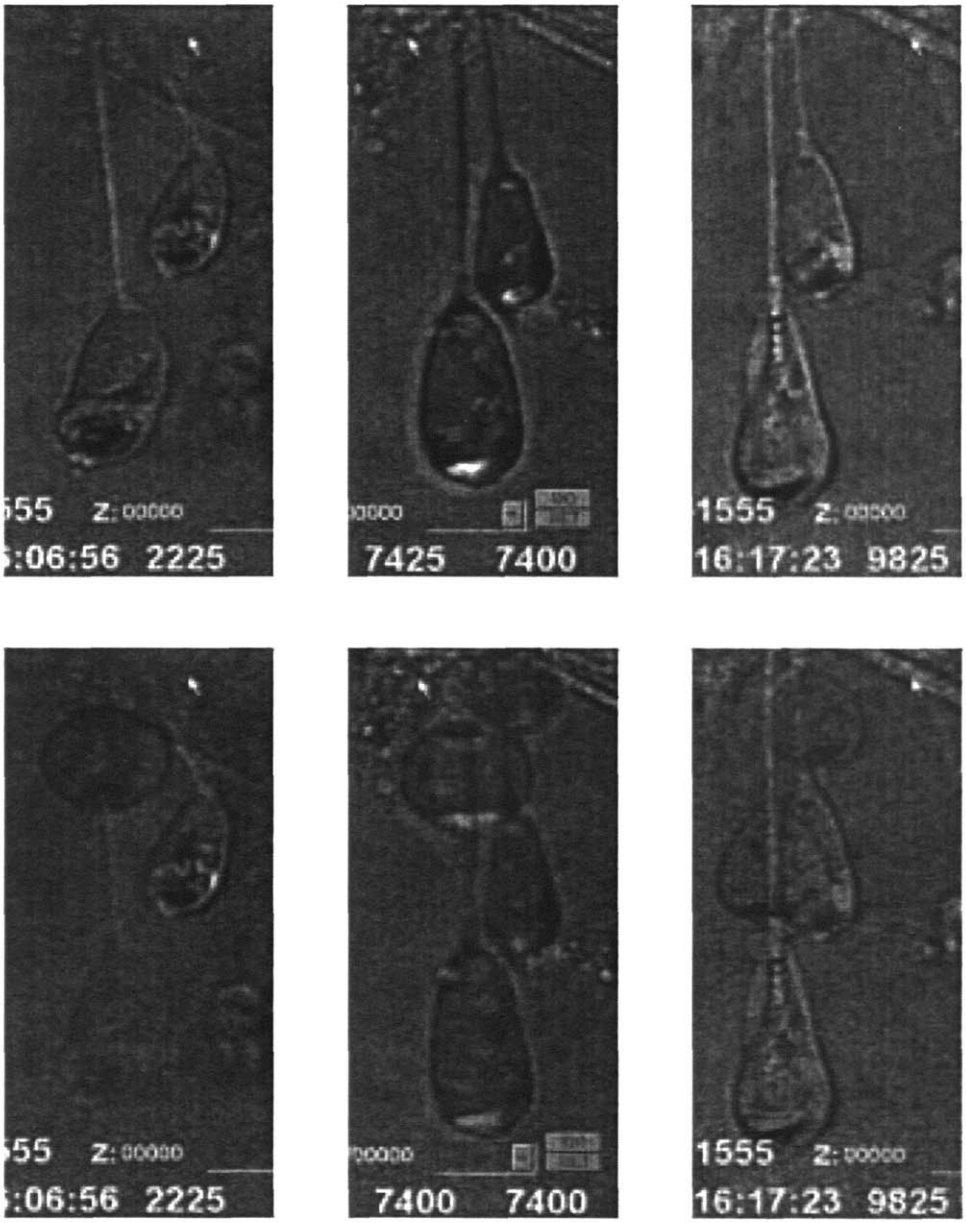
55 Z: 00000
:06:56 2225
7425 7400
1555 Z: 00000
16:17:23 9825
55 Z: 00000
:06:56 2225
7400 7400
1555 Z: 00000
16:17:23 9825

Figure 2.1 Live *Vorticella* in the Centrifuge Polarization Microscope. **(top)** Cells before contraction at various rotational speeds (2225 RPM, 7400 RPM, 9825 RPM) corresponding to centrifugal accelerations of 415g, 4591g, and 8093g, respectively, from left to right. One "g" is an acceleration equal to 9.81 m/s^2. **(bottom)** The same cells in the during the process of contraction and extension. Due to frame averaging, shadows of the cells in both full extension just before contraction, and just after full contraction can be seen in one frame. The polarizer was rotated by 90° in the middle frames with respect to its position in the outer frames, causing the spasmoneme to appear dark instead of light.

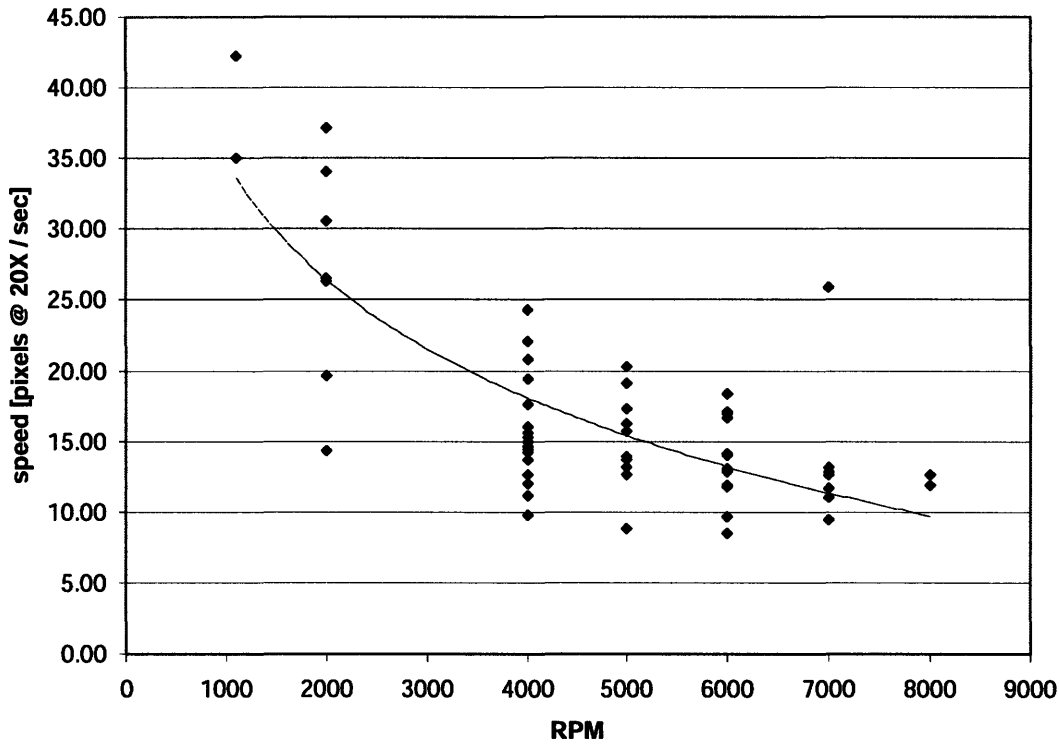

Figure 2.2 Slowing of extension in the Centrifuge Polarization Microscope. Cell bodies were coarsely tracked as they extended after spontaneous contractions. Each data point corresponds to one extension. Speed decreases as centrifugal force increases. The logarithmic trend line is meant only to guide the eye.

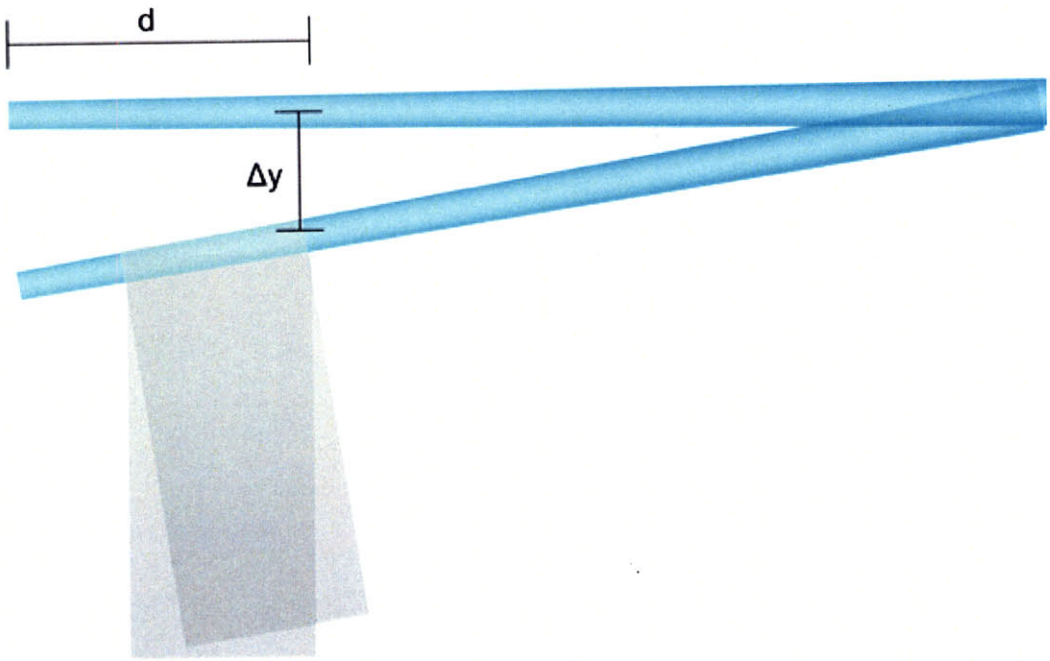
d
Δy

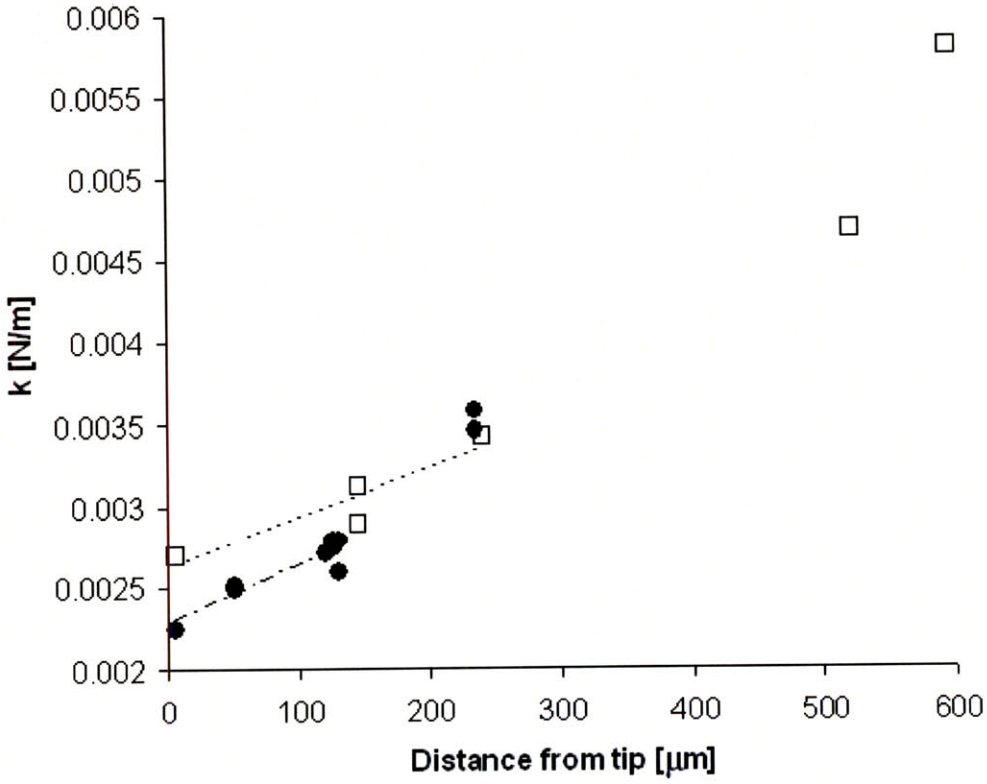
0.006
0.0055
0.005
0.0045
0.004
0.0035
0.003
0.0025
0.002
k [N/m]
0
100
200
300
400
500
600
Distance from tip [μm]

Figure 2.3 Calibration of micropipettes for stall force experiments. **(top)** Schematic showing calibration protocol wherein different weights (slivers of mylar) were applied near the end of the pipette, causing it to deflect from its resting position. Deflections (Δy) were measured at the point of contact between the weight and the pipette, at a distance (d) from the tip, and were used to calculate the spring constant, k = weight / Δy, of the pipette at that distance. **(bottom)** Calculated spring constant, k, vs. distance, d, from the pipette tip, for two different weights: (open squares) F = 1.59 μN and (filled circles) F = 0.948 μN. The relationship is relatively linear for small distances and sharply increases (as would be expected from the dependence of k on pipette diameter and length) for distances greater than about 200 – 300 μm. The y-intercept as determined by a linear least-squares fit was used as the k value of the pipette. By this method, the three different pipettes had spring constants k = {0.0024611, 0.0026587, 0.0055759} N/m.

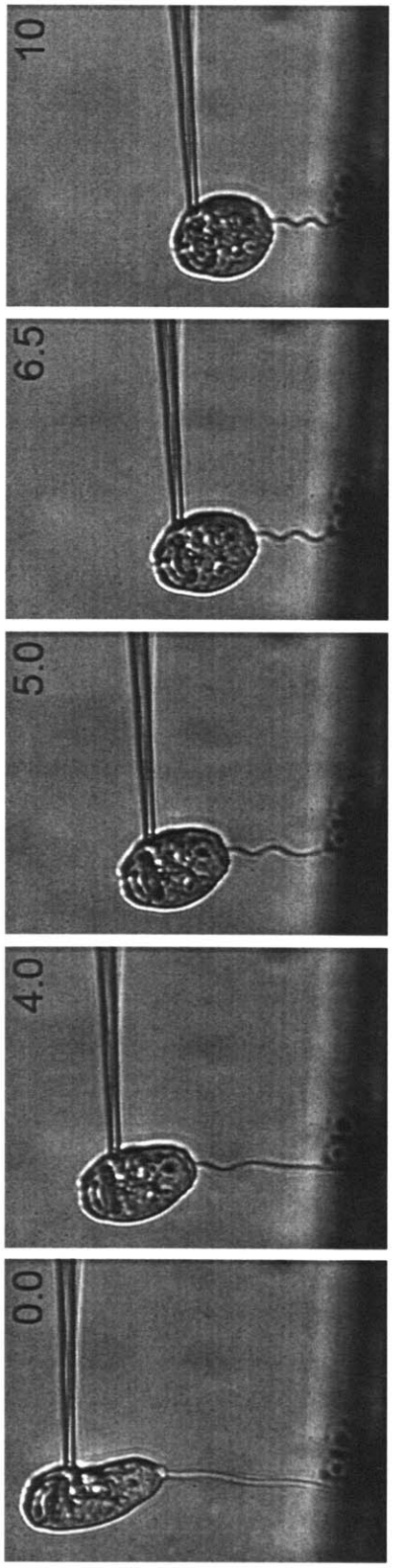
0.0
4.0
5.0
6.5
10

Figure 2.4 Image sequence showing a live *Vorticella* deflecting a micropipette. The cell body is attached to the micropipette through suction into the tip of the micropipette. Time from the start of cell body contraction, in milliseconds, is given at the top of each frame.

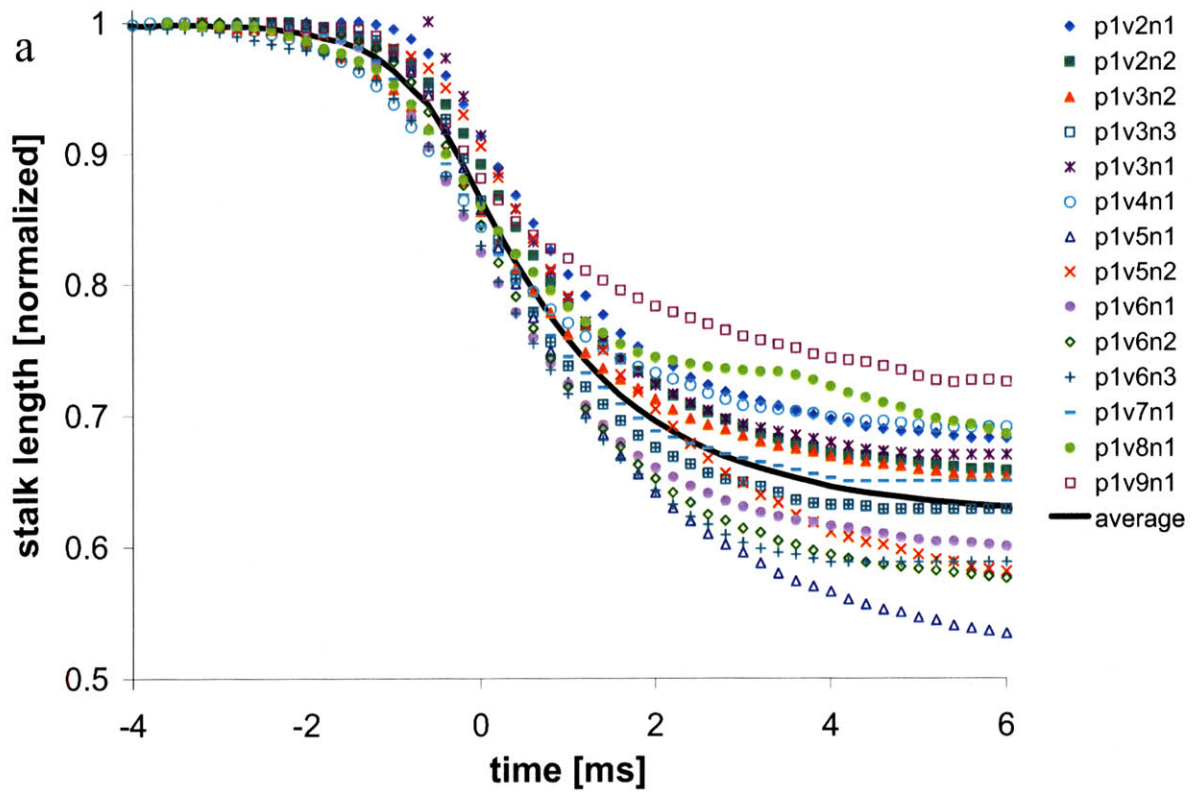

Figure 2.5 Time courses of pipette displacement caused by live *Vorticella* during spontaneous contractions. Each plot shows data for a different pipette. In each plot, the thick black line represents the average of all the displacement data for that pipette. The different symbols correspond to different contractions, some performed by the same cell. The legend entry for each recording indicates the pipette number (p1, p2, or p3), the cell number (v2, v3, etc), and the contraction number for that cell (n1, n2, etc).

(a) Pipette 1: $k = 0.00246$ N/m

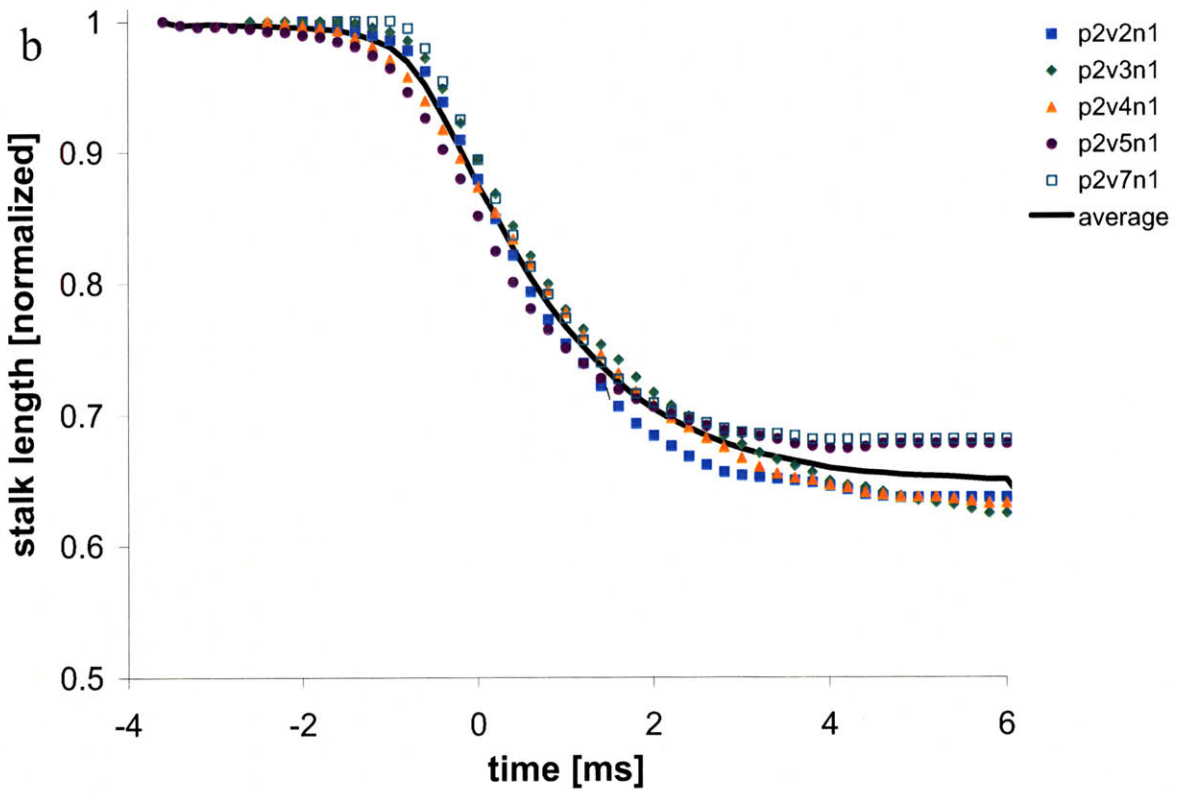

Figure 2.5 Time courses of pipette displacement caused by live *Vorticella* during spontaneous contractions. Each plot shows data for a different pipette. In each plot, the thick black line represents the average of all the displacement data for that pipette. The different symbols correspond to different contractions, some performed by the same cell. The legend entry for each recording indicates the pipette number (p1, p2, or p3), the cell number (v2, v3, etc), and the contraction number for that cell (n1, n2, etc).

(b) Pipette 2: k = 0.00266 N/m

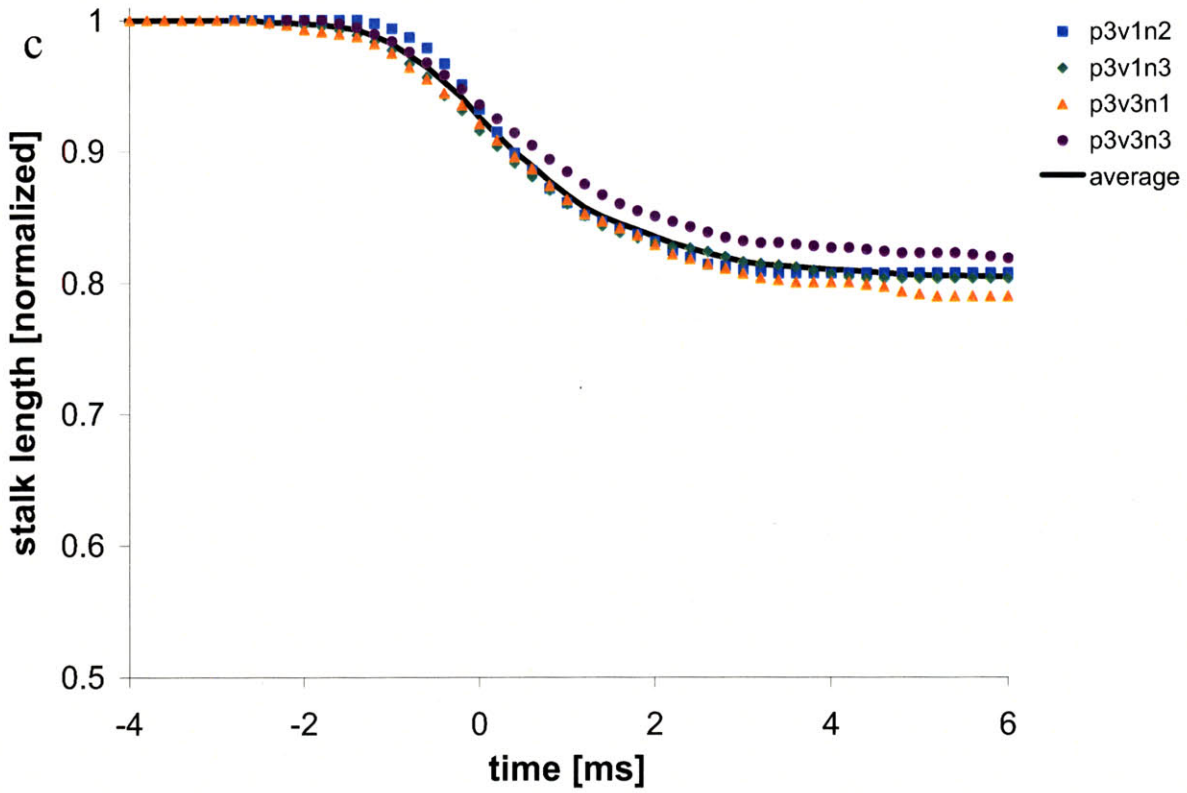

Figure 2.5 Time courses of pipette displacement caused by live *Vorticella* during spontaneous contractions. Each plot shows data for a different pipette. In each plot, the thick black line represents the average of all the displacement data for that pipette. The different symbols correspond to different contractions, some performed by the same cell. The legend entry for each recording indicates the pipette number (p1, p2, or p3), the cell number (v2, v3, etc), and the contraction number for that cell (n1, n2, etc).

(c) Pipette 3: $k = 0.00558$ N/m.

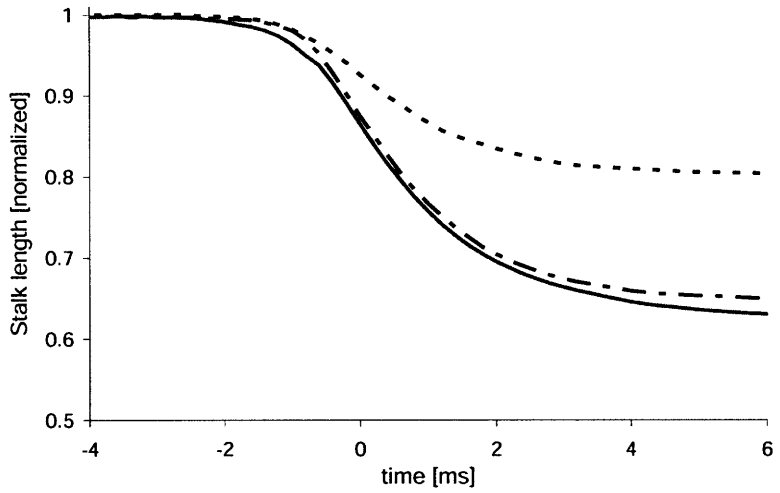
Stalk length [normalized]
1
0.9
0.8
0.7
0.6
0.5
-4
-2
0
2
4
6
time [ms]

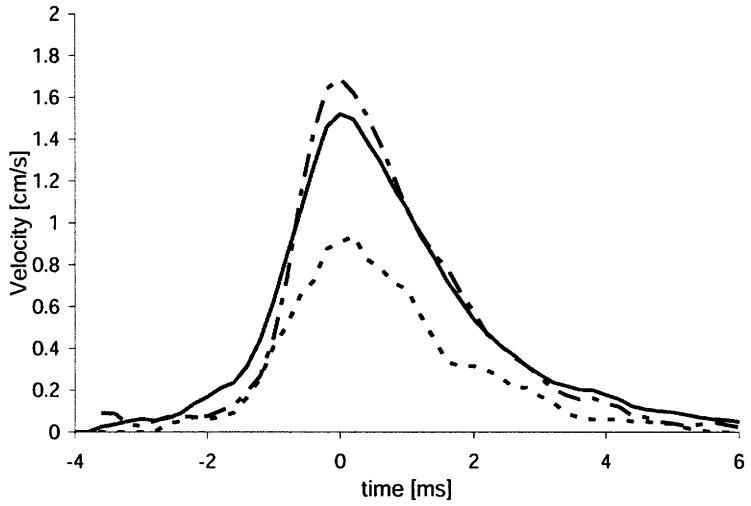
Velocity [cm/s]
2
1.8
1.6
1.4
1.2
1
0.8
0.6
0.4
0.2
0
-4
-2
0
2
4
6
time [ms]

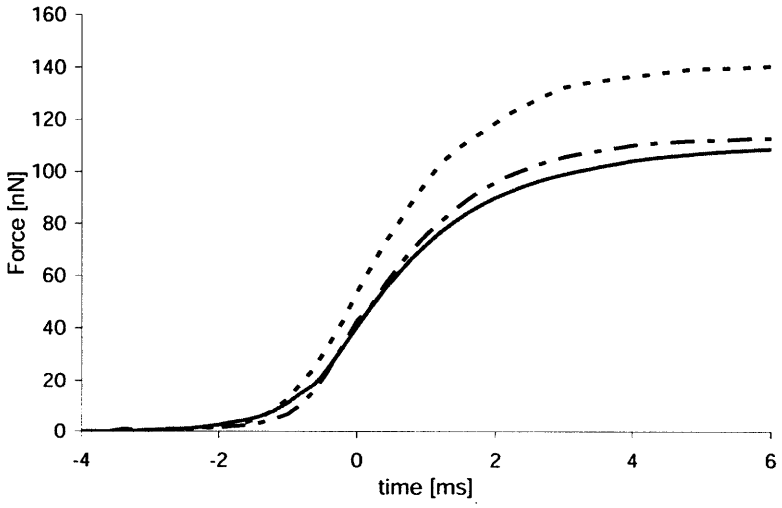
Force [nN]
160
140
120
100
80
60
40
20
0
-4
-2
0
2
4
6
time [ms]

Figure 2.6 Average displacements, velocities, and forces versus time. Each plot shows the average data for each of three different pipettes. The solid lines represent pipette 1 ($k = 0.00246$ N/m), the dash-dot lines represent pipette 2 ($k = 0.00266$ N/m), and the dotted lines represent pipette 3 ($k = 0.00558$ N/m).

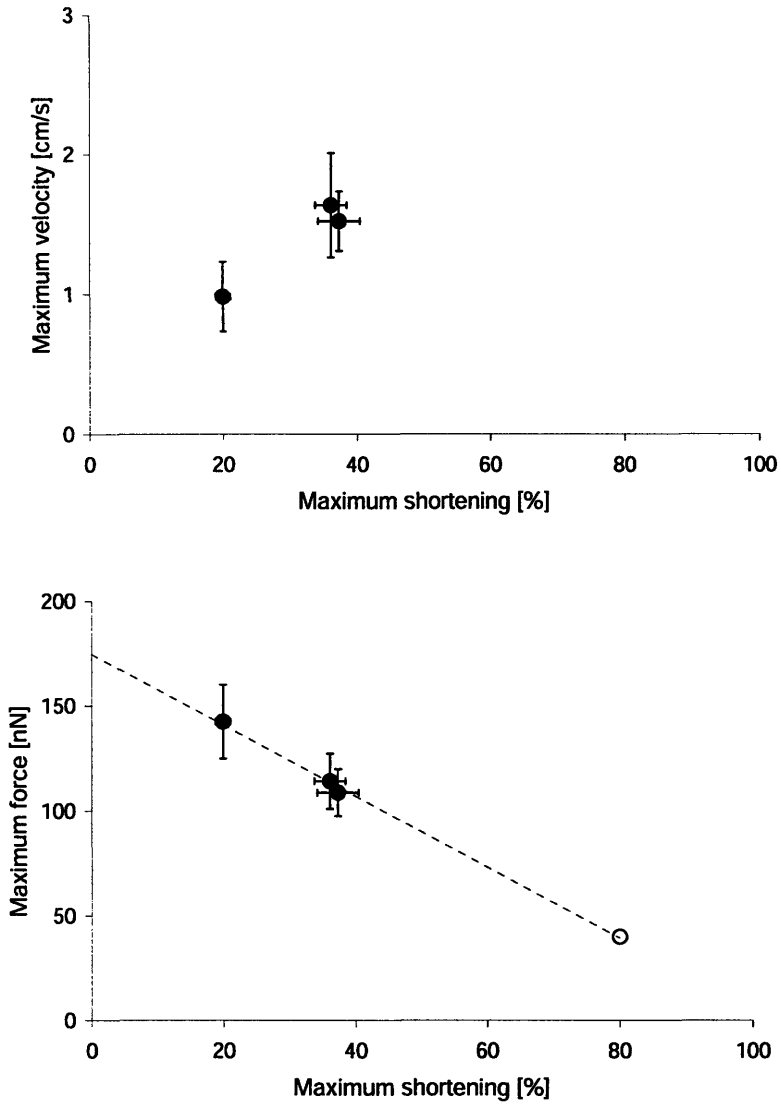

Figure 2.7 Maximum average velocities **(top)** and forces **(bottom)** plotted against the maximum shortening (as a percentage of total resting length) achieved by live *Vorticella* contracting until being stalled by suction pipettes. Solid circles represent average data from three different pipettes while the empty circle represents the movement of freely contracting cells (with force estimated from Stokes' drag). Error bars show 95% confidence intervals. For the force plot, a linear regression fit (dotted line) to the data ($R^2 = 0.9981$) shows a force at zero shortening of 175 nN.

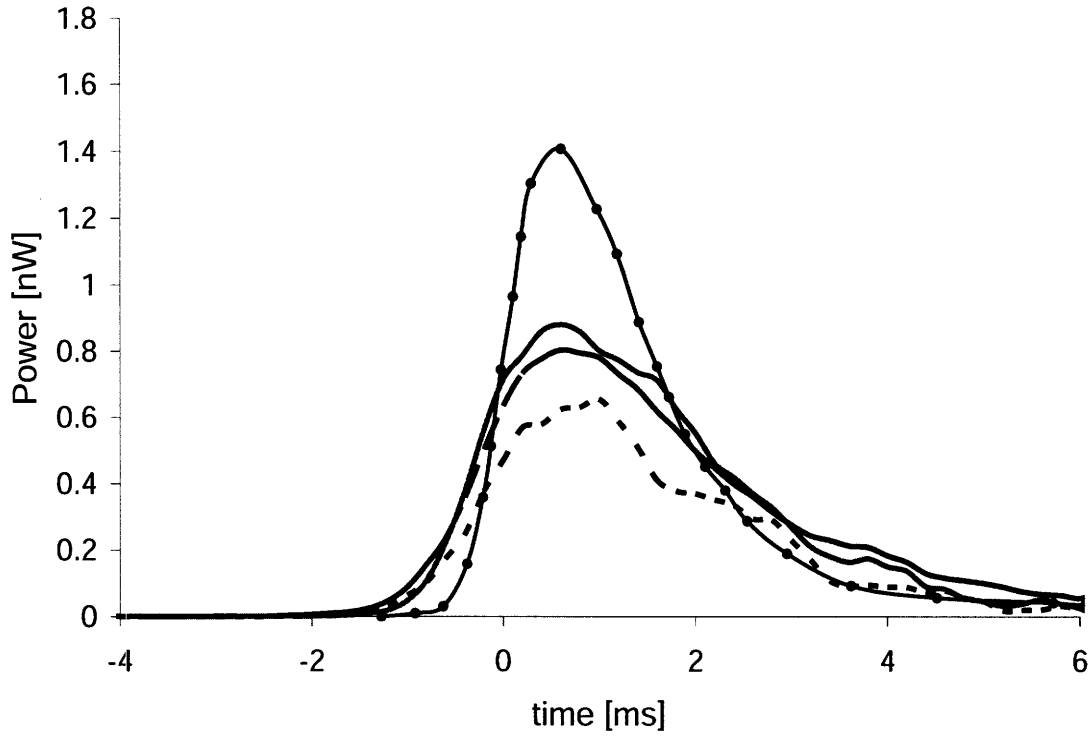
1.8
1.6
1.4
1.2
1
0.8
0.6
0.4
0.2
0
Power [nW]
-4
-2
0
2
4
6
time [ms]

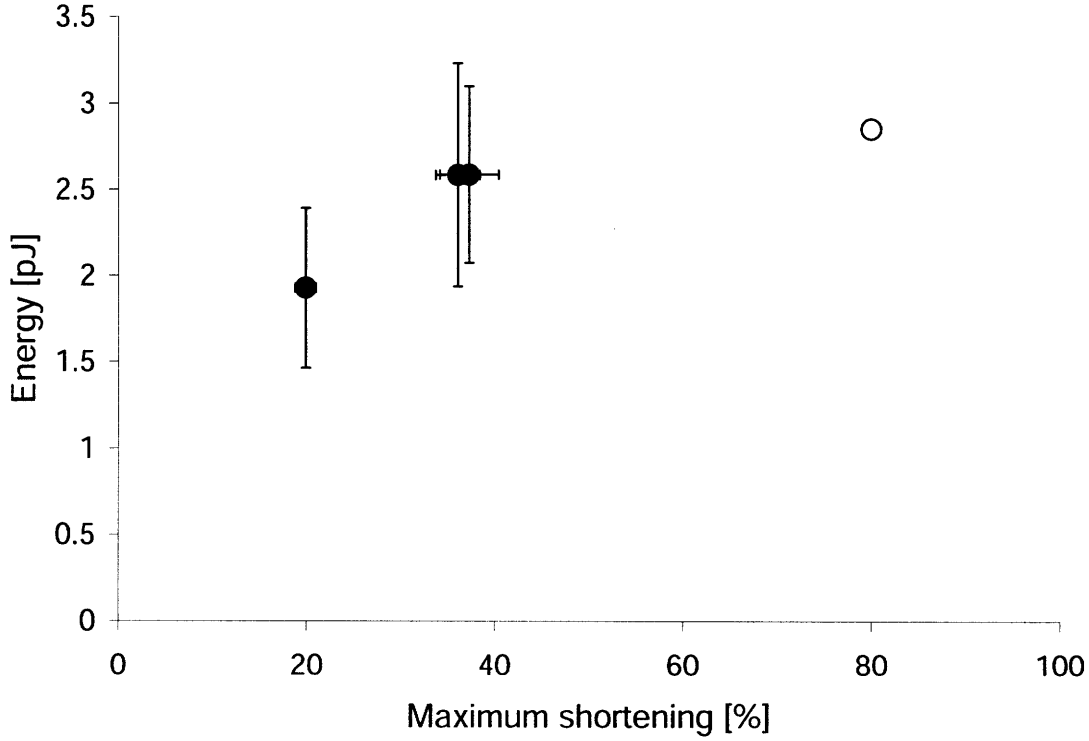
3.5
3
2.5
2
1.5
1
0.5
0
Energy [pJ]
0
20
40
60
80
100
Maximum shortening [%]

Figure 2.8 Power developed and energy dissipated in different loading conditions. **(top)** Power developed over time. The solid black curve with distinct data points shows power dissipation for experiments which applied increased load to *Vorticella* contraction via increased viscous drag. Data were digitized from Figure 3a in Upadhyaya, *et al.,* 2007, showing power versus time for a typical cell at all viscosities tested. The solid gray line represents average power dissipated for all cells stalled by pipette 1 (k = 0.00246 N/m), the dash-dot line represents the same for pipette 2 (k = 0.00266 N/m), and the dotted line represents the same for pipette 3 (k = 0.00558 N/m). Areas under the curves give the average energy dissipated in each loading condition, which is then plotted against the maximum shortening (as a percentage of total resting length) achieved during contraction **(bottom)**. Solid circles represent average data from the three pipettes while the empty circle represents the digitized data for viscous drag loading. Error bars show 95% confidence intervals.

3

Imaging for structural parameters

3.1. Introduction and background

Structural imaging in motile cells provides information on cytoskeletal organization which is critical for constraining mechanistic models for movement. In the case of *Vorticella* spasmoneme contraction, methods like birefringence imaging and electron microscopy, which do not require preexisting knowledge of protein identity, are particularly helpful. Although both methods have been employed in the past, the conclusions drawn and models proposed leave some gaps and inconsistencies.

Early measurements with polarized light and transmission electron microscopy pointed at a fibrous substructure for the spasmoneme; birefringence indicated a high degree of fibrous alignment with the stalk axis in the extended state (Amos 1971) while transmission electron micrographs of the contracted stalk revealed thousands of filaments roughly 2-4 nm in diameter, interspersed with tubules and mitochondria (Amos 1972; Allen 1973). However, in these early studies, no birefringence was seen in the contracted state, leading Amos to surmise that the 2-4 nm filaments could not be the birefringent structures seen in extended cells. Rather, Amos supposed that the birefringence of extended cells must come from another substance which is not visualized by TEM (Amos 1972).

The ambiguities of such a hypothesis, along with the availability of vastly improved instrumentation and methods for polarization microscopy, led me to re-examine the birefringence of the *Vorticella* stalk. This chapter will show high-resolution birefringence images that are not only significantly more informative, but lead to new and different conclusions on the underlying structure. High-speed measurements of live *Vorticella* movements show the persistence of birefringence throughout the contraction-extension cycle. Orientation-independent measurements taken with an LC Pol-Scope show strong birefringence with slow axis parallel to the stalk long axis in both the extended and contracted states. Quantification of textural differences between the two states reveals slight disordering upon contraction. Transmission electron micrographs show a correlation between nanometer-scale filaments and the distribution of birefringence within the spasmoneme. As a whole these measurements indicate that any model of the contractile mechanism should consider the interactions of semi-rigid protein rods at high concentrations which lead to longitudinal alignment in both the extended and contracted states. Such a model and how it derives from the images presented in this chapter is discussed in Chapter 4.

3.1.1. Polarized light microscopy

Polarization microscopy and the measurement of birefringence in biological samples have a long history of providing insight into cellular structures and mechanics. Early movies of dividing cells taken with polarization optics first showed the presence of labile fibers and their components, later proven to be microtubules, segregating chromosomes into their respective daughter cells (Inoué 1953; Inoué 1960). The helical packing of DNA within cave cricket sperm was revealed by a combination of birefringence imaging with UV irradiation (Inoué 1966). Such fundamental discoveries hinged on the fact that polarization microscopy can recognize and

measure biologically significant anisotropies within cellular material, without any need for labels or perturbations.

The basic phenomenon examined through polarized light microscopy is that of birefringence, whereby light traveling through an optically anisotropic material is split into two perpendicular vibrations, one of which travels at a slower speed than the other due to the fact that its electric field vector vibrates in a direction of higher refractive index within the material. Birefringence, or coefficient of birefringence, is then defined as the maximum difference in refractive indices, $N_e - N_o$, which depends on the difference in indices of refraction in any given direction and the direction the polarized ray takes through the material. If polarized light is sent into the specimen, the small phase difference between the two beams as they emerge from the material manifests as an elliptically polarized wave. A second polarizer after the sample, oriented perpendicularly to the first, can then pass one component of that elliptically polarized wave. In practice, another birefringent element with a known slow axis, a compensator, is placed between the crossed polarizers. The effect is to make the background signal grey, while a parallel alignment of compensator and specimen slow axes results in bright white, and a perpendicular alignment results in black. Intrinsic birefringence arises from anisotropies in molecular bonds, whereas form birefringence is a result of a highly anisotropic geometry on a scale less than the wavelength of light used. The birefringence of many biological fibers is primarily form birefringence due to the long aspect ratio of cytoskeletal fibers and the relatively isotropic sub-molecular nature of protein material (Inoué 1986).

3.2. Polarized light imaging of live cell contraction

3.2.1. Methods

The Universal Light Microscope (ULM), developed at the MBL (Inoué 1986), was coupled to a high-speed CCD camera [Phantom v7 by Vision Research, Inc., Wayne, NJ] to take high-speed measurements of birefringence. Bright illumination is necessary due to several limitations, the most important of which is the need to image at settings close to extinction in order to obtain the best possible contrast. Accordingly, a concentrated mercury lamp was used. The microscope was set up for extinction with a 20X/0.4 NA or 40X/0.65 NA rectified objective (Hyde and Inoué 1956; Inoué and Hyde 1957) (augmented with 2.0X magnification before camera) and then a sample was placed on the stage. The compensator was set for extinction of the spasmoneme within the *Vorticella* stalk, and then rotated to low angles (2-10°) on either side to check the reversal of birefringence from bright white to dark black and vice versa. At those low angles, the focus was also shifted slightly to check for anomalous diffraction signals – i.e., to test that a shift in focus did not erroneously appear as a change in birefringence. Low frame rate videos (30 fps) were collected at a compensator angle of 5.5° counterclockwise from the 0° polarizer setting. For high frame rate videos, the compensator was opened up to 15°. This allowed more light to reach the camera within the low exposure times required (100 - 300 μs), at the cost of decreased contrast. However, the amount of light was still limiting and accordingly the cellular contraction was slowed by the addition of 4% PVP (poly(vinyl pyrollidone), P-5288, MW 360000, SIGMA, St. Louis, MO) to the spring water medium. This increased viscosity enabled video capture at a lower rate of 3000 fps with a 328 μs exposure time. All cellular contractions were spontaneous, although the frequency of contraction did increase as the cells were longer exposed to the intense

light. As a protective measure, light to the sample was blocked in between video recording periods to avoid unnecessary perturbations to the cells. Phantom software, included with the camera, was used to capture videos, enhance brightness and contrast, and select frames for later analysis and display.

3.2.2. Results

In order to reveal dynamic birefringence changes during live cell contractions, videos were taken at high frame rates with traditional polarization optics and were therefore orientation-dependent. Accordingly, contractions in three different orientations were visualized at 3000 frames per second (fps). The same three orientations were used to observe extensions at 30 fps.

First, the cell was oriented at +45° to the polarizer and analyzer axes, an orientation chosen for maximum contrast and a strong birefringent signal from the extended spasmoneme. The compensator was set at +5.5° (for extension) or +15° (for contraction), a position chosen to achieve a balance between high contrast (which occurs at low compensator angles) and amount of light let through (which increases with compensator angles up to 45°). In this orientation the spasmoneme birefringence is positively compensated and appears as a bright white signal above the background [Figure 3.1: a,c,f]. The cell was then rotated to -45° to make the same recording with negative compensation (not shown). In this orientation the spasmoneme is black and darker than the background. Finally, the cell was rotated to a 0° position between the first two positions. Here the stalk axis was aligned with the polarizer and was 90° to the analyzer. Stalk birefringence was essentially extinguished by in this orientation [Figure 3.1: b,d,g].

Throughout the cycles of contraction and extension, the underlying birefringence of the stalk never disappears, but rather changes orientation along with direction of coiling. Segments of the

stalk which align at 0° or 90° to the compensator axis appear light or dark, respectively. Those that are 45° off from the compensator axis are extinguished and blend in with the background. By collecting in the three orientations chosen, two cases of orientation change are demonstrated: the first shows a "disappearing" birefringence signal as the stalk coils and loses its 0° or 90° orientation to the compensator [Figure 3.1: a,c]. The second shows a "reappearing" birefringence signal as the stalk coils and thereby gains 0° or 90° alignment with the compensator [Figure 3.1: b,d]. Taken together, the two sets of measurements indicate that birefringence is never actually lost, but rather only loses optimal alignment with the optical components. In such a case its birefringence is not captured by the crossed polarizers and appears to be non-birefringent like the gray background.

Contraction and extension sequences in the ULM: **Figure 3.1**

Observations of contraction timing using the birefringence signal of the spasmoneme yield another clue to the contraction mechanism. Due to the contrast between the spasmoneme and its extracellular sheath, it becomes apparent that the spasmoneme actually shortens at the start of contraction, aligning itself along the inside short path of the coil, forming a straight rod [Figure 3.1: a, center panel]. At this stage, the stalk is slightly compressed and begins curving away from the spasmoneme. As contraction continues, the spasmoneme begins to coil along with the sheath, always maintaining the shortest path through the center of the coiled structure. The combined evidence shows a spasmoneme that shortens and widens upon contraction, forming a coil where bâtonnets within the extracellular sheath localize to points of lowest compression.

3.3. Orientation-independent polarized light imaging of static states

3.3.1. Methods

The classical polarization microscopy method described above yields images wherein the level of birefringence observed depends upon the relative orientations of optical components to the specimen slow axis. With a few substitutions of optical components, the birefringence measurements can be made independently of orientation. An LC Pol-Scope employs two liquid crystal variable retarders in place of a compensator, and a circular instead of linear analyzer. This universal compensator system is capable of generating any polarization state. Five images at different polarization settings are collected in quick succession by changing the electrical signal to the liquid crystal elements. Intensity values in these raw images encode the retardance and direction of slow axis for every image pixel. Retardance is then encoded as intensity, and slow axis direction is encoded according to a color scale, in a composite image based on the original data (Oldenbourg 1995; Shribak 2003). The methodology of image formation is depicted in Figure 3.2.

LC Pol-Scope image formation: **Figure 3.2**

Retardance and birefringence are related by the length and orientation of the path taken through the material by the imaging beam. For the case of fiber birefringence, retardance depends on birefringence as well as the optical path through the sample and its orientation relative to the fiber axis. Specifically,

$$R = (n_e - n_o)*d*\cos\sigma \quad \textbf{(3.1)}$$

where R is retardance, n_e is the refractive index seen by the extraordinary ray, n_o is the refractive index seen by the ordinary ray, d is the path traveled through the material, and σ is the angle between the specimen plane and the birefringent fiber axis. The quantity $(N_e - N_o)$, or coefficient of birefringence mentioned earlier, is equivalent to $(n_e - n_o)*\cos\sigma$. Shribak and Oldenbourg have developed a method of oblique illumination which can measure true retardance for angles $\sigma \neq 0$ (Shribak and Oldenbourg 2004), but such illumination was not used in these studies. Birefringence elements lying at an incline to the x-y imaging plane are therefore measured as a reduced signal depending on their angle of incline. It is anticipated that this effect will be negligible in extended stalks but possibly more relevant to contracted stalk measurements.

When required for experiments, freely swimming *Vorticella* were poured from their culture flasks into Petri dishes containing #1½ or #0 cover slips for attachment. Before observation, cover slips were rinsed with sterile spring water [Poland Spring, Wilkes Barre, PA] and constructed into a microscope slide. Some *Vorticella* which were imaged in a contracted state were found spontaneously contracted in spring water, likely as a result of mechanical disturbances during slide construction. Most contracted cells imaged in the LC Pol-Scope were induced to contract by the addition of dibucaine [Sigma D 0638, St. Louis, MO], a local anesthetic which demonstrates many other cellular effects secondary to its anesthetic capabilities (Frangopol and Mihailescu 2001). The exact mechanism of action is not known, but dibucaine has been shown to affect membrane proteins, possibly preventing the re-uptake of Ca^{2+} by ATPase pumps in the membrane of Ca^{2+} storage sacs (Mondal and Chakrabarti 1992),(Senisterra and Lepock 2000). Therefore, while it is not known how dibucaine induces contraction, it likely

maintains the contracted state through such inhibition of Ca^{2+} uptake. Cells attached to cover slips were washed with rinse buffer (RB; 100 mM NaCl, 4 mM EGTA, 50 mM Tris-Cl, pH 6.8) and then placed into a dish containing 10 mM dibucaine in RB. Contraction happens immediately and the cover slip was quickly constructed into a slide for observation. In 10 mM dibucaine, we did not observe the spontaneous cell extension which can occur at lower (1-2 mM) dibucaine concentrations. However, washing cells with RB after 10 mM dibucaine exposure does result in spasmoneme extension (Valeriya Baru, unpublished observations).

3.3.2. Results

The stalks of live cells exposed to either EGTA (extended), or dibucaine (contracted) and thereby held in that particular static state, display two distinct birefringent structures: the spasmoneme itself and the surrounding sheath [Figure 3.3]. The sheath in profile consists of two continuous and parallel birefringent lines outside the spasmoneme; its retardance is stronger than that of the spasmoneme and varies sinusoidally in magnitude as it progresses along the length of the stalk [Figure 3.5]. In uncontracted, extended stalks, the slow axes of birefringent elements are parallel to the long axis of the stalk. The texture of retardance in the extended spasmoneme varies from stalk to stalk and is reflected in the variation of average retardance and birefringence. Average retardance of an extended spasmoneme is 1.122 nm, and the average thickness is 1.398 μm. These measurements yield an average birefringence of 0.000787 [Table 3.1].

Contracted stalks also exhibit birefringence of the spasmoneme and extracellular sheath, with slow axes aligned with the stalk long axis as it travels through a coil. The spasmoneme retains 95% of the retardance seen in the extended stalk and 90% of the birefringence as becomes about 20% thicker [Table 3.1]. Ninety-five percent confidence intervals on the mean retardance,

thickness, and birefringence in contracted spasmonemes are larger than in the extended case. The average retardance and average birefringence measurements for extended and contracted spasmonemes cannot be determined (by two-tailed t-test) to be coming from statistically distinct populations ($p = 0.7062$ for average retardance, $p = 0.2565$ for average birefringence, 95% confidence).

Table 3.1 Spasmoneme measurements (averages ± 95% confidence intervals)

	Average Retardance [nm]	Directional Retardance Ratio	Average Thickness [μm]	Average Birefringence [x10^3]
Extended *n = 16*	1.122 ± 0.144	0.929 ± 0.022	1.398 ± 0.151	0.787 ± 0.146
Contracted *n = 11*	1.065 ± 0.256	0.768 ± 0.074	1.673 ± 0.435	0.704 ± 0.190

Extended and contracted stalks in the LC Pol-Scope: **Figure 3.3**

Birefringence images at this resolution in space and time provide information on the roles of the spasmoneme and the extracellular sheath during contraction. Sheath birefringence is easily distinguished from spasmoneme birefringence in both static and dynamic images. Bâtonnets are a major contribution to sheath birefringence, as can be seen from periodicity of the sheath retardance in an extended stalk. At points along the sheath where the spasmoneme is farthest away, sheath retardance is highest [Figure 3.5]. Likewise, where the spasmoneme is closest to the sheath, retardance is lowest. These signal variations correspond well with the known bâtonnet configuration of an opposite-handed coil situated on the far side of the stalk from the spasmoneme.

In order to visualize the three-dimensional contracted stalk structure, a maximum intensity projection was made using optical slices collected throughout the stalk volume in the z-dimension. This projection makes it easier to see that the retardance slow axis in the spasmoneme follows the direction of coiling of the stalk, but it also shows that the spasmoneme takes the inside, shorter path through the coil [Figure 3.4]. Also, the effect of filament pitch into or out of the focal plane [$\sigma \neq 0$], which manifests as a lower retardance according to the cosine law [$R = (n_e - n_o)*d*\cos\sigma$], can be seen in the intensity decreases at the curves of the coil.

3.4. Ordering parameters

3.4.1. Methods

Quantitative analysis of differences in retardance between states dictates that as much information as possible is encoded into intensity values alone rather than intensity and hue, enabling simultaneous measurement of changes in retardance and slow axis direction through the manipulation of those intensity values. To that end, projected retardance images were calculated:

$$R_{proj} = R*\cos(2\varphi - \alpha), \qquad \textbf{(3.2)}$$

where φ represents the slow axis angle, $0^\circ < \varphi < 90^\circ$, and α is the angle between the spasmoneme long axis and the horizontal dimension of its calculated image. In most cases the stalk axis was usually aligned with horizontal in the original images so that α was equal to zero. None of the images was digitally rotated before data analysis. Equation 3.2 renders retardances which are the same magnitude but have slow axes at 90° to each other as projected retardances with opposite

signs. Magnitudes of the retardance and projected retardance signals were measured as an average value across focused regions of the spasmoneme in any given image after using manual tracing to define the spasmoneme edges. Path length through the specimen was estimated from width of the spasmoneme in any given image. Assuming that the spasmoneme is elliptical*, average thickness across a line perpendicular to the fiber axis is given by the cross-sectional area of the ellipse divided by the width in that section. Dimensions of the elliptical cross-section were defined by the minimum and maximum widths measured along the spasmoneme. Therefore for the ith line across the width of the spasmoneme,

$$d_i = \pi * W_{max} * W_{min} / W_i \qquad \textbf{(3.3)}$$

where d = average path length = average spasmoneme thickness, W_i = spasmoneme width, W_{max} = maximum spasmoneme width and W_{min} = minimum spasmoneme width.

Average birefringence was then calculated, according to equation 3.1, using the calculated path length from equation 3.3.

After averaging over the spasmoneme material, the projected retardance signal was divided by the retardance, yielding the "directional retardance ratio":

$$DRR = \langle R_{proj} \rangle / \langle R \rangle \qquad \textbf{(3.4)}$$

* The spasmoneme is elliptical in the extended state but becomes circular in cross-section after contraction. Equation 3.3 is still valid for a circular cross-section.

This quantity indicates the degree to which the retardance signal aligns with the stalk long axis. A value close to 1 indicates a high degree of directionality along the spasmoneme long axis, while values close to -1 indicate a high degree of directionality at 90° to the long axis. Values around zero can indicate a high degree of directionality at 45° to the long axis, or, more likely, a higher degree of azimuth disorder.

In order to generate the histograms in Figure 3.6, slow axis angle values (φ) for all of the same pixels used in calculating $\langle R \rangle$ and $\langle R_{proj} \rangle$ were converted into values of $\cos(2\varphi - \alpha)$. These values were then counted and formed into two separate histograms, one for the set of all spasmoneme pixels in extended cells, and one for the set of all spasmoneme pixels in contracted cells.

ImageJ software (Rasband 1997-2006) was used to crop image sections for further analysis in MATLAB [The MathWorks, Natick, MA]. ImageJ was also used to create maximum intensity projections of optical z-slices into the x-y plane. Slices were thresholded at 60/255 gray levels to diminish background and enable a clearer projected image. Statistical analyses were performed on the tabulated data (average retardance, average birefringence, DRR, etc.) in Excel [Microsoft Corporation, Redmond, WA].

3.4.2. Results

Slow axis angle distributions among the pixels of both extended and contracted spasmonemes are heavily weighted towards alignment with the stalk long axis (which occurs at $\cos(2\varphi-\alpha) = 1$), as shown in the histograms in Figure 3. The rate at which the histograms fall away from alignment indicates the distribution of angles within each set of spasmonemes; the contracted

spasmonemes have a larger spread of angle values than the extended spasmonemes, whose angle distribution falls more steeply away from long axis alignment.

Slow axis angle histograms: **Figure 3.6**

The directional retardance ratio (DRR) quantifies the degree to which microscopically resolvable birefringent elements in the spasmoneme are aligned with the long axis of the stalk. It greatly reduces the variation seen in the retardance signal alone, and shows a clear demarcation between extended and contracted states. The DRR for extended cells is 0.929 out of a maximum of one. For contracted spasmonemes, the DRR reduces to 0.768, or 83% of the DRR for extended cells [Table 1]. Distinction between the two states by DRR is statistically significant, as determined by a two-tailed t-test with a resulting p-value of 0.0014 at 95% confidence.

3.5. Transmission electron microscopy

3.5.1. Methods

Cells were grown on large plastic Petri dishes to high density and washed well with sterile spring water. Cells meant to be kept in the extended state were then rinsed with RB, and immediately fixed for one hour in Karovsky's fix [2.5% glutaraldehyde, 3% paraformaldehyde with 5% sucrose in 0.1M sodium cacodylate buffer (pH 7.4)] plus 10 mM EGTA. Cells meant to be fixed in the contracted state were induced to contract by the addition of 10 mM dibucaine to the spring water. They were then rinsed in RB without EGTA and with added calcium (100 mM NaCl, 1 mM $CaCl_2$, 50 mM Tris-Cl, 2 mM dibucaine, pH 6.8) to help maintain the contracted

state. Fixation was in Karovsky's fix + 1 mM $CaCl_2$ for one hour. After fixation, the plates were checked for high fractions (> ~70%) of extended or contracted cells. Cells were then scraped from the plates and collected through two successive centrifugations, first at 3500g to reduce volume, and then at 14000g to form a solid pellet. Tissue was then post fixed in 1% OsO_4 in veronal-acetate buffer. The tissue was stained in block overnight with 0.5% uranyl acetate in veronal-acetate buffer (pH6.0), then dehydrated (into ethanol) and embedded in Spurrs resin. Sections were cut on a Reichert Ultracut E microtome with a Diatome diamond knife at a thickness setting of 50nm, and stained with 2.0% uranyl acetate followed by 0.1% lead citrate. Samples were examined using a Jeol 1200EXM at 60 KV or a Phillips EM410 at 80 KV. Printed photographs were scanned and contrast levels adjusted slightly in Photoshop [Adobe Systems Inc., San Jose, CA].

3.5.2. Results

TEM images of extended and contracted cells show structural elements which are consistent with those seen with polarized light. A longitudinal slice through the extended stalk [Figure 3.7] shows the fibrous spasmoneme within a largely transparent sheath. Three bâtonnet groupings are seen in the upper right side of the sheath. The spasmoneme overall appears to be made up of twisted longitudinal fibers. Higher magnification images of the spasmoneme [Figure 3.7] show round membranated structures (perhaps mitochondria and/or tubules) enmeshed in a dense network of small filaments roughly 3-6 nm in diameter. An important feature to notice in the extended stalk is the effective grouping of the small filaments into larger fibers by the tubules. Figure 3.8 shows a slice through one coil of a contracted stalk. The sheath is thrown into folds at the points of high curvature in the coils, and is smoother at the outer edges. Bâtonnets can be

seen in cross-section at these outer edges. At greater magnification [Figure 3.8] the twisting of the filamentous material and tubules is more apparent. These images agree well with those seen before for contracted cells (Amos 1972; Allen 1973).

TEM images of extended stalks: **Figure 3.7**

TEM images of contracted stalks: **Figure 3.8**

3.6. Conclusion

This set of high resolution, orientation-independent polarization images demonstrates that the spasmoneme and sheath maintain their birefringence with slow axis oriented along the stalk long axis, coiled or otherwise. Textural qualities in the birefringence signal are quantifiably distinguishable between the extended and contracted states, and correlate to fiber groupings seen in TEM images. The spasmoneme and sheath are distinct structural elements that play different roles in contraction. The spasmoneme appears to actively shorten while the sheath provides structural constraints. Accordingly, we focus on shape changes of the spasmoneme, and the textural and orientation changes within spasmoneme birefringence for clues into the molecular level interactions which drive *Vorticella* contraction.

Assuming that any individual birefringent element within the spasmoneme does not change birefringence but rather only changes its orientation within the spasmoneme, the change in average retardance due to contraction is due to at least three effects – a change in path length as the spasmoneme changes geometry, and changes in orientation of birefringent elements both within the imaging plane and out of it in the z direction. We have accounted for path length

(thickness) changes in the calculation of birefringence. Changes in orientation within the imaging plane are captured in the directional retardance ratio. It is possible to image the true birefringence of elements which tilt out of the imaging plane (Shribak and Oldenbourg 2004); however we have not taken such a measurement and such tilts will act to reduce the birefringence seen.

Changes in birefringence orientation within the imaging plane therefore provide the most helpful information in the current study. The histograms in Figure 3.6 show that birefringent elements within extended cells tend to be more highly aligned with the stalk long axis than are birefringent elements within contracted cells. The directional retardance ratio (DRR) proves to be a reliable and consistent method to quantify such changes by accounting for both slow-axis orientation and retardance magnitude, combining them into a metric which reveals the fraction of retardance signal which is oriented along the long axis of the stalk. When distinguished by the DRR, extended and contracted cells clearly differ in degree of retardance orientation; ordering of ~93% in the extended state drops to ~77% in the contracted state. Presumably, these are two states along a spectrum ranging from highly ordered (DRR = 1, 100% ordering) to disordered (DRR = 0, 0% ordering) molecular material. The live cell operates within the high end of the spectrum, perhaps due to constraints on shape, protein concentrations, reversibility, or any other number of undetermined parameters.

Another feature of the DRR measurement is that it greatly reduces the variation seen in the retardance signal in both the extended and contracted states. This may be because the underlying cause of retardance variation is textural variation due to the mixture of contractile proteins and tubules which make up the spasmoneme material. Some optical sections through the spasmoneme appear to have three or four distinct fibers running along the length [Figure 3.3];

these birefringent "fibers" correspond well to the distribution of 2-4 nm filaments in TEM images of the extended cell [Figure 3.7]. These filament groupings would appear as birefringent fibers only in opposition to the negative space (i.e., not birefringent) created in the image by the tubules running longitudinally along the stalk. Other optical slices of extended stalks [not shown] show a more continuous birefringent signal, presumably due to the coincidence of viewing an area with fewer tubules.

The persistence of birefringence throughout contraction and extension limits the number of models which can feasibly explain the mechanism of *Vorticella* motility. Neither the model of rubber-like elasticity nor the model of coiling subfibers proposed by Salisbury (Salisbury 2004) is consistent with the persistence of birefringence. Both of these models rely on a loss of birefringence in the contracted state. However, we can consider a new model, with filamentous subunits corresponding to semi-rigid rods which interact at high protein concentrations. At the high concentrations likely found in the *Vorticella* stalk[†], entropic forces will actually mandate an ordered array of proteins in the extended state. The difference between the extended and contracted states lies in the interactions between these rods, which are drastically affected by the addition of calcium.

Further details of a proposed model which is consistent with the structural images presented in this chapter are presented in Chapter 4.

[†] Routledge used an interference microscope to obtain of figure of 210 mg/mL for the dry mass concentration of the spasmoneme (Routledge *et al.*, 1975).

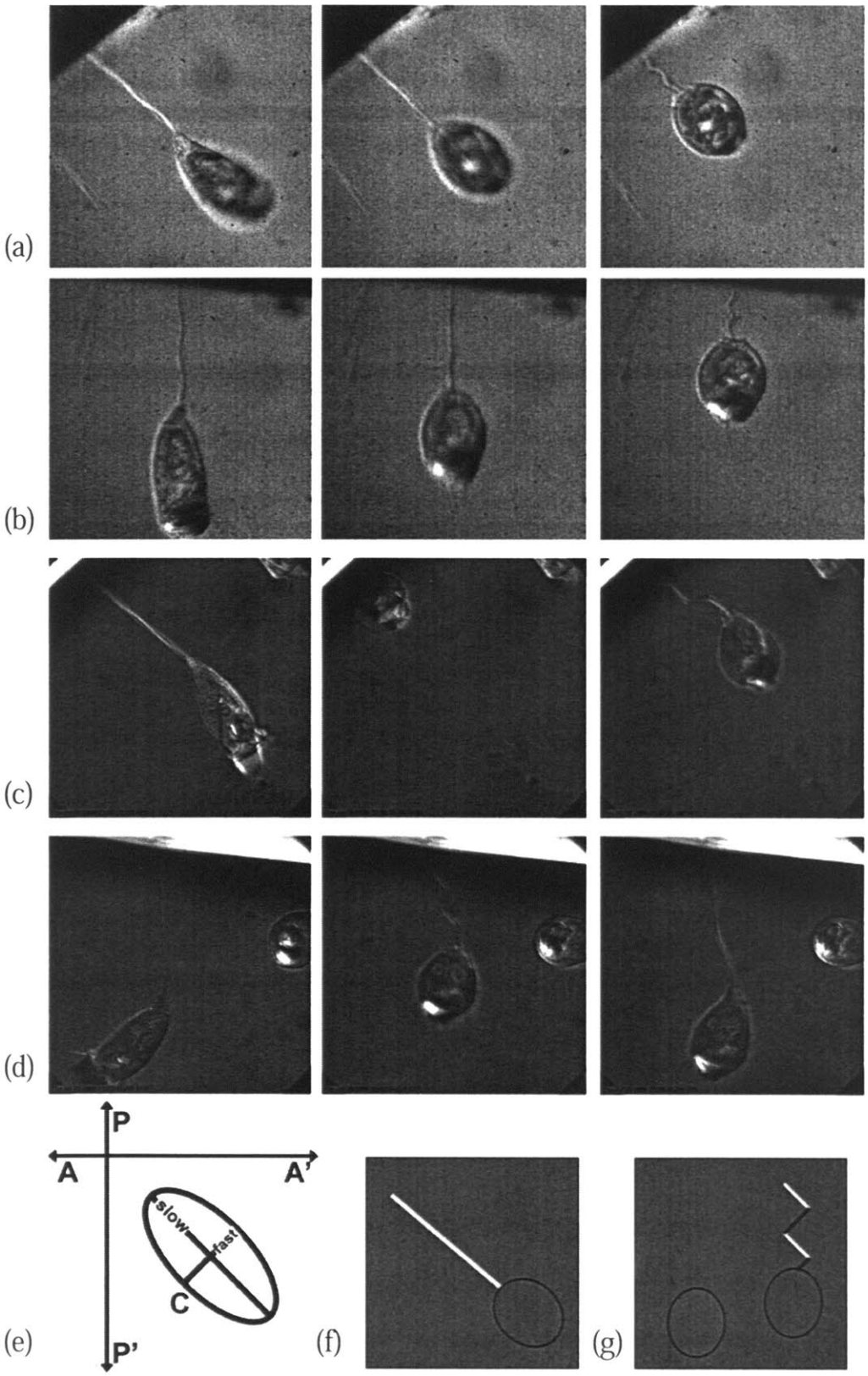
(a)
(b)
(c)
(d)
P
A
A'
slow
fast
C
P'
(e)
(f)
(g)

Figure 3.1 Individual frames captured from real-time recordings of *Vorticella* contraction and extension using the ULM coupled to the Phantom v7 high-speed CCD camera.

(a,b) Still images of cell contraction in 4% PVP, taken at 20X / 0.4 NA and 3000 fps. Compensator was set at 15° counterclockwise from the polarizer while the stage was rotated to the three different orientations.

(c,d) Still images of cell extension following contraction in spring water, taken at 40X / 0.65 NA and 30 fps. Compensator was set at 5.5° counterclockwise from the polarizer while the stage was rotated to the three different orientations.

(e) Schematics showing orientations of optical elements and **(f,g)** expected signals from spasmonemes in various orientations.

Frames from both extension and contraction capture the phenomenon of apparent "disappearing" birefringence (sequences a,c,f) as the coiled spasmoneme goes out of alignment with the compensator. The converse is also witnessed (sequences b,d,g) where birefringence "reappears" as coiled parts of the spasmoneme align with the compensator.

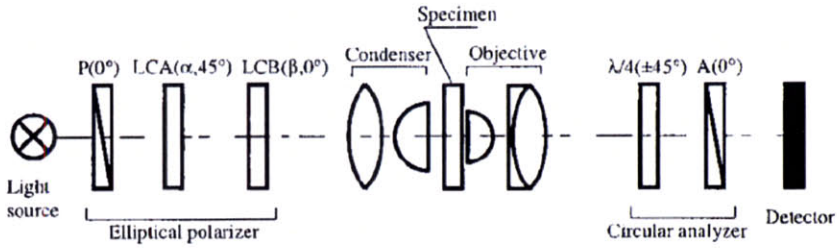
Specimen
P(0°)
LCA(α,45°)
LCB(β,0°)
Condenser
Objective
λ/4(±45°)
A(0°)
Light source
Elliptical polarizer
Circular analyzer
Detector

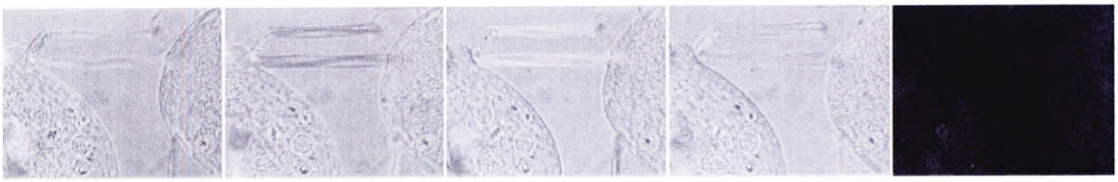

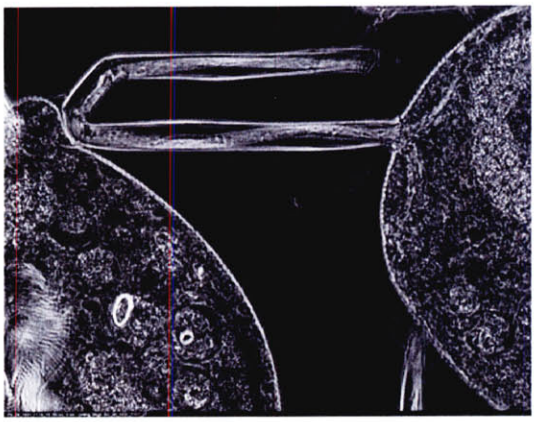

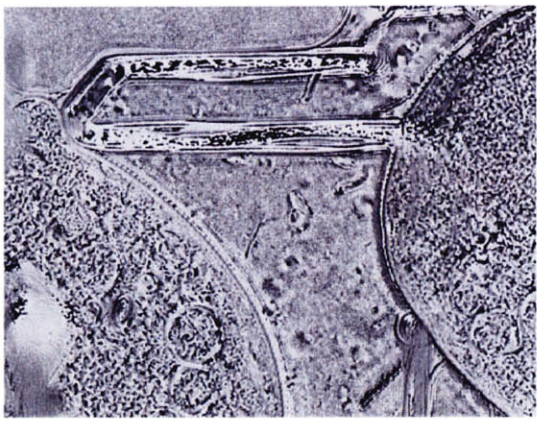

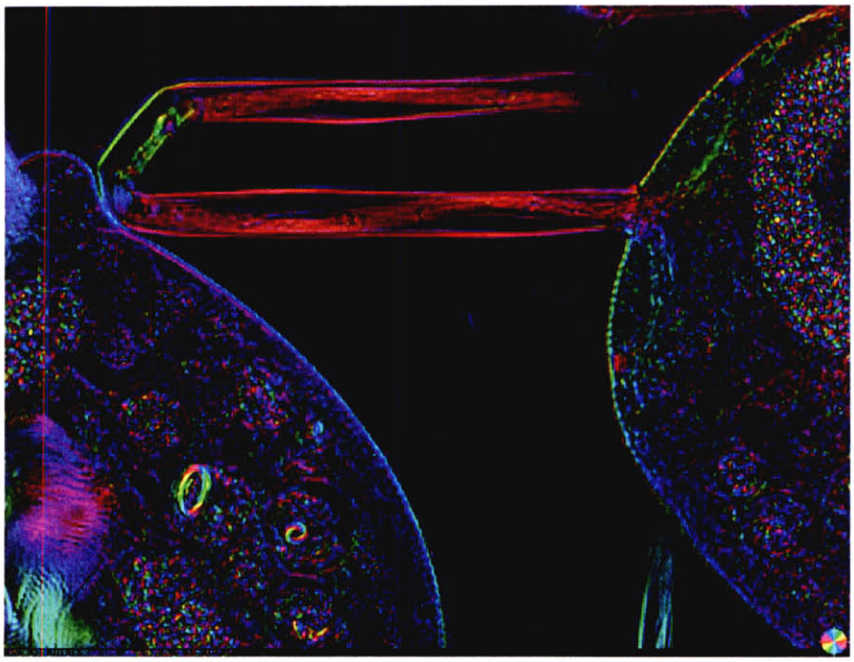

Figure 3.2 Process of image formation in the LC-Pol Scope. **(top)** Schematic of the imaging path within the LC Pol-Scope. Bandpass-filtered 546 nm light passes through an elliptical polarizer made up of a linear polarizer (P) and two liquid crystal variable retarders (LCA and LCB). Polarized light is condensed and passes through the sample to be collected by the objective and sent through a circular analyzer made up of quarter-wave plate ($\lambda/4$) and a linear analyzer (A). The retardances of LCA and LCB are α and β, respectively. **(2nd row)** Through voltage modulation of the liquid crystal retarders, images are procured at four different elliptical polarizations and one circular polarization (far right image). **(3rd row)** The five images in the 2nd row are combined to generate two images in which each pixel encodes either the maximum retardance (left image) or the slow axis angle corresponding to maximum retardance (right image) as an intensity value ranging from 0 to 256. **(bottom)** The slow axis angle is encoded according to the color wheel on the lower left and overlaid on the retardance intensity image to produce a color image showing both maximum retardance and the corresponding slow axis angle for every pixel in the image.

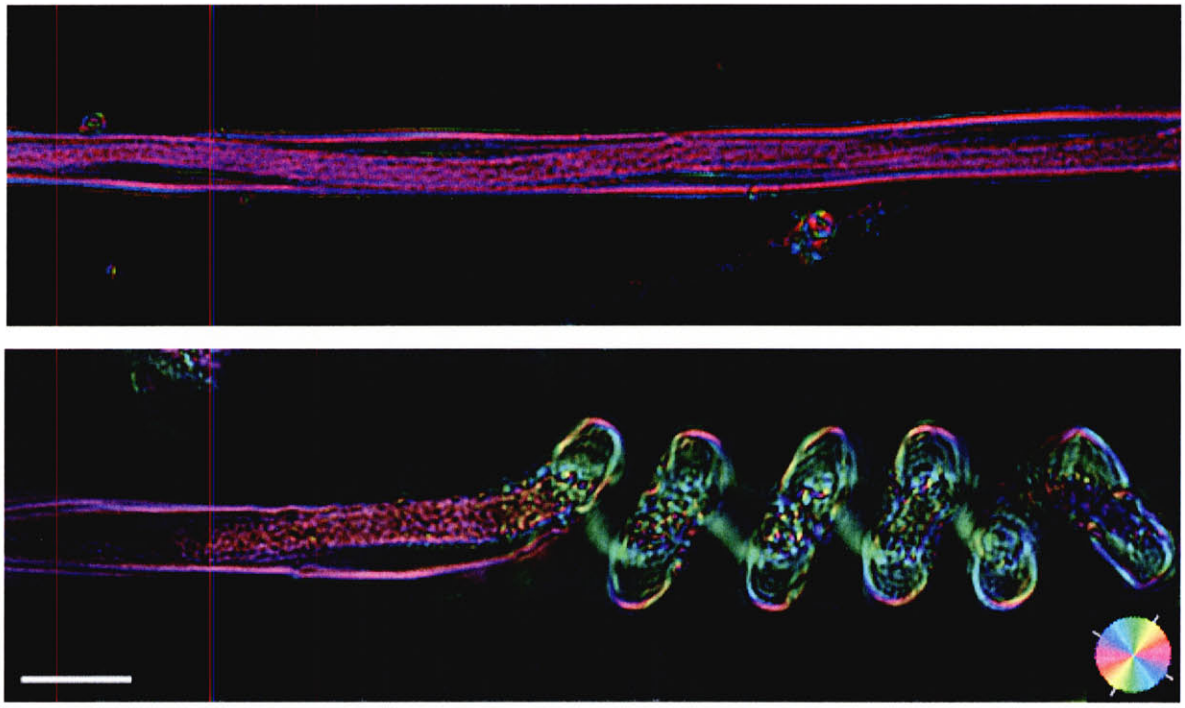

Figure 3.3 LC Pol-Scope images of extended cells in 1 M EGTA **(top)** and contracted cells in 10 mM dibucaine **(bottom)**. Retardance is encoded as intensity (8-bit, with 256 corresponding to the 5 nm (top) or 4 nm (bottom) retardance ceiling) and angle (0-180°) of retardance slow axis is encoded according to the color wheel shown. Retardance arises from proteins in the extracellular sheath as well as from the spasmoneme itself. Textural differences can be seen between the extended and contracted spasmonemes, with a more fibrous substructure being apparent in the extended case. Scale bars = 5 μm.

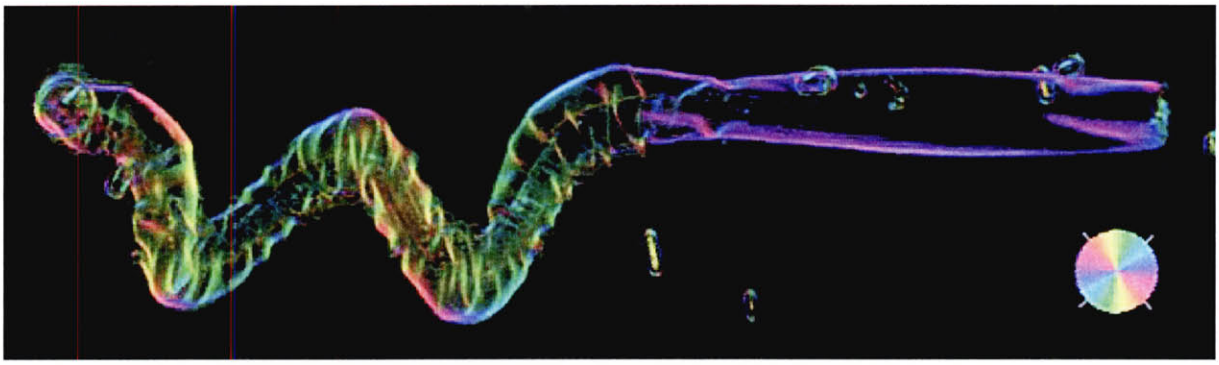

Figure 3.4 Three-dimensional reconstruction of the *Vorticella* stalk from a stack of LCPolScope retardance images. A z-stack of retardance images was collected at 200 nm intervals and reconstructed into a volume using ImageJ software. Background was reduced with a threshold of 60 (out of 256). The retardance slow axis for both the spasmoneme and the sheath signals follows the long axis of the stalk as it coils. The attachment point of the stalk to the coverslip is at the left side of the image. Towards the right side of the image, the portion of spasmoneme normally closest to the cell body has disconnected and withdrawn, leaving an empty portion of sheath. A few bacteria can also be seen.

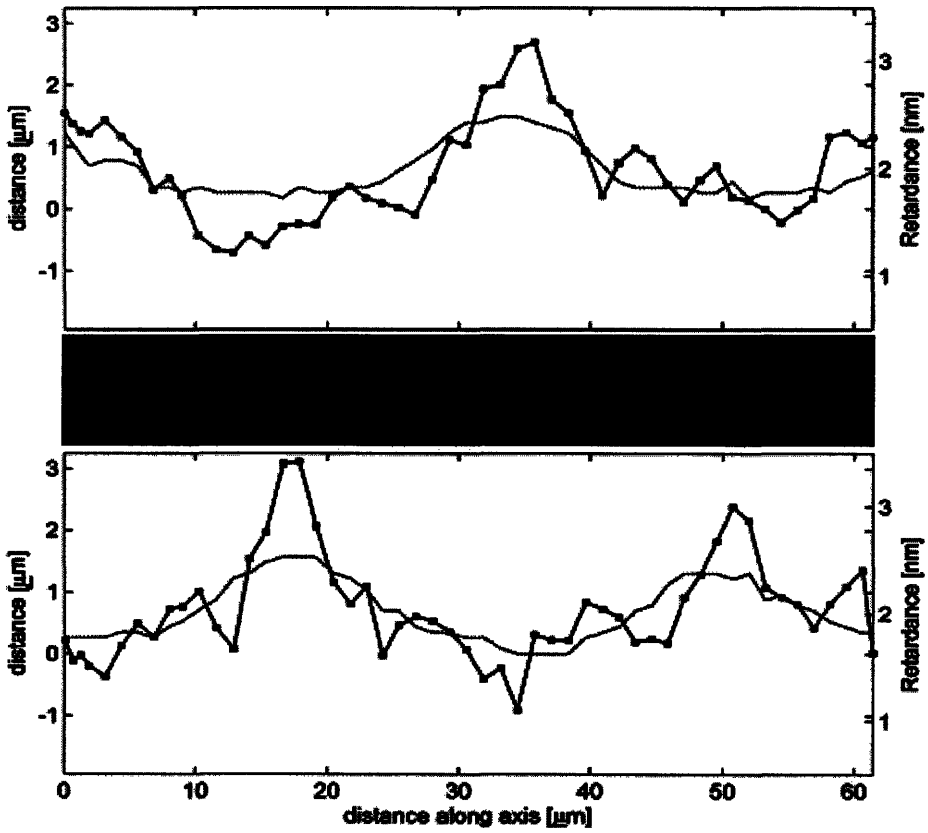

Figure 3.5 Evidence for bâtonnet retardance within sheath, as inferred from LC Pol-Scope images. Intensity varies with distance along the sheath, and is compared at points along the sheath to the distance between that point and the spasmoneme. High sheath intensity corresponds to greater distance from the spasmoneme, indicating areas where the bâtonnet fibers coil through the sheath in an opposite-handed helix to the spasmoneme. **(top panel)** The solid line connects retardance measured at points (circles) along the upper sheath in the image shown in the middle panel; the dotted line shows distance between the upper sheath and the upper edge of the spasmoneme measured at the same points along the length of the stalk. **(bottom panel)** The same schematic is shown for the lower sheath and lower spasmoneme edge.

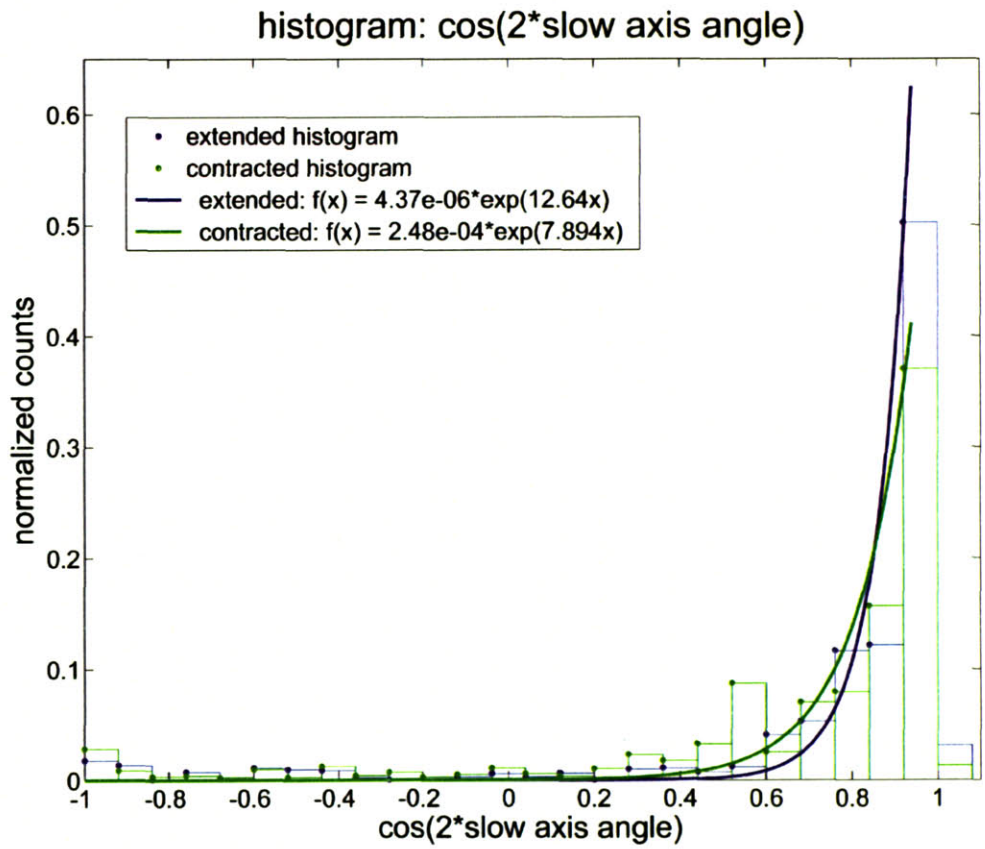

Figure 3.6 Histograms showing distribution of slow axis angles in extended and contracted stalks. Slow axis angle values for all pixels with retardance values greater than 0.5 nm from 16 images of extended cells and 11 images of contracted cells were counted. Fits show that extended cells have slow axis angles which cluster near alignment with the stalk axis (at cos(2*slow axis angle) = 1), while contracted cells have a distribution of slow axis angles which has a greater spread away from alignment with the stalk axis.

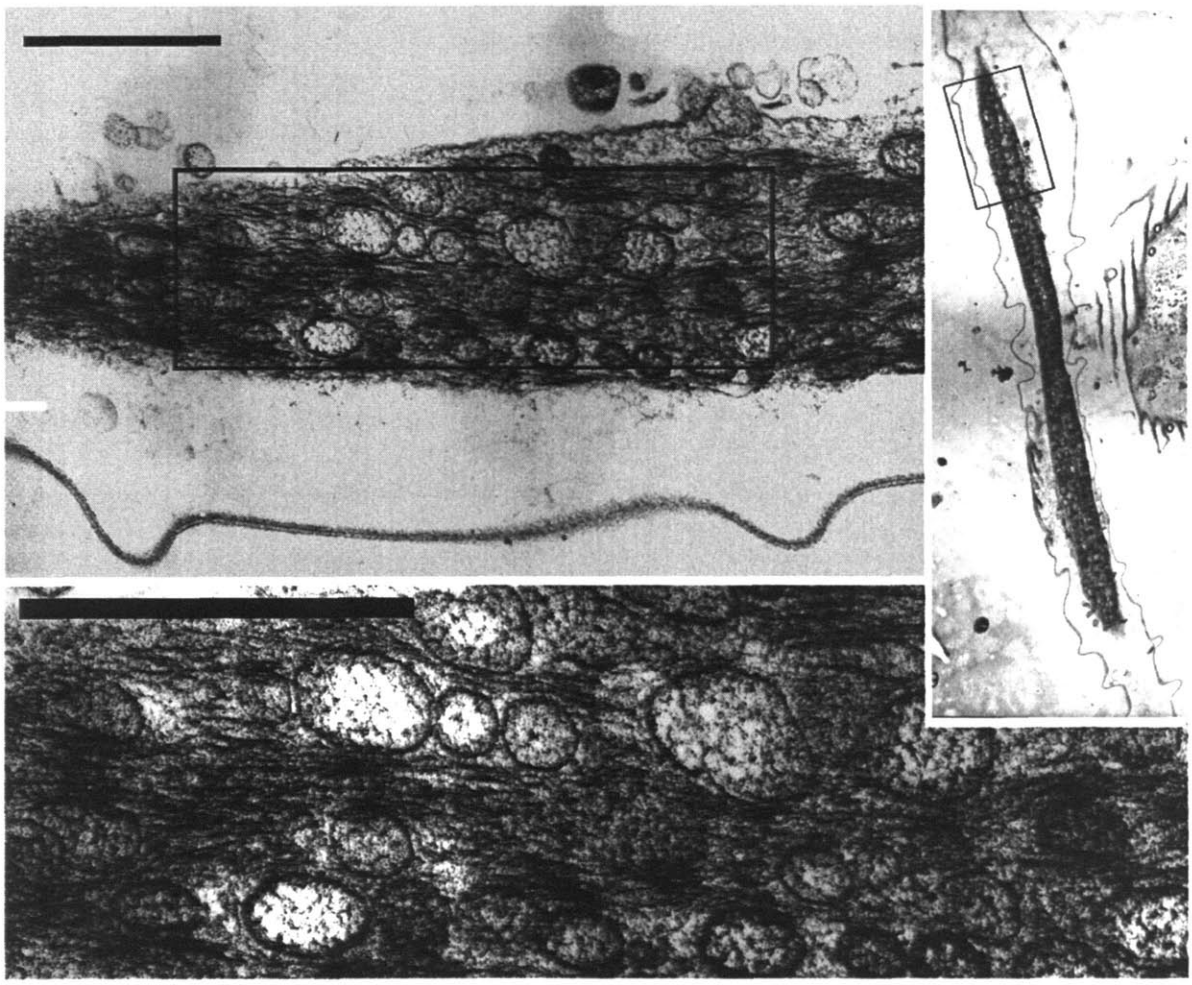

Figure 3.7 TEM images of stalks fixed in the extended state. (inset) Longitudinal section through an extended stalk and (top, bottom) zooming in on extended structure; scale bars = 500 nm.

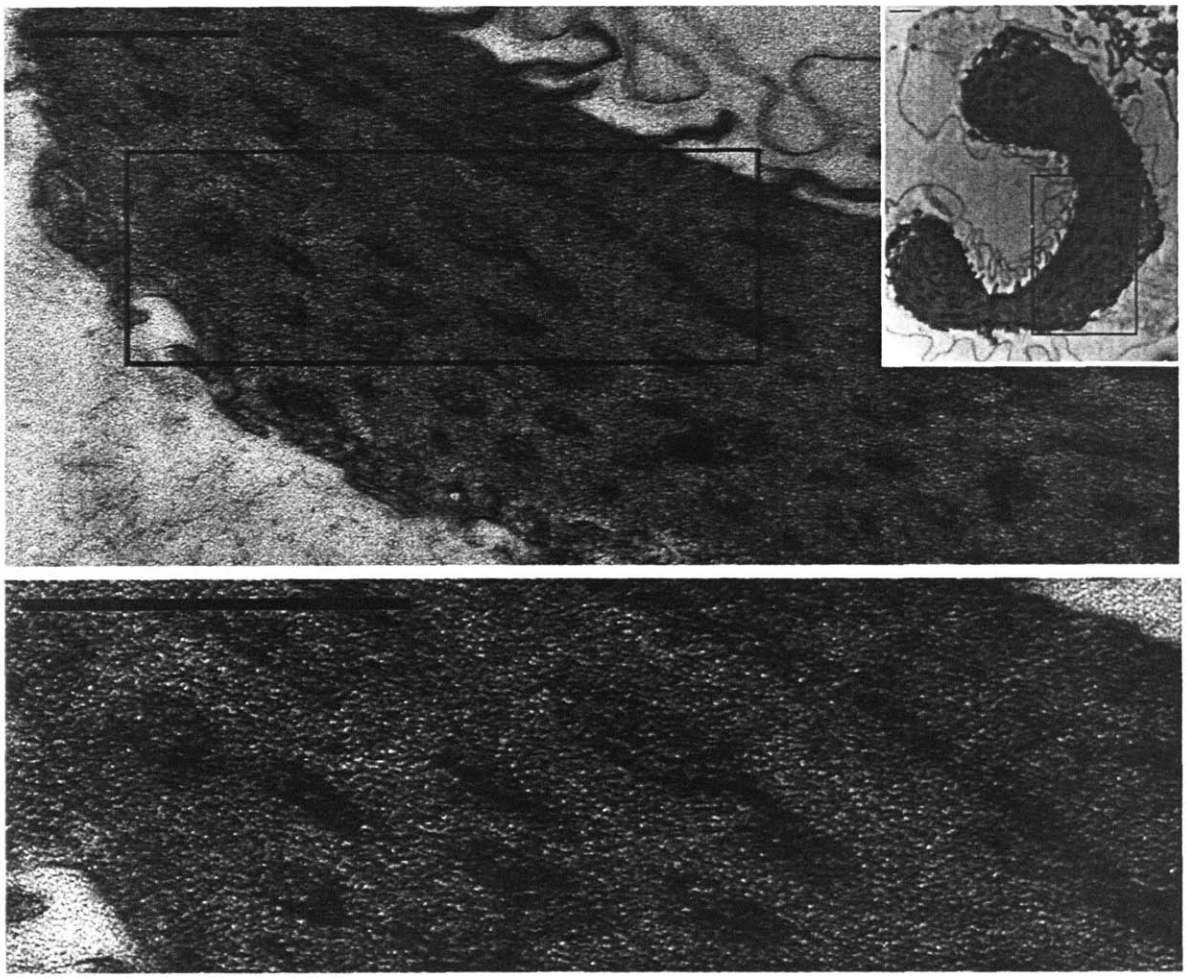

Figure 3.8 TEM images of stalks fixed in the contracted state. (inset) Cross-section through one coil of a contracted stalk and (top, bottom) zooming in on contracted structure; scale bars = 500 nm.

4

Biochemistry and testable hypotheses

4.1. Introduction & Background

That Nature tends not to reinvent the wheel is a common theme in biology. Diverse organisms are known to accomplish relatively diverse tasks by the same essential molecular mechanism; for example, the ATP-dependent conformational changes of the motor protein myosin are used in both the highly evolved contractile mechanism of muscle and in transporting vesicles within cells (Lodish, Berk et al. 2004). Centrin-based motility seems to be no exception to the rule. While centrins form the basis of dramatic cellular movements in organisms like *Vorticella* and *Stentor* (Huang and Pitelka 1973; Ochiai, Kato et al. 1988), they are also responsible for flagellar excision in the green algae *Chlamydomonas* (Salisbury 1998) and are essential for cell division in budding yeast (Kilmartin 2003). Sharing of knowledge about centrin discovered within these various systems makes sense, and the use of information from homologous systems may prove very useful in furthering our understanding of the centrin-based motility seen in *Vorticella* contraction.

The number of components necessary for *Vorticella* motility is an open question. As a calcium-binding protein and the major component of the spasmoneme by weight (Amos, Routledge et al. 1975), it is quite likely that the *Vorticella* centrins and spasmin are critical to

spasmoneme contraction*. There are varying reports in the literature on centrin's ability to form fibers or to actuate structures, with some investigators citing inabilities to coerce purified centrin into fibrous forms (Salisbury 1998) and others claiming to have witnessed centrin self-assembly *in vitro* (Tourbez, Firanescu et al. 2004). The first section of this chapter investigates capabilities of recombinant human centrin 2 on its own *in vitro*; specifically, whether it actually self-assembles into fibers†.

In addition to the evidence presented here on centrin capabilities, there are several other indications that spasmoneme contraction is executed by at least two components. Chemical modifications to tryptophan, methionine, and histidine residues can abolish contractility (Kono, Ochiai et al. 1997); this points to involvement of a second component since the centrin and spasmin sequences do not contain many of those residues. Centrins are soluble, while the spasmoneme as a whole is not; this also points towards a second component, likely to be high in molecular weight and of a structural nature.

The discovery in 2003 of a novel centrin-binding protein in budding yeast led many investigators to the hypothesis that centrin is part of a two-component fiber. The newly discovered protein, Sfi1p, has several conserved repeats along its sequence, each of which is able to bind one molecule of centrin‡ (Kilmartin 2003). The picture emerges of a long Sfi1p backbone decorated along its length by centrin molecules. In 2006, the structure of this two-component fiber system was confirmed by x-ray crystallography and electron microscopy (Li, Sandercock et al. 2006). Sfi1p takes the form of one long alpha helix. Centrins bind to the helix, with each one

* However, its involvement has yet to be definitively proven in *Vorticella* by any sort of deletion assay.
† Other *in vitro* experiments, described in Appendix I, explore whether centrin has the ability to induce contraction in an artificial fiber.
‡ The budding yeast centrin is known as cdc31.

rotated around the helix by about 65° relative to the centrin preceding it and making contacts with its neighbors [Figure 4.4].

Sfi1p homologs are present in a number of species from fungi to humans, and human Sfi1 has been shown to bind CDC31 as well as mammalian centrins (Kilmartin 2003). In 2003, I set out to find an Sfi1p homolog within the newly published *Tetrahymena* genome (TIGR 2003). *Tetrahymena* is a model laboratory organism and a close relative of *Vorticella*, and far more amenable to large-scale cultures for protein purification (Orias 2002). The second portion of this chapter describes the bioinformatics used to search the *Tetrahymena* genome for a Sfi1p homolog, the discovered sequence, and immunolocalization of the found protein.

The chapter closes with a proposed model for centrin-based motility in *Vorticella*, and a framework for testing the model with *in vitro* protein experiments.

4.2. Capabilities of centrin alone

The set of experiments described here characterizes the calcium-dependent self-associations of recombinant human centrin 2. Further experiments which investigate the ability of centrin to actuate engineered structures are described in Appendix I.

4.2.1. Methods

Human centrin 2 (hsCen2) is available from the Salisbury Lab at the Mayo Clinic, as a GST-tagged recombinant protein expressible in *E. coli*. Purification of a few milligrams of hsCen2 was performed according to standard GST protocols outlined by Amersham Biosciences

(Amersham 2004). In brief, *E. coli* containing the GST-hsCen2 plasmid were grown up to exponential phase in 2X YT media with ampicillin, and then expression was induced with 0.33 mM IPTG. After 4 hours of induction, the cells were collected by centrifugation and lysed by sonication. The lysis mixture was centrifuged to remove cellular debris, and then the supernatant was batch incubated with Glutathione Sepharose 4 Fast Flow. After washing off unbound protein, centrin was eluted by cleavage from the bound GST using Amersham's proprietary PreScission Protease. GST was then released from the sepharose medium with 10 – 50 mM reduced glutathione. It was relatively straightforward to acquire about 1 mL of pure protein at a concentration of 5 mg/mL using this method.

Dynamic Light Scattering (DLS) is a well-known technique for determining approximate molecular sizes. The autocorrelation of scattered light through a sample of particles falls off at a time scale which is characteristic of the diffusion velocity of the particles; if the particles are assumed to have a certain approximate geometry (spheres or elongated rods, for example), the dimensions of the particle can be calculated from their diffusion velocity. Thus the output from a DLS experiment is a histogram showing relative percentages of differently sized particles in the sample.

The DLS measurements described here were made on a DynaPro Molecular Sizing Instrument and Dynamics V6 Software [Protein Solutions, Piscataway, NJ]. Experiments were designed to mimic the conditions used by Tourbez and colleagues as reported in 2004 (Tourbez, Firanescu et al. 2004). The same buffer, protein, and calcium concentrations were used. Samples of purified hsCen2 (~3.4 mg/mL in buffer A: 50 mM Bis-Tris, 20 mM KCl, pH 7.1) were centrifuged at 200,000g for 15 minutes to remove any extraneous impurities. DLS measurements were taken at 20°C. Calcium and magnesium were then added to final concentrations of 0.88

mM Ca^{2+} and 1.85 mM Mg^{2+}, and the DLS measurements were taken again after waiting 10 minutes for polymerization to equilibrate. Finally, the sample was spun again at 200,000g to remove proteins which had polymerized. A sample of the supernatant was then re-examined by DLS. The pellet was examined under the transmission electron microscope.

Standard protocols were used to stain the pellet of hsCen2 plus Ca^{2+} and Mg^{2+} obtained in the DLS experiments. The proteins were adsorbed to a formvar on copper grid for 30 seconds, and then stained with 2% uranyl acetate in water for 30 seconds. After drying, grids were examined on a Jeol 1200EXM transmission electron microscope operating at 60 kV.

4.2.2. Results

The first set of experiments on purified hsCen2 explored its ability to self-assemble into fibers, as had been claimed by Tourbez *et al.* on the basis of light scattering observations of concentrated (~3.4 mg/mL) hsCen2 in the presence of high (1-2 mM) calcium concentrations (Tourbez, Firanescu et al. 2004). Dynamic light scattering experiments were conducted to verify the development of large molecular aggregates upon the addition of calcium. Indeed, as shown in Figure 4.1, the population of molecules within the hsCen2 sample shifted from consisting almost entirely of 3 nm diameter, 42 kDa proteins (hsCen2 dimers) to containing many larger particles of indeterminate size[§]. The large aggregates were collected by ultracentrifugation, stained, and visualized by transmission electron microscopy, showing that the aggregates were not fibrous in form. The unaggregated proteins remaining in solution after ultracentrifugation consists are centered around a diameter of 3.6 nm, slightly larger than the 3 nm molecules in the sample

[§] DLS measurements are only valid for particles much smaller than the wavelength of light used for the scattering measurement. Larger aggregates whose size approaches the wavelength are not reliably measured by this method.

before aggregation. The increase in diameter is likely due to the known conformational change of centrin from a closed to an open configuration upon binding calcium (Durussel, Blouquit et al. 2000). The increase in molecular weight is therefore just indicative of the increase in diameter, and does not indicate an actual weight increase, since it is calculated on the assumption that the molecule is spherical.

Centrin aggregates in high calcium: **Figure 4.1**

4.3. Search for an Sfi1p homolog in *Tetrahymena thermophila*

4.3.1. Methods and results

Kilmartin's discovery of Sfi1p as a centrin binding partner in yeast immediately fueled interest in finding its ciliate homologue. The lack of published data on *Vorticella* proteins led us to examine a better-known organism, *Tetrahymena thermophila.* GenBank holds 800 *Tetrahymena* protein sequences and 9862 ESTs. Earlier BLAST (NCBI) searches done to replicate Kilmartin's results had not turned up any *Tetrahymena* proteins so I did a first pass through these sequences with the program PatScan (Overbeek 1995), which parsed all GenBank sequences with the Sfi1p consensus pattern: A-X_{12}-F/L-X_2-W-K/R/H*. This turned up seven proteins and sixty-one ESTs, but none possessed the same conserved repeat structure as seen in Sfi proteins.

* This pattern reads as follows: alanine, followed by any 12 amino acids, then phenylalanine or leucine, followed by any 2 amino acids, then tryptophan and either lysine, arginine, or histidine. No gaps or deletions are allowed. The corresponding DNA pattern was used for EST scans: GC (A/C/G/T) 36...36 (TTA/TTG/CTT/CTC/CTA/CTG/TTT/TTC) 6...6 TGG (CAC/CAT/AAA/AAG/CGT/CGC/CGA/CGG/AGA/AGG).

Having exhausted the known *Tetrahymena* sequences, I turned to the rough new genome for information[∅] (TIGR 2003). After fruitless BLAST searches with each of five Sfi protein sequences [see Appendix II], I again turned to Patscan. The same DNA pattern as above was made more specific with *Tetrahymena* codon biases and used to scan the entire unannotated genome. I sorted the 256 matches into those on the same contig; then, using Sixpack (EMBOSS), I translated the contigs with the greatest number of matches in all six reading frames[♥], and found all possible open reading frames (ORFs)[♠]. The ORFs were fed into PattinProt (PBIL), which can find sequences that match a pattern with as low as 50% similarity[⊗]. Manual scans of the PattinProt results for ORFs with multiple repeats of high similarity uncovered one strong pattern, similar to the Sfi1p pattern but more highly conserved [Figure 4.2]. A BLAST search with this new stronger repeat picked out two more similar sequences from the *Tetrahymena* genome.

In order to design antibodies, it was first necessary to remove any potential introns from the raw DNA sequences. While *Tetrahymena* retains the normal conserved splice sites (AG and GT) (Csank, Taylor et al. 1990), methods to more accurately determine introns, such as those used for the human genome, have not yet been developed. It proved futile to attempt to find the introns in two of the three found sequences, which were both in the middle of a contig with more than a million base pairs and contained introns of at least a few thousand base pairs. Luckily the third sequence was on a contig of only 1108 base pairs, so it was a far easier task to manually assess the possible introns and come up with those that maintained the right reading frame for the repeats and created a stop codon before the end of the contig [see Appendix II]. As a control I

[∅] Preliminary sequence data was obtained from The Institute for Genomic Research at http://www.tigr.org.
[♥] Translations were done according to the *Tetrahymena* genetic code, which differs from the human code only in that TAA and TAG are not stop codons but instead code for glutamine.
[♠] Sixpack defines an ORF (open reading frame) as any possible translation between two stop codons.
[⊗] I had previously used PattinProt to successfully rediscover the same repeats Kilmartin cited in the Sfi protein.

BLASTed these newly found sequences against the known GenBank ESTs and protein sequences to see if they were already known; I did not find any matches, so it is safe to assume that these are unexamined sequences. I also ran the sequences through Pfam (Institute) and found that they contain several TPR domains, which are implicated in protein-protein interactions. This and a preliminary highly α-helical structural prediction[⊕] are positive indicators that these sequences code for a Sfi1p homolog protein that can also form a fibrous backbone for *Tetrahymena* centrin.

Discovered homologous repeats in *Tetrahymena* genome sequence: **Figure 4.2**

Antibodies for three different regions of this found sequence – the repeats and the N-, and C-termini – were produced in rabbits by Invitrogen Corp. [Carlsbad, CA]. Upon receipt, antibodies were purified from the serum by passage over a protein A column [HiTrap™ Protein A HP, 17-0403-01, Amersham Biosciences, Uppsala, Sweden], according to standard procedures, and then concentrated by centrifugation over a membrane with molecular weight cutoff of 30 kDa [Vivaspin, 20 mL, Vivascience AG, Hannover, Germany]. Preparation for immunofluorescence microscopy was carried out in *Tetrahymena* according to standard procedures (Orias, Hamilton et al. 1999). Immunostaining of *Tetrahymena* with these antibodies has revealed their colocalization with centrin antibodies in the basal body structures lying just underneath the cellular membrane [Figure 4.3]. Such colocalization is a promising indication that I have found a

[⊕] Structural prediction performed with web tool at **http://www.cmpharm.ucsf.edu/cgi-bin/nnpredict.pl**

protein which is structurally involved with centrin. The next step is to use the same antibodies to immunoprecipitate the Sfi1p homolog and investigate its properties.

Co-localization of Sfi1p homolog and centrin in *Tetrahymena*: **Figure 4.3**

4.4. Testable hypotheses and future work

4.4.1. A proposed model for *Vorticella*'s contractile mechanism

The experiments outlined in this thesis, conducted at both the cellular and molecular levels, provide several pieces of evidence that constrain a model for the mechanism of *Vorticella* contraction. The persistence of birefringence throughout contraction and its spatial correlation with nanometer-scale fibers indicates that these fibrous components are the agents responsible for executing contraction. The inability of centrin to form such fibers on its own points towards the involvement of a separate structural component. By homology with yeast studies, that structural component is likely to be Sfi1p. The discovery, in another ciliated protozoan, *Tetrahymena*, of a colocalizing protein with homologous sequence to Sfi1p, strengthens this hypothesis. Therefore, at this stage, the best clues into the true contractile mechanism of *Vorticella* come from examining the physics of interacting rod-like proteins whose surface chemistry is described by the properties of centrins in solution and the crystal structures of the yeast centrin-Sfi1p complex.

Two models which have previously been proposed – the rubber-like entropic spring (Amos 1972; Moriyama, Okamoto et al. 1999) and the coiling fiber (Salisbury 2004) – involve drastic structural changes within the constituent polymeric subunits of the spasmoneme. Persistent

birefringence rules out these drastic structural changes, but another piece of evidence is the lack of large conformational differences seen by Li *et al.* between the crystal structures of centrin-decorated Sfi1p fragments with and without bound Ca^{2+} (Li, Sandercock et al. 2006). The evidence points to a mechanism which relies on the interactions between rod-like centrin-Sfi1p complexes, rather than large conformational changes within each complex.

The arrangement of fibers in the extended state, as seen in TEM images [Figure 3.7], is likely to come from electrostatic repulsion between the highly negatively charged structures [Figure 4.4]. The Debye length in cytoplasmic fluid is likely to be on the order of one nanometer, and as a rule of thumb, the repulsive forces will be noticeable at about five times the Debye length, or five nanometers (Israelachvili 1992). The assumption is therefore that rod-like subunits are packed into the spasmoneme at such a high density that they are forced to lie as closely together as electrostatic repulsion will allow, and will tend to be ordered along the long axis of the spasmoneme due to the gain in translational freedom that such ordering confers.

An electrostatic mechanism has long been popular for *Vorticella* contraction, due mainly to the negative surface charge of spasmin and centrin; the pI ~ 4.7 – 4.8 for spasmin, for example, was established in the 1970s (Routledge, Amos et al. 1976). Experiments were done early on to test the effectiveness of monovalent salt ions in screening such surface charges and thereby also inducing contraction; it was found that monovalent ions cannot cause collapse and that the calcium thresholds for contraction remain the same in high salt concentrations. It may seem strange that the contractile mechanism could be based on an electrostatic repulsion which cannot be reduced by charge screening, but there is precedence for a similar phenomenon between actin filaments. At high concentrations (~ 3.7 mM) induced by ultracentrifugation, negatively charged (pI ~ 5.3 (Karakozova, Kozak et al. 2006)) actin filaments repel each other at a minimum center-

to-center distance of 10-12 nm, which cannot be decreased by monovalent salt screening. Since the diameter of an actin filament is about 7 nm, this center-to-center distance corresponds to an interfilament spacing of about 5 nm. However, addition of Mg^{2+} reduces the distance to 7 nm, indicating that Mg^{2+} acts as an ionic cross-linker which can bridge adjacent filaments and bring them closer together (Matsudaira, Mandelkow et al. 1983). Also, other divalent ions besides calcium can contract the spasmoneme, just not to the same degree; the best ones (Eu^{3+}, Tb^{3+}) are the same ionic radius as calcium (~ 0.1 nm). This implies some specificity for the binding pocket in centrin, but that divalency is the most important condition (Yokoyama and Asai 1987).

Besides electrostatic repulsion, another intermolecular force which may come into play is hydrophobicity. Gains in hydrophobicity have been detected in purified hsCen2 as it binds calcium and changes conformation to expose a hydrophobic patch (Wiech, Geier et al. 1996; Durussel, Blouquit et al. 2000). In addition, when that patch is blocked by a hydrophobic fluorescent probe molecule (ANS), calcium-dependent centrin aggregation is blocked (Tourbez, Firanescu et al. 2004). However, as mentioned above, when yeast centrin is bound to Sfi1p, it appears to undergo very little conformational change upon binding calcium (Li, Sandercock et al. 2006). There is also no remarkable increase in non-polar (white) regions in the molecular surfaces shown in Figure 4.4. However, my recent studies with purified human centrin 2 showed aggregation (not filament formation) in high calcium – indicating that centrin can form two kinds of contacts: centrin-centrin contacts which are stabilized by the Sfi1p backbone, and centrin-centrin contacts which are mediated by calcium. These calcium-mediated contacts could involve both ionic cross-linking, as discussed above, and hydrophobic interactions.

Surface charge of centrin-Sfi1p complexes: **Figure 4.4**

Finally, it is possible that as filaments get close enough together (~ 1 nm), van der Waals forces could significant enough to aid in bringing the filaments into more direct contact.

The arrangement of filaments in the contracted state is more difficult to ascertain in TEM images [Figure 3.8]. There is obvious twist within the contracted spasmoneme, a structural parameter which also manifests itself in the rotations of the cell body after contraction (see Introduction). If the assumption is that centrin-Sfi1p complexes pack together due to ionic cross-linking or hydrophobic interactions, or both, making centrin-centrin contacts, then the geometry of packing could feasibly be helical. Centrins bind to repeats along the Sfi1p which are spaced in such a way that one centrin is rotated around the backbone with respect to its neighbors. The helically-decorated complexes appear relatively flexible in rotary shadowing EM images (Li, Sandercock et al. 2006), with a persistence length on the order of the length of the fiber (~ 60 nm). They may be held in a more rigidly straight conformation due to electrostatic repulsion in the extended state, yet have the flexibility to form helical associations when calcium is added. While the packing density and stiffness of the complexes is not likely to allow one complex to wrap a full turn around another complex, the degree to which they can associate helically may be enough to explain the twist seen in TEM images, as well as the difficulty in resolving individual fibers.

Proposed model schematic: **Figure 4.5**

In this model, molecular-level interactions easily scale up to shortening of the spasmoneme overall. The spasmoneme is an elongated sack containing the interacting filaments and

constrained along its length to the extracellular sheath**. Increased twist and generally closer lateral and longitudinal molecular associations within the substructure would translate into shortening of the organelle, consistent with our high-speed polarization videos of contraction, wherein the stalk shortens and takes the shortest path through the stalk before coiling with the structure as a whole. The situation proposed for the *Vorticella* stalk therefore is that twist and shortening of the spasmoneme are translated into an overall coiling of the stalk through the mechanical constrictions imposed by connections to, and stiffening proteins (the bâtonnets) within, the extracellular sheath.

How would such a molecular-scale model manifest itself on the sub-micron scale which we can observe with birefringence? As stated above, birefringence would maintain the same direction, changing only slightly in degree of ordering, because the long axes of helically-associated filaments would still be largely in the same direction. Periodicities across or along the spasmoneme may be due to longer-range organization inherent in the contractile mechanism, or simply due to positioning of other cellular structures, such as the tubules which run throughout the spasmoneme.

This model, involving centrin bound to Sfi1p, independently of calcium, with calcium-dependent centrin-centrin contacts bringing filaments together, is similar to the model proposed by Martinez-Sanz et al. for contraction of basal body associated fibers (Martinez-Sanz, Yang et al. 2006).

It may be possible in the near future to recreate and test the proposed interaction scheme *in vitro*, using purified rod-like protein complexes made up of *Vorticella* centrin, spasmin, and

** This constraint is demonstrated by the observation of local coiling in response to local contraction, as witnessed in reponse to calcium electrospray (Ochiai *et al.*, 1983).

other constituent proteins. In the meantime, studies in the homologous yeast spindle pole body system are consistent with the theory of interacting rods presented above. Purified rods (~350 kDa, 5 x 60 nm) of an alpha-helical structural protein (Sfi1p) decorated with yeast centrin (Cdc31p) do not appear to intrinsically change shape upon the addition of calcium, indicating that their function in motility may lie in the interactions of such rods with each other (Li, Sandercock et al. 2006).

4.4.2. Future Work

4.4.2.1. Testing the model *in vitro* with proteins

The model proposed above hinges on the interactions of rod-like protein complexes with each other. Therefore future work should focus on characterizing the surface chemistry of these complexes and exploring the phenomena of their interactions in solution. Because these phenomena are expected to be highly concentration-dependent, the first set of experiments should explore protein interactions throughout a range of concentrations.

Figure 4.6 presents the framework for experiments exploring the concentration-dependent interactions of centrin-Sfi1p complexes in solution. The complexes themselves can be the centrin-decorated 15-repeat Sfi1p fragments described by Li, *et al.*, in their 2006 paper on centrin-Sfi1p structures from yeast[††]. Protein interactions will be measured by an order parameter, such as birefringence or retardance of the sample according to techniques similar to those described in Chapter 3. At low concentrations, the addition of calcium should make no significant change to ordering of the system, since the rods have enough freedom of movement to attain a randomly dispersed set of configurations. At very high concentrations, rods should

[††] These complexes are available from the Kilmartin laboratory as GST-tagged constructs expressed in *E. coli.*

behave as they do within the spasmoneme; that is, they will be ordered without calcium due to entropic constraints on their rotational freedom and will remain ordered in the presence of calcium due to the same entropic constraints as well as lateral/helical associations between rods. The most revealing behavior may occur at intermediate concentrations. Here, the rods without calcium will be at a high enough concentration that they will tend towards the aligned state. As calcium is added, effective volume of each rod drops, and these "smaller" rods will be at a low enough concentration to move into random orientations.

Such an experiment can be carried out in two ways. One way would involve examining the centrin-Sfi1p complexes with or without calcium throughout a range of concentrations, generating separately the two sigmoidal curves shown in Figure 4.6. A second way would be to add calcium to the complexes at various concentrations, examining whether a change in the ordering metric occurs, thereby generating the two sigmoidal curves at once.

Proposed experimental framework: order vs. concentration: **Figure 4.6**

4.4.2.2. Testing the model in nanoscale or microscale devices

Preparation of very highly concentrated protein samples for experiments such as the one described above is not a trivial matter, and it would be wise to take advantage of technologies which enable the use of small amounts of material at high concentrations. One such technology is electrospinning, as described in Appendix I. It is possible to electrospin coaxial fibers (Dzenis 2004; Jiang, Hu et al. 2005), as depicted in Figure 4.7. Such fibers could use a spinnable polymer, such as poly(ethylene oxide), to form the outer sheath while keeping the interior

solution of protein complexes in aqueous phase. The studies described in Appendix I have proven that it is possible to spin proteins (human centrin 2 was used) concentrated to hundreds of milligrams per milliliter under conditions (physiologic buffers at neutral pH) which favor retention of their native structures and activity.

Coaxial electrospinning: **Figure 4.7**

The coaxial fiber structure that would be generated by such an experiment is one that closely mimics the actual size and structure of the spasmoneme. Electrospun fibers are generally less than a micron in diameter, so the spun fibers would be of the same size as the spasmoneme. The coaxial structure, with a polymeric sheath surrounding the contractile element, is analogous to the extracellular sheath enclosing the spasmoneme.

A number of schemes can be imagined for observation of shape changes in electrospun fibers upon the addition of calcium. The simplest scheme may be to let the fibers deposit as a random meshwork on the anode, as they naturally tend to do, and then add calcium ions in solution. Calcium will diffuse through the polymeric network of the coaxial sheath and actuate the centrin-Sfi1p complexes contained within the core. As fibers change shape in response to calcium, they will pull at the nodes in the network where fibers overlap, and thereby shrink the pores of the fibrous network. The decrease in pore size will be the metric which quantifies the shape changes due to addition of calcium.

4.5. Conclusion

Knowledge of the *Vorticella* motility at the molecular scale is limited, but can be informed by studies carried out in homologous systems. This chapter has demonstrated that a few key biochemical experiments, in conjunction with careful analysis of the literature of homologous contractile proteins, have the power to connect cellular level measurements with molecular level hypotheses. It was demonstrated that centrin cannot form filaments on its own, and that a likely candidate for the major filamentous component of the spasmoneme is a homolog to the yeast centrin-binding partner Sfi1p.

Integration of these simple facts with the findings from Chapters 2 and 3 from this thesis led to a model of *Vorticella*'s contractile mechanism which hinges on the interactions of rod-like protein complexes with each other, and proposes how the addition of calcium could power movement over hundreds of micrometers. The important groundwork has been laid for testing this model through *in vitro* biochemical experimentation.

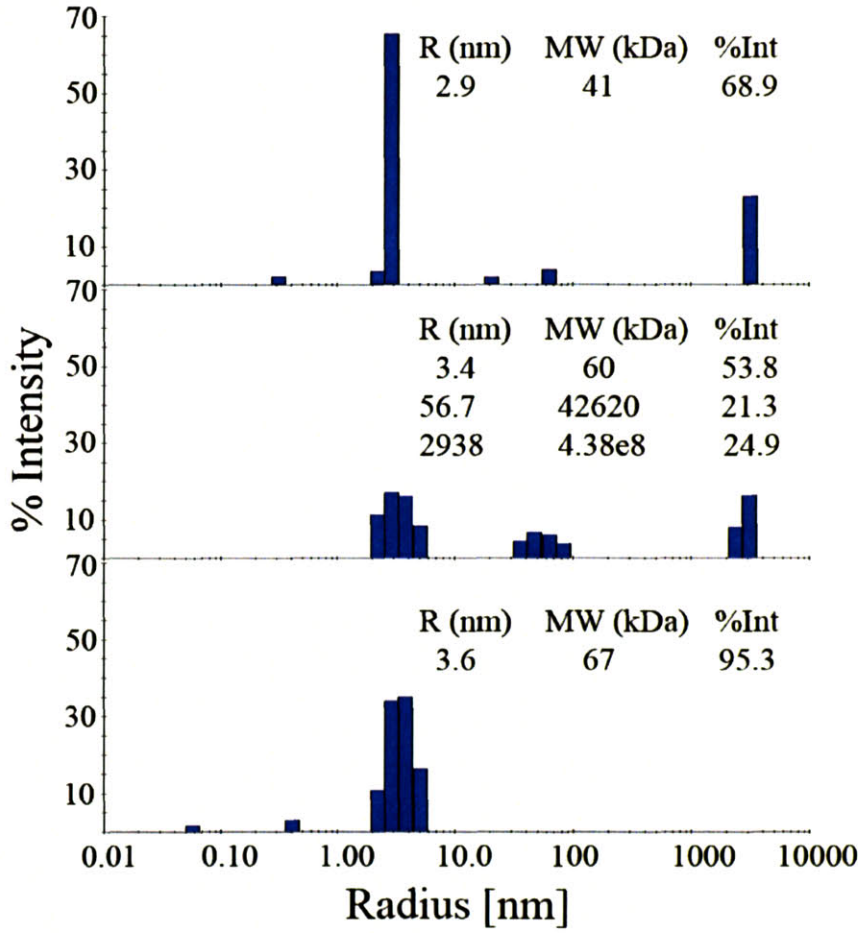
% Intensity
70
50
30
10
R (nm) MW (kDa) %Int
2.9 41 68.9
R (nm) MW (kDa) %Int
3.4 60 53.8
56.7 42620 21.3
2938 4.38e8 24.9
R (nm) MW (kDa) %Int
3.6 67 95.3
0.01 0.10 1.00 10.0 100 1000 10000
Radius [nm]

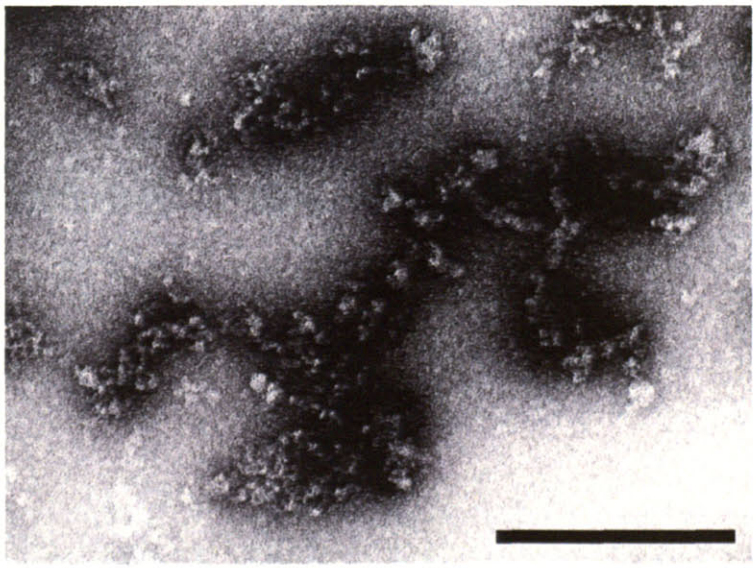

Figure 4.1 **(top)** Data obtained from dynamic light scattering measurements on the aggregation process of purified human centrin 2 (hsCen2) in the presence of high calcium. (top histogram) Purified hsCen2, ~ 3.4 mg/mL and dimerized, is monodisperse (high MW peak is likely dust or some other contaminant), with a spherical equivalent radius of ~ 2.9 nm, and spherical equivalent molecular weight of 41 kDa. (middle histogram) When calcium and magnesium ions are added, hsCen2 aggregates into several larger species. (bottom histogram) After aggregated species are spun down out of the sample by ultracentrifugation (200,000g, 15'), the sample is again monodisperse, with a spherical equivalent radius of ~ 3.6 nm, and spherical equivalent molecular weight of 67 kDa. Centrin is likely still dimerized and in a more elongated configuration, leading to the higher apparent radius and molecular weight. **(bottom)** Transmission electron micrograph of aggregated hsCen2 plus 0.88 mM Ca^{2+} and 1.85 mM Mg^{2+} within the pellet spun down from the supernatant shown in the bottom histogram of the top panel. The aggregated structures are not fibrous. Scale bar = 500 nm.

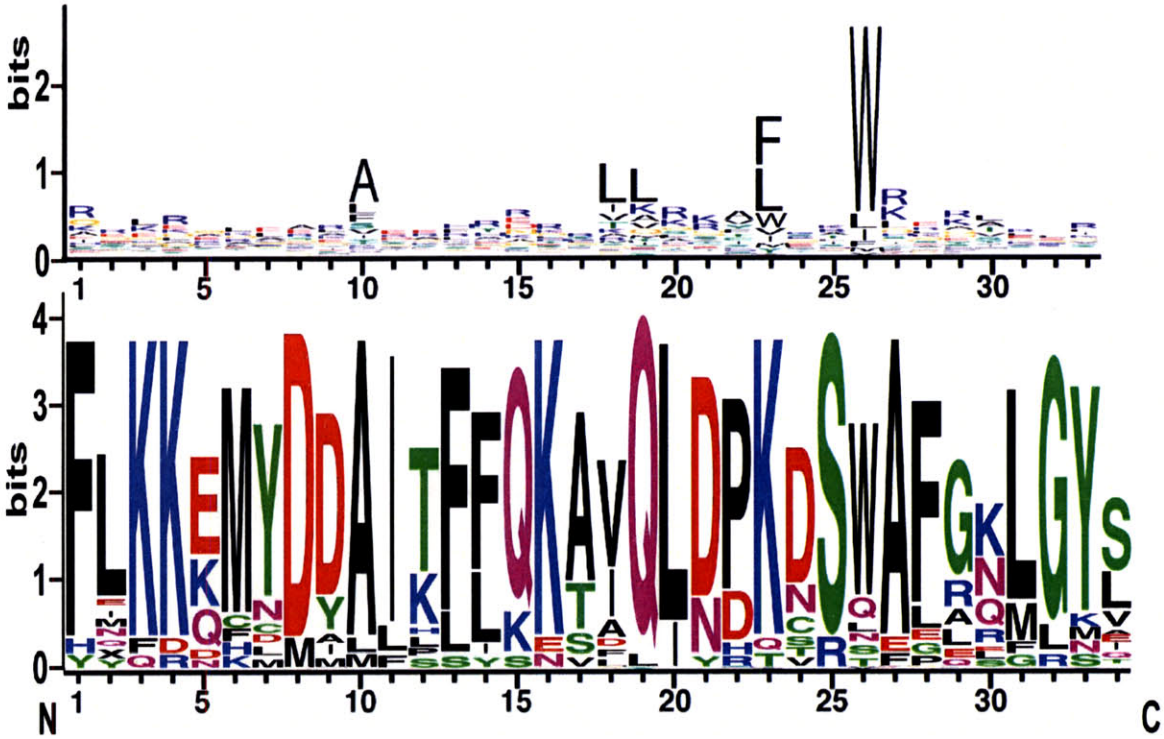

Figure 4.2 Sequence logos for conserved Sfi1p repeats. **(top)** Sequence logo for 454 Sfi1p repeats from 23 different organisms. Reproduced from (Li, Sandercock et al. 2006). **(bottom)** Sequence logo for all repeats within the homologous sequence found in the *Tetrahymena* genome. Both logos were calculated using the web-based tool available at http://weblogo.berkeley.edu/logo.cgi (Crooks, Hon et al. 2004).

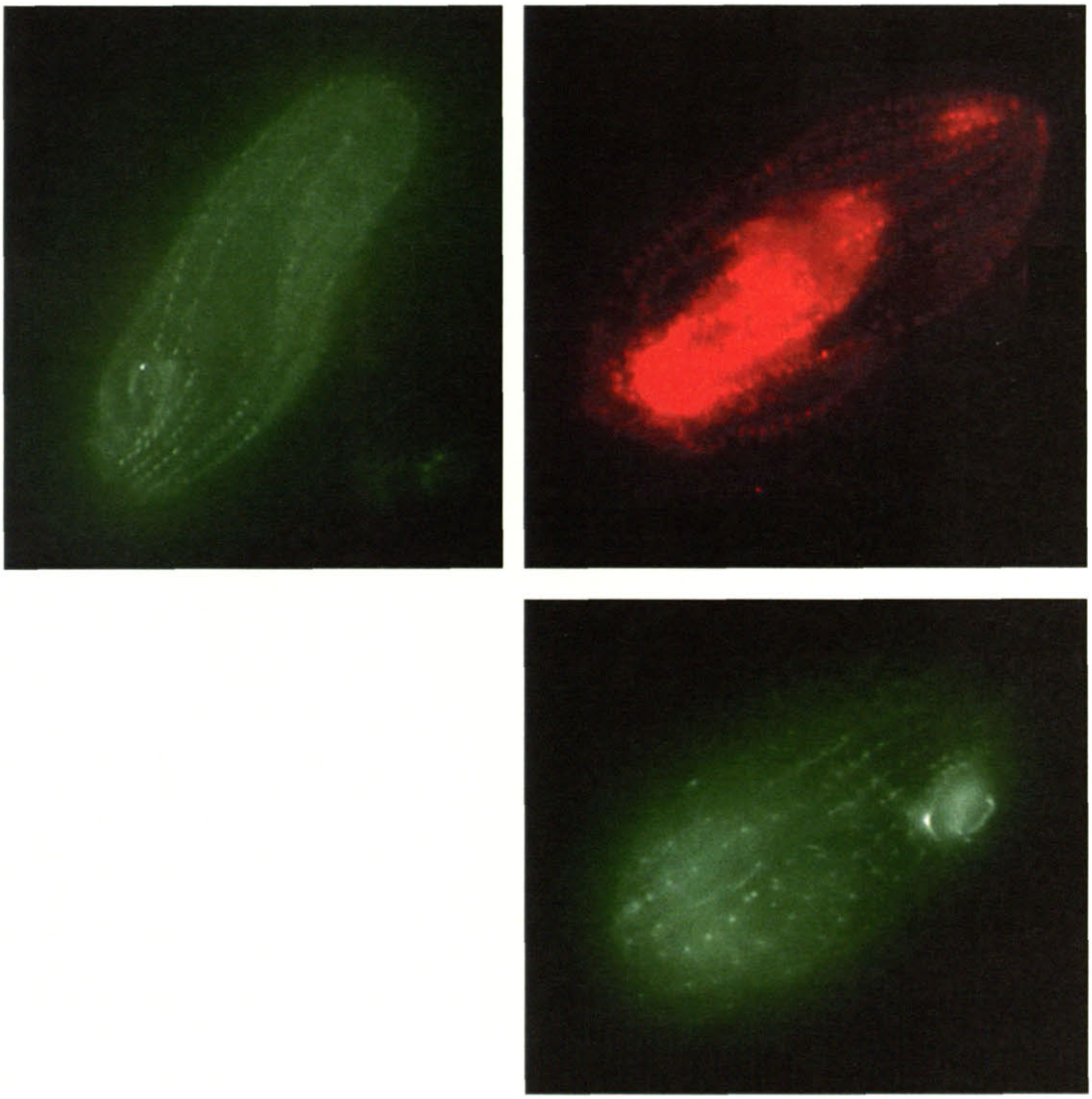

Figure 4.3 Colocalization of centrin and the found Sfi1p homolog sequence in *Tetrahymena thermophila*. **(top left)** Localization of antibody 1 against C-terminus of found sequence. **(top right)** Localization of antibody 2 against C-terminus of found sequence. **(bottom right)** Localization of antibody against *Vorticella* centrin 5. All three antibodies localize to the basal bodies of *Tetrahymena*, structures at the base of each cilium which are known to contain centrin (Guerra, Wada et al. 2003).

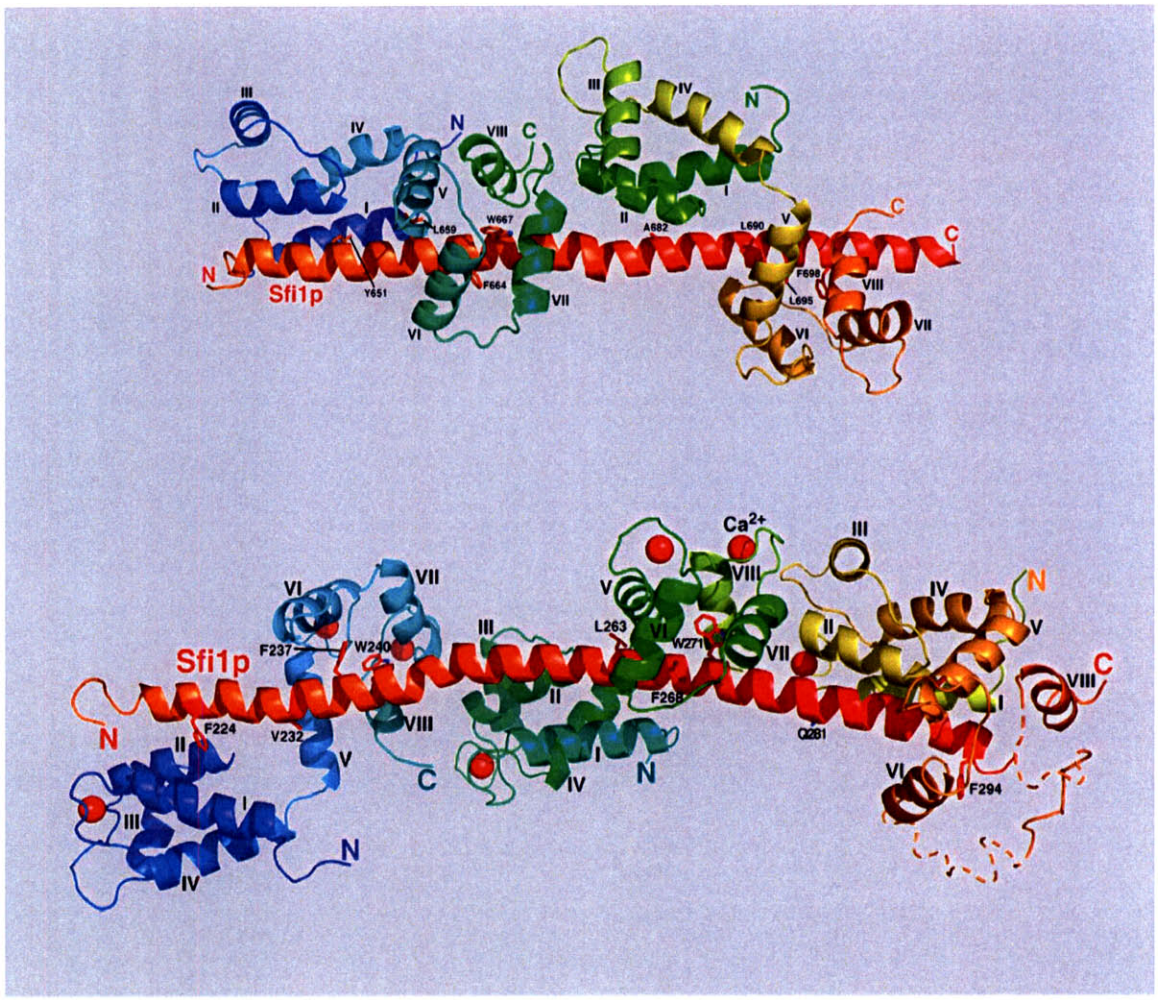

Figure 4.4 Structure and surface properties of centrin-Sfi1p complexes from yeast.

(a) Protein data bank structures 2GV5 (top) and 2DOQ (bottom) displayed as backbone ribbons. 2GV5 shows two centrins bound to a fragment of Sfi1p (red helix). 2DOQ shows three centrins bound to a longer fragment of Sfi1p (red helix) as well as six bound calcium ions (red spheres). The alpha-helices and N- and C-termini of each centrin molecule are labeled. Figure reproduced from Li *et al.*, 2006.

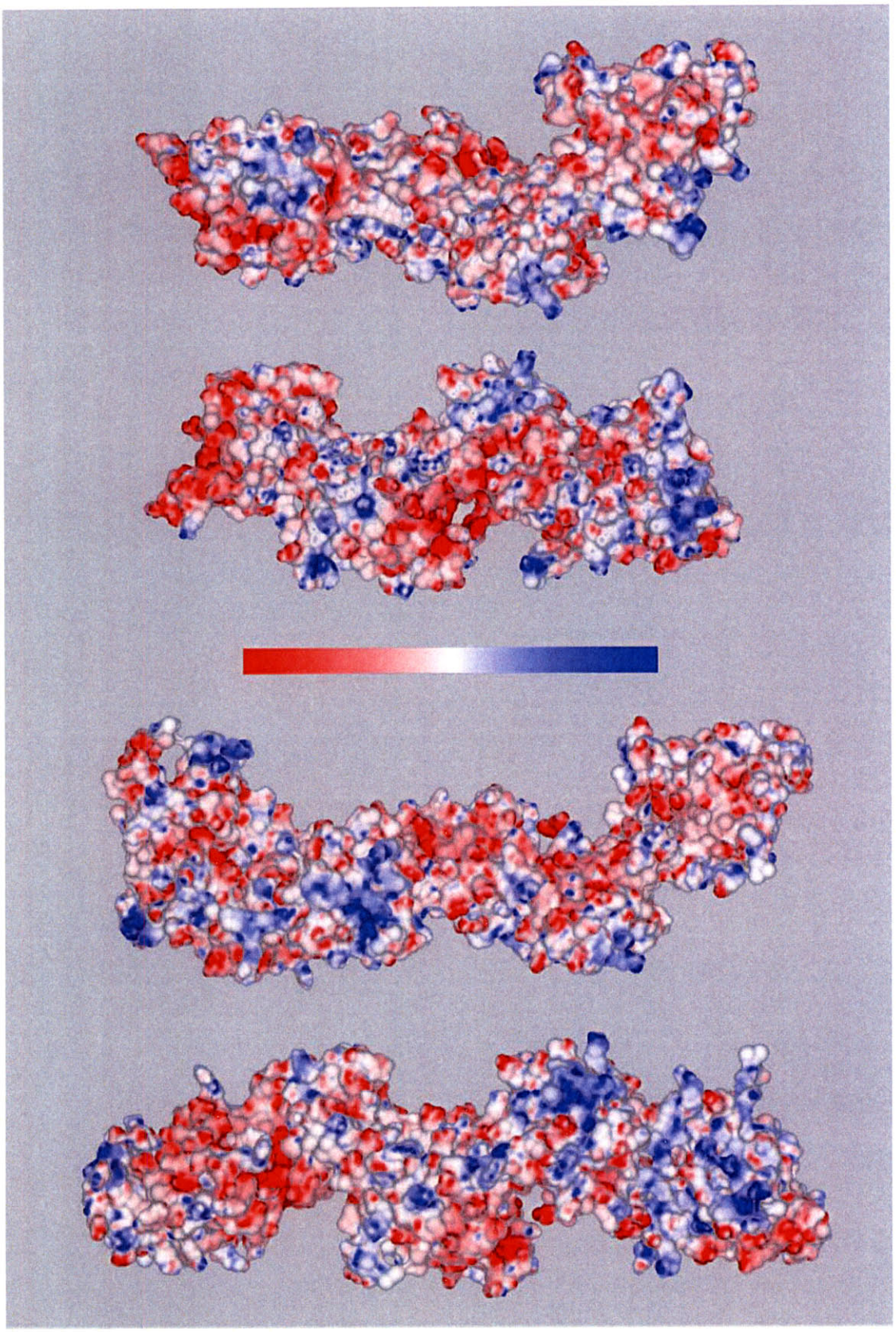

Figure 4.4 Structure and surface properties of centrin-Sfi1p complexes from yeast.

(b) Protein data bank crystal structures 2GV5 (top) and 2DOQ (bottom) displayed as electrostatic surfaces. Structure 2GV5 consists of two centrins bound to a fragment of Sfi1p. Structure 2DOQ consists of three centrins bound to a longer fragment of Sfi1p as well as six bound calcium ions. Each structure is shown in two orientations which differ by a rotation of 180° of the molecule around its long axis. The colorbar at left runs from a minimum of -235 mV (-10 k_BT/e) surface potential (red) through neutral (white) to a maximum of +235 mV (+10 k_BT/e) (blue). The electrostatic potential surfaces were calculated using a modified version of the DelPhi software package (Gilson, Sharp et al. 1988; Sharp and Honig 1990), called GRASP (Nicholls, Sharp et al. 1991), which solves the linearized Poisson--Boltzmann equation on a 129 x 129 x 129 grid centered over all the atoms. The program MSMS (Sanner, Olson et al. 1996) was used to obtain a triangular mesh of the solvent boundary with the molecular surface using a solvent probe radius of 1.4 Å (Connolly 1983) and a 2.0 Å ion-excluding Stern layer. The following parameters were used: molecular dielectric, $\varepsilon = 4$; solvent dielectric, $\varepsilon = 80$; salt concentration = 0.145 M. The PARSE parameter set (Sitkoff, Sharp et al. 1994) was used for all atoms.

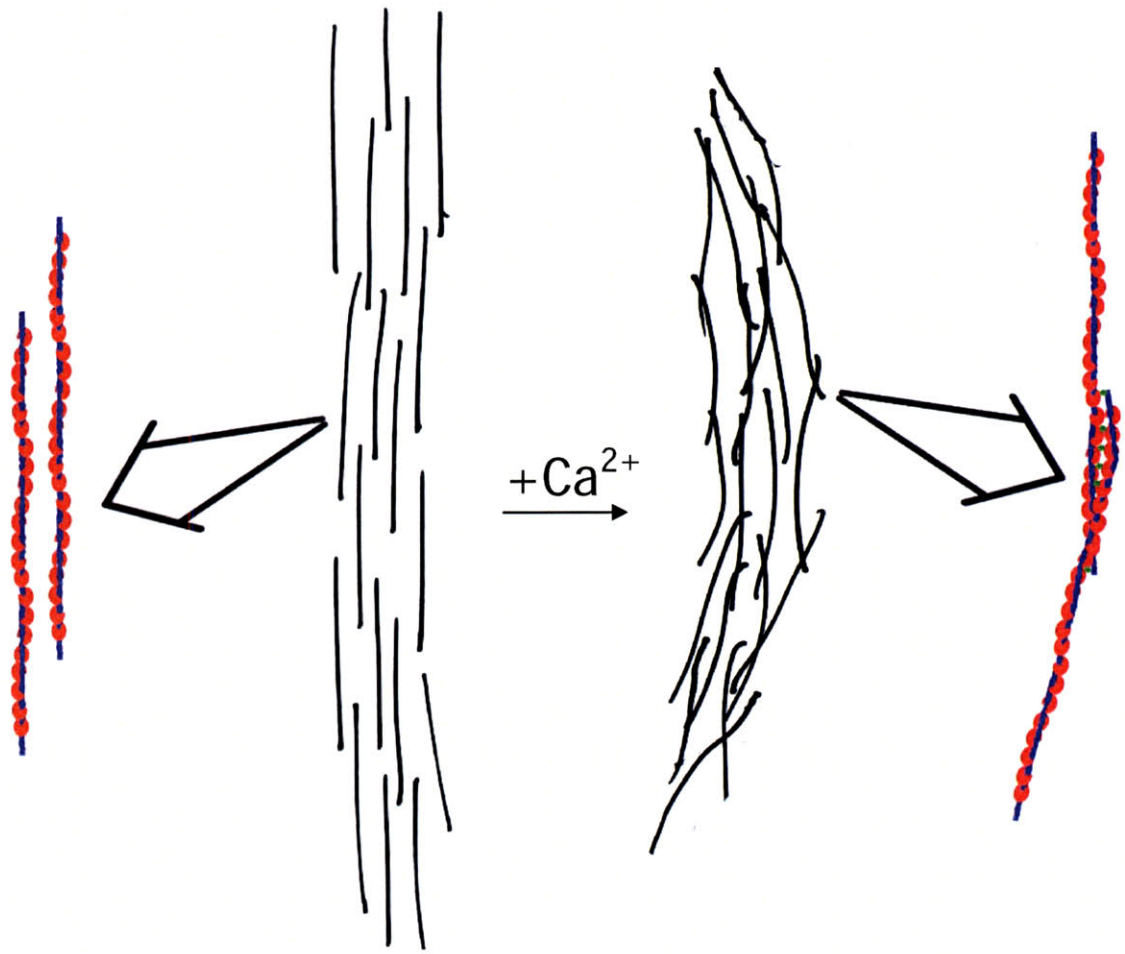

Figure 4.5 Schematic showing proposed molecular interactions within the spasmoneme. Rod-like protein complexes repel each other in the extended state, leading to entropically-driven alignment. The effect of calcium binding is to allow rods to interact with each other. Each rod is made up of a Sfi1p backbone decorated by ~ 20 centrins along its length. In the contracted state, helical associations between centrins on adjacent rods are accommodated by the flexibility of the backbone and scale up to a twisted structure on the microscale. Sfi1p is blue, centrins are red, and some calcium ions are depicted in green.

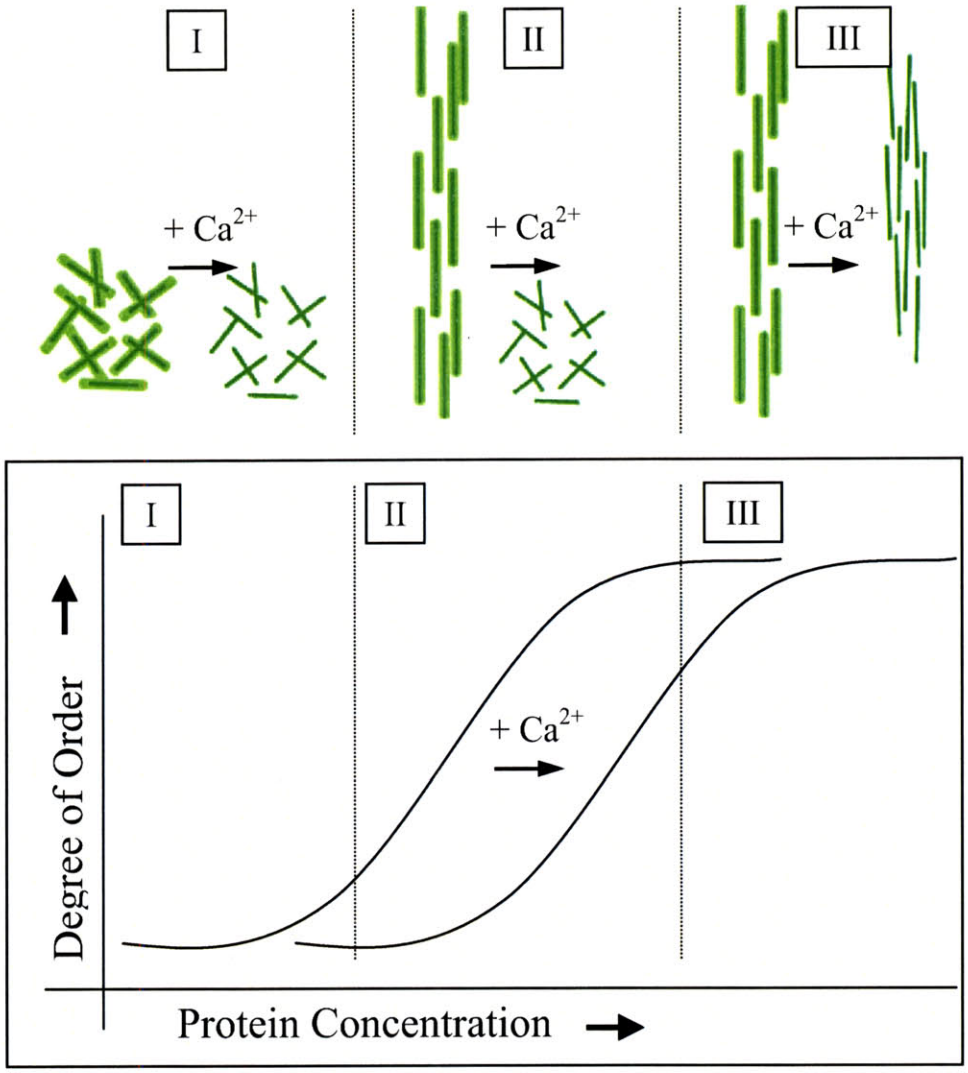

Figure 4.6 Interactions of rod-like protein complexes at various concentrations. Three different regimes of calcium dependent changes in an ordering parameter (such as sample birefringence) may be displayed. In regime I, at low concentrations, proteins are disordered with or without calcium. In regime III, at high concentrations, proteins are ordered with or without calcium. Regime II is an intermediate regime where a significant change in the ordering parameter may be brought about by the addition of calcium.

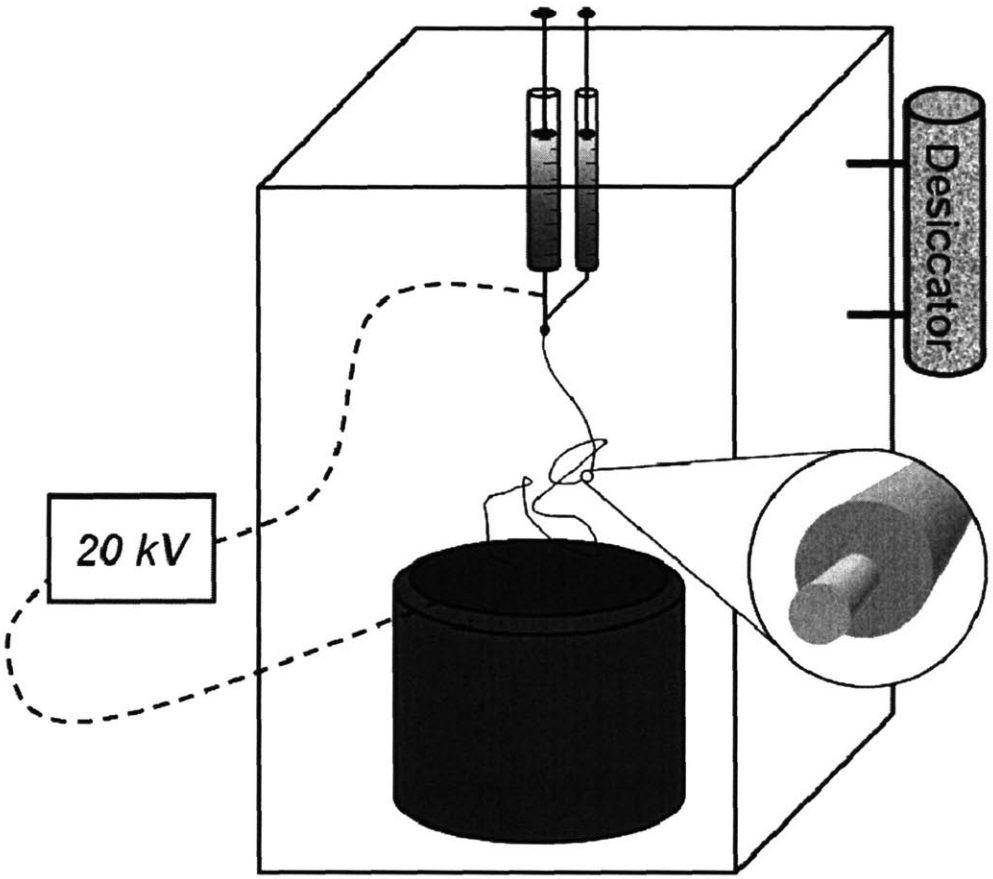

Figure 4.7 Coaxial electrospinning as a method for forming spasmoneme-mimetic actuating fibers. Within a humidity-controlled chamber, two solutions are extruded through the tip of a syringe and across a large voltage gap. Droplets at the tip of the syringe are rapidly elongated by the electric field and deposit as a meshwork of fibers on the anode. Each fiber, on average a few hundred nanometers in diameter, has a coaxial structure (inset). The outer layer can be formed from a spinnable polymer that forms a sheath with suitable pore size to allow diffusion of calcium into the inner core, which consists of contractile proteins in aqueous buffer. Figure courtesy of Jonathan Tejada.

5

Conclusions

5.1. Important parameters for modeling and future work

The multiscale experimental approaches taken in this thesis have converged on a set of structural and mechanochemical characteristics of *Vorticella* motility that have been able to better define the parameters of acceptable models of its molecular mechanism.

At the cellular level, experiments applied two new loading conditions to the contraction of a live cell. The first used centrifugal acceleration to show that cells can overcome more than 200 nanonewtons of force opposing their contraction. The second experiment caused the cells to contract against the restoring force of a flexible micropipette. These pipette-loading experiments defined a maximum stall force for the contractile mechanism of ~ 180 nanonewtons. They also demonstrated that the amount of work performed by the cell during contraction is proportional to the amount by which the stalk is allowed to shorten, with less shortening corresponding to less work.

At the microscale, imaging of the birefringence of live *Vorticella* revealed that microscopically resolvable elements within the spasmoneme are highly ordered in both the extended and contracted state. This piece of evidence alone rules out both rubber-like entropic spring (Moriyama, Okamoto et al. 1999; Mahadevan and Matsudaira 2000) and coiling fiber

(Salisbury 2004) models which have been previously proposed to explain the contractile mechanism. In addition, careful analysis of the images was able to quantify a slight change in ordering which informed the proposal of a new model.

Finally, at the molecular level, it was established that the contractile mechanism is at minimum a two-component system whose components are likely to be homologous to the rod-like centrin-Sfi1p complexes recently discovered in budding yeast. This homology provided new information which could also be used to guide the proposal of a new model for *Vorticella* motility at the molecular level.

The newly proposed model of *Vorticella* motility hinges on the interactions of rod-like protein complexes rather than drastic conformational changes within the complexes. This makes it consistent with the body of evidence discovered through experiments at multiple length scales within this thesis.

Any successful scientific study should uncover more questions than it answers, and this thesis is no exception. The *Vorticella* cell is a complex structure with different mechanical elements playing different roles during contraction. Separation of the components, for example, removal of the spasmoneme from its sheath so that each can be examined independently, should yield new insights into how each component affects contraction. There is also still much to be discovered about the underlying structure through further imaging. With the right preparations, transmission electron microscopy can reach higher resolutions than seen here, and combined with tomographic reconstructions, may be able to reveal more structural details about both the extended and contracted structures. Finally, the molecular level work shown here opens up a large new field of potential investigations. Homology to and important differences from yeast proteins can be better established through further immunofluorescence imaging and biochemistry

work on the spasmoneme proteins. The interactions of such proteins in solution, especially their behavior at different concentrations, will determine the validity of the model proposed here.

5.2. Wider relevance

Vorticella's ultra-fast and powerful motility is a fascinating phenomenon on its own merits, but becomes even more interesting when considered in relation to other centrin-based eukaryotic structures. It appears that the same proteins which generate *Vorticella's* powerful movement exist in fibrous structures that carry out a range of functions in other eukaryotic cells. The flagellar roots of green algae, in which centrin was discovered, contract in response to calcium in order to jettison the flagellum from the algal cell (Salisbury 1984; Salisbury 1998). In budding yeast, the half-bridge of the spindle pole body which forms at the early stages of mitosis and goes on to organize the microtubules which separate chromosomes into daughter cells is made of Sfi1p-centrin fibers. How are these structures related, and how many more exist to carry out other cytoskeletal functions in eukaryotic cells? To what extent do the constituent proteins exploit the same surface properties and intermolecular phenomena which appear to be at play in *Vorticella* contraction? To what extent do completely different proteins use similar structural arrangements to produce movement? These are open questions that promise to reveal fundamental aspects of how cells might use the concept of stored energy to generate movements which require more speed or force than can be attained by the well-known motility mechanisms driven by motor proteins or polymerization.

In fact, the production of high speeds and forces at the micro and nanoscales is something at which biology is often more adept than engineered structures, such as shape-changing polymers.

Through their complex structures, proteins are able to modulate and exploit a variety of intermolecular interactions for various functions, including motility. Hierarchical structures, which are built to high fidelity and exacting standards by biological organisms, are then able to amplify slight changes at the nanoscale into large movements at the microscale. These principles can prove useful if transported to the realm of engineered nanostructures. Actuators based on bio-inspired contractile filaments self-assembled in microscale devices have promise of delivering large, ultra-fast, reversible movements at low power.

A better understanding of *Vorticella* motility, as advanced in this thesis, therefore holds the potential to increase our understanding of the subcellular architectures which produce movements of remarkable speed and power, and how they can be mimicked to fulfill the need for fast microscale actuators in engineered structures.

References

Allen, R. D. (1973). "Structures linking the myonemes, endoplasmic reticulum, and surface membranes in the contractile ciliate Vorticella." J Cell Biol **56**(2): 559-79.

Amersham Biosciences. (2004). GST Gene Fusion System Handbook, Amersham Biosciences. **18-1157-58 Edition AA**.

Amin, A. (1997). Insights into the Secretory Pathway of Stalk Components in *Vorticella convallaria*. Biological Sciences, Graduate College. Chicago, University of Illinois at Chicago: 123.

Amos, W. B. (1971). "Reversible mechanochemical cycle in the contraction of Vorticella." Nature **229**(5280): 127-8.

Amos, W. B. (1972). "Structure and coiling of the stalk in the peritrich ciliates Vorticella and Carchesium." J Cell Sci **10**(1): 95-122.

Amos, W. B. (1975). "Contraction and calcium binding in the vorticella ciliates." Soc Gen Physiol Ser **30**: 411-36.

Amos, W. B., L. M. Routledge, et al. (1975). "Calcium-binding proteins in a vorticellid contractile organelle." J Cell Sci **19**(1): 203-13.

Asai, H., T. Ochiai, et al. (1978). "Improved preparation and cooperative calcium contraction of glycerinated Vorticella." J Biochem (Tokyo) **83**(3): 795-8.

Blum, J. J. and E. Felauer (1959). "Polyelectrolyte Behavior of Glycerol-Treated Psoas Fibers." J Polymer Sci **XLI**: 487-494.

Buhse, H. E., Jr. and J. C. Clamp (2001). Vorticella. Nature Encylopedia of Life Sciences.

Connolly, M. L. (1983). "Solvent-Accessible Surfaces of Proteins and Nucleic Acids." Science **221**: 709 - 713.

Crooks, G. E., G. Hon, et al. (2004). "WebLogo: a sequence logo generator." Genome Res **14**: 1188-1190.

Csank, C., F. M. Taylor, et al. (1990). "Nuclear pre-mRNA introns: analysis and comparison of intron sequences from Tetrahymena thermophila and other eukaryotes." Nucleic Acids Res **18**(17): 5133-41.

David, C. and B. Vigues (1994). "Calmyonemin: a 23 kDa analogue of algal centrin occurring in contractile myonemes of Eudiplodinium maggii (ciliate)." Cell Motil Cytoskeleton **27**(2): 169-79.

Diehl, M. R., K. Zhang, et al. (2006). "Engineering Cooperativity in Biomotor-Protein Assemblies." Science **311**(5766): 1468-1471.

Durussel, I., Y. Blouquit, et al. (2000). "Cation- and peptide-binding properties of human centrin 2." FEBS Lett **472**(2-3): 208-12.

Dzenis, Y. (2004). "MATERIAL SCIENCE: Spinning Continuous Fibers for Nanotechnology." Science **304**(5679): 1917-1919.

Elvin, C. M., A. G. Carr, et al. (2005). "Synthesis and properties of crosslinked recombinant pro-resilin." **437**(7051): 999-1002.

EMBOSS Sixpack. http://www.hgmp.mrc.ac.uk/Software/EMBOSS/Apps/sixpack.html

Fancy, D. A. and T. Kodadek (1999). "Chemistry for the analysis of protein-protein interactions: Rapid and efficient cross-linking triggered by long wavelength light." PNAS **96**(11): 6020-6024.

Febvre, J. (1981). "The myoneme of the Acantharia (Protozoa): A new model of cellular motility." Biosystems **14**(3-4): 327-36.

Frangopol, P. T. and D. Mihailescu (2001). "Interactions of some local anesthetics and alcohols with membranes." Colloids and Surfaces B: Biointerfaces **22**: 3-22.

Frey-Wyssling, A. (1953). Submicroscopic Morphology of Protoplasm. New York, Elsevier Publishing Company.

Gardel, M. L., J. H. Shin, et al. (2004). "Elastic Behavior of Cross-Linked and Bundled Actin Networks." Science **304**(5675): 1301-1305.

Gilson, M. K., K. A. Sharp, et al. (1988). "Calculating the Electrostatic Potential of Molecules in Solution: Method and Error Assessment." J Comput Chem **9**: 327 - 335.

Gouin, E., M. D. Welch, et al. (2005). "Actin-based motility of intracellular pathogens." Current Opinion in Microbiology **8**(1): 35-45.

Grafix Plastics (2004) "Dura-Lar: Oriented Polyester Film." Accessed April 28, 2007. http://www.grafixplastics.com/downloads/mylar_duralar.pdf

Guerra, C., Y. Wada, et al. (2003). "Cloning, localization, and axonemal function of *Tetrahymena* centrin." Molecular Biology of the Cell **14**: 251-61.

Hoffmann-Berling, H. (1953). "The water glycerin extracted cell as model of cell motility." Biochim Biophys Acta **10**(4): 628.

Howard, J. (2001). Mechanics of Motor Proteins and the Cytoskeleton. Sunderland, MA, Sinauer Associates, Inc.

Huang, B. and D. R. Pitelka (1973). "The contractile process in the ciliate, Stentor coeruleus. I. The role of microtubules and filaments." J Cell Biol **57**(3): 704-28.

Hyde, W. L. and S. Inoué (1956). Polarizing Optical Systems. USPTO. **2936673**.

Inoué, S. (1960). "Birefringence in Dividing Cells."

Inoué, S. (1986). "An Introduction to Biological Polarization Microscopy." Video Microscopy: 477-510.

Inoué, S., M. Goda, et al. (2001). "Centrifuge polarizing microscope. II. Sample biological applications." Journal of Microscopy **201**(3): 357-367.

Inoué, S. and W. L. Hyde (1957). "Studies on depolarization of light at microscope lens surfaces. II. The simultaneous realization of high resolution and high sensitivity with the polarizing microscope." J. Cell Biol. **3**(6): 831-844.

Inoué, S., R. A. Knudson, et al. (2001). "Centrifuge polarizing microscope. I. Rationale, design and instrument performance." Journal of Microscopy **201**(3): 341-356.

Institute, S. Pfam: Protein Families Database of alignments and HMMs. UK, Sanger Institute.

Israelachvili, J. (1992). Intermolecular and Surface Forces. San Diego, CA, Academic Press.

Jiang, H., Y. Hu, et al. (2005). "A facile technique to prepare biodegradable coaxial electrospun nanofibers for controlled release of bioactive agents." Journal of Controlled Release **108**(2-3): 237-243.

Karakozova, M., M. Kozak, et al. (2006). "Arginylation of {beta}-Actin Regulates Actin Cytoskeleton and Cell Motility." Science **313**(5784): 192-196.

Katoh, K. and M. Kikuyama (1997). "An all-or-nothing rise in cytosolic [Ca^{2+}] in *Vorticella Sp.*" J Exp Biol **200**(Pt 1): 35-40.

Katoh, K. and Y. Naitoh (1992). "A Mechanosensory Mechanism for Evoking Cellular Contraction in Vorticella." J Exp Biol **168**(1): 253-267.

Katoh, K. and Y. Naitoh (1994). "Control of Cellular Contraction by Calcium in Vorticella." J Exp Biol **189**(1): 163-77.

Keizer, J., G. D. Smith, et al. (1998). "Saltatory Propagation of Ca2+ Waves by Ca2+ Sparks." Biophys J **75**(2): 595-600.

Kilmartin, J. V. (2003). "Sfi1p has conserved centrin-binding sites and an essential function in budding yeast spindle pole body duplication." J Cell Biol **162**(7): 1211-21.

Kojima, H., A. Ishijima, et al. (1994). "Direct Measurement of Stiffness of Single Actin Filaments with and Without Tropomyosin by in vitro Nanomanipulation." Proc Natl Acad Sci **91**(26): 12962-12966.

Kono, R.-I., T. Ochiai, et al. (1997). "Chemical modification of amino acid residues in glycerinated *Vorticella* stalk and Ca^{2+}-induced contractility." Cell Motil Cytoskeleton **36**(4): 305-312.

Kuroda, Y., M. Ogawa, et al. (1996). "Locations of local anesthetic dibucaine in model membranes and the interaction between dibucaine and a Na+ channel inactivation gate peptide as studied by 2H- and 1H-NMR spectroscopies." Biophys J **71**(3): 1191-1207.

Li, S., A. M. Sandercock, et al. (2006). "Structural role of Sfi1p-centrin filaments in budding yeast spindle pole body duplication." J Cell Biol **173**(6): 867-877.

Lodish, H., A. Berk, et al. (2004). Molecular Cell Biology, W. H. Freeman.

Maciejewski, J. J., E. J. Vacchiano, et al. (1999). "Cloning and expression of a cDNA encoding a Vorticella convallaria spasmin: an EF-hand calcium-binding protein." J Eukaryot Microbiol **46**(2): 165-73.

Mackinnon, D. and R. Hawes (1961). An Introduction to the Study of Protozoa. Oxford, Clarendon Press.

MacKintosh, F. C., J. Kas, et al. (1995). "Elasticity of semiflexible biopolymer networks." Physical Review Letters **75**(24): 4425-4428.

Mahadevan, L. and P. Matsudaira (2000). "Motility powered by supramolecular springs and ratchets." Science **288**(5463): 95-100.

Marchant, J. and I. Parker (2000). "Functional Interactions in Ca^{2+} Signaling over Different Time and Distance Scales." J Gen Physiol **116**: 691-695.

Marenduzzo, D., K. Finan, et al. (2006). "The depletion attraction: an underappreciated force driving cellular organization." J Cell Biol **175**(5): 681-686.

Martinez-Sanz, J., A. Yang, et al. (2006). "Binding of human centrin 2 to the centrosomal protein hSfi1." FEBS Journal **273**: 4504-4515.

Matsudaira, P., E. Mandelkow, et al. (1983). "Role of fimbrin and villin in determining the interfilament distances of actin bundles." Nature **301**: 209-214.

McCutcheon, S. and H. E. Buhse, Jr. (2005). Personal Communication. P. Matsudaira, D. Cook and V. Baru. Cambridge, MA.

Mondal, M. and A. Chakrabarti (1992). "The tertiary amine local anesthetic dibucaine binds to the membrane skeletal protein spectrin." FEBS Letters **532**: 396-400.

Moriyama, Y., S. Hiyama, et al. (1998). "High-speed video cinematographic demonstration of stalk and zooid contraction of Vorticella convallaria." Biophys J **74**(1): 487-91.

Moriyama, Y., H. Okamoto, et al. (1999). "Rubber-like elasticity and volume changes in the isolated spasmoneme of giant Zoothamnium sp. under Ca2+-induced contraction." Biophys J **76**(2): 993-1000.

Moriyama, Y., K. Yasuda, et al. (1996). "Ca(2+)-induced tension development in the stalks of glycerinated Vorticella convallaria." Cell Motil Cytoskeleton **34**(4): 271-8.

NCBI BLAST. http://www.ncbi.nlm.nih.gov/blast/

Nicholls, A. (2007). GRASP: Graphical Representation and Analysis of Structural Properties. New York, Columbia University.

Nicholls, A., K. A. Sharp, et al. (1991). "Protein Folding and Association: Insights From the Interfacial and Thermodynamic Properties of Hydrocarbons." Proteins: Struc., Func., and Genet. **11**: 281 - 296.

Ochiai, T., H. Asai, et al. (1979). "Hysteresis of Contraction-Extension Cycle of Glycerinated *Vorticella*." J Protozool **26**(3): 420-425.

Ochiai, T., R. Hara, et al. (1983). "Contraction of the spasmoneme and coiling of the sheath in the glycerinated stalk of Vorticella. ." Cytobios **36**: 95-105.

Ochiai, T., M. Kato, et al. (1988). "Spasmin-like proteins in various ciliates revealed by antibody to purified spasmins of Carchesium polypinum." Experientia **44**(9): 768-71.

Oldenbourg, R. M., G. (1995). "New polarized light microscope with precision universal compensator." Journal of Microscopy **180**(2): 140-147.

Orias, E. (2002). Sequencing the *Tetrahymena thermophila* Genome: A White Paper submitted to the National Human Genome Research Institute. Santa Barbara, CA: 12.

Orias, E., E. P. Hamilton, et al. (1999). *Tetrahymena* as a Laboratory Organism: Useful Strains, Cell Culture, and Cell Line Maintenance. *Tetrahymena thermophila*. D. J. Asai and J. D. Forney. San Diego, Academic Press. **62:** 190-208.

Overbeek, R. (1995). Patscan. Argonne, IL, Argonne National Laboratory.

Papahadjopoulos, D., K. Jacobson, et al. (1975). "Effects of local anesthetics on membrane properties. I. Changes in the fluidity of phospholipid bilayers." Biochim Biophys Acta **394**(4): 504-519.

PBIL PattinProt. Lyon, France, Pole BioInformatique Lyonnais. http://npsa-pbil.ibcp.fr/cgi-bin/npsa_automat.pl?page=/NPSA/npsa_server.html

Poste, G., D. Papahadjopoulos, et al. (1975). "Local Anesthetics Affect Transmembrane Cytoskeletal Control of Mobility and Distribution of Cell Surface Receptors." PNAS **72**: 4430-4434.

Rahat, M., I. Parnas, et al. (1969). "Extensibility and tensile strength of the stalk "muscle" of Carchesium sp." Experimental Cell Research **54**(1): 69-76.

Rasband, W. S. (1997-2006). ImageJ. Bethesda, MD, U.S. National Institutes of Health: http://rsb.info.nih.gov/ij/,.

Routledge, L. M. (1978). "Calcium-binding proteins in the vorticellid spasmoneme." J Cell Biol **77**(2): 358-70.

Routledge, L. M., W. B. Amos, et al. (1975). "Microprobe measurements of calcium binding in the contractile spasmoneme of a vorticellid." J Cell Sci **19**(1): 195-201.

Routledge, L. M., W. B. Amos, et al. (1976). New Calcium-binding Contractile Proteins. Cell Motility. R. Goldman, T. Pollard and J. Rosenbaum. Cold Spring Harbor, Cold Spring Harbor Laboratory. **Book A:** 93-113.

Salisbury, J. L. (1984). "Striated Flagellar Roots: Isolation and Partial Characterization of a Calcium-modulated Contractile Organelle." J Cell Biol **99**: 962-970.

Salisbury, J. L. (1995). "Centrin, centrosomes, and mitotic spindle poles." Curr Opin Cell Biol **7**(1): 39-45.

Salisbury, J. L. (1998). "Roots." J Eukaryot Microbiol **45**(1): 28-32.

Salisbury, J. L. (2004). "Centrosomes: Sfi1p and centrin unravel a structural riddle." Curr Biol **14**(1): R27-9.

Sanner, M. F., A. J. Olson, et al. (1996). "Reduced surface: An efficient way to compute molecular surfaces." Biopolymers **28**: 305 - 320.

Sato, H., G. Ellis, et al. (1975). "Microtubular origin of mitotic spindle form birefringence. Demonstration of the applicability of Wiener's equation." J. Cell Biol. **67**(3): 501-517.

Schiebel, E. and M. Bornens (1995). "In search of a function for centrins." Trends Cell Biol **5**(5): 197-201.

Schumacher, M. A., A. F. Rivard, et al. (2001). "Structure of the gating domain of a Ca2+-activated K+ channel complexed with Ca2+/calmodulin." Nature **410**(6832): 1120-4.

Senecal, K. J., J. W. Soares, et al. (2004). "Novel membrane technology for food and water monitoring." Proc SPIE **5271**: 140 -146.

Senisterra, G. A. and J. R. Lepock (2000). "Thermal destabilization of transmembrane proteins by local anaesthetics." International Journal of Hyperthermia **16**(1): 1-17.

Sharp, K. A. and B. Honig (1990). "Electrostatic Interactions in Macromolecules: Theory and Applications." Ann Rev Biophys Biophys Chem **19**: 301 - 332.

Shin, J. H. (2004). Dynamics and statics of actin assemblies. Mechanical Engineering. Cambridge, MA, Massachusetts Institute of Technology: 101.

Shin, J. H., L. Mahadevan, et al. (2003). "Stored elastic energy powers the 60-{micro}m extension of the Limulus polyphemus sperm actin bundle." J. Cell Biol. **162**(7): 1183-1188.

Shin, J. H., B. K. Tam, et al. (2007). "Force of an Actin Spring." Biophys J **92**(10): 3729-3733.

Shiono, H. and Y. Naitoh (1997). "Cellular contraction precedes membrane depolarization in Vorticella convallaria." J Exp Biol **200**(16): 2249-2261.

Shribak, M. and R. Oldenbourg (2004). Mapping polymer birefringence in 3D using a polarizing microscope with oblique illumination. A. Dario, SPIE. **5462**: 57-67.

Shribak, M. O., R. (2003). "Techniques for Fast and Sensitive Measurements of Two-Dimensional Birefringence Distributions." Applied Optics **42**(16): 3009-3017.

Sitkoff, D., K. A. Sharp, et al. (1994). "Accurate calculation of hydration free energies using macroscopic solvent models." J Phys Chem **98**: 1978 - 1988.

Spencer, M. (1969). "Low-angle x-ray diffraction from concentrated sols of F-actin." Nature **223**: 1361-1362.

Tani, T., R. D. Allen, et al. (2001). "Cellular membranes that undergo cyclic changes in tension: Direct measurement of force generation by an in vitro contractile vacuole of Paramecium multimicronucleatum." J Cell Sci **114**(4): 785-795.

Thompson, et al. (1994). CLUSTAL W.

Thompson, G. A., Jr., L. C. Baugh, et al. (1974). "Nonlethal deciliation of *Tetrahymena* by a local anesthetic and its utility as a tool for studying cilia regeneration." J Cell Biol **61**: 253-257.

TIGR, T. I. f. G. R. (2003). "*Tetrahymena thermophila* Genome, Assembly 10/2003." Retrieved January, 2004, from http://www.tigr.org/tdb/e2k1/ttg/.

Tourbez, M., C. Firanescu, et al. (2004). "Calcium-dependent Self-assembly of Human Centrin 2." J Biol Chem **279**(46): 47672-47680.

Upadhyaya, A., M. Baraban, et al. (2007). "Power-limited contraction dynamics of *Vorticella convallaria*: an ultra-fast biological spring." Biophys J: 1-9.

Vacchiano, E. J., A. Dreisbach, et al. (1992). "Morphogenetic transitions and cytoskeletal elements of the stalked zooid and the telotroch stages in the peritrich ciliate *Vorticella convallaria*." J. Protozool. **39**(11): 101-106.

Vacchiano, E. J., J. L. Kut, et al. (1991). "A novel method for mass-culturing *Vorticella*." J. Protozool. **38**(6): 609-613.

Vale, R. D. and R. A. Milligan (2000). "The Way Things Move: Looking Under the Hood of Molecular Motor Proteins." Science **288**(5463): 88-95.

van der Linden, H. J., S. Herber, et al. (2003). "Stimulus-sensitive hydrogels and their applications in chemical (micro)analysis." The Analyst **128**(4): 325-331.

van Leeuwenhoek, A. (1676). Letter. A. Philos. Trans. R Soc. London Ser. B 12: 133.

Waggoner, B. and A. Van Leeuwenhoek (1996) "Antony van Leeuwenhoek (1632 - 1723)." **Volume**, DOI:

Weis-Fogh, T. and W. B. Amos (1972). "Evidence for a New Mechanism of Cell Motility." Nature **236**(5345): 301-304.

Wibel, R., E. J. Vacchiano, et al. (1997). "The fine structure of the scopula-stalk region of Vorticella convallaria." J Eukaryot Microbiol **44**: 457-466.

Wiech, H., B. M. Geier, et al. (1996). "Characterization of green alga, yeast, and human centrins. Specific subdomain features determine functional diversity." J Biol Chem **271**(37): 22453-61.

Yokoyama, Y. and H. Asai (1987). "Contractility of the spasmoneme in glycerinated *Vorticella* stalk induced by various divalent metal and lanthanide ions." Cell Motil Cytoskeleton **7**: 39-45.

Appendix I

AI.1. Electrospinning: Methods

With the data in mind that hsCen2 will not form fibers on its own, we began investigating its capabilities within fibers formed artificially through a technique called electrospinning. Electrospinning provides a way to form nanometer-scale fibers from a variety of components, including proteins or mixtures of proteins and inorganic polymers, as long as the resulting mixture has the right viscosity and degree of entanglement. The process involves using a large static voltage (~20 kV) to break the surface tension of a drop of soluble polymer/protein material extruded from a syringe, drawing the drop out into a long thin (<1 μm diameter) fiber. The syringe holding the polymeric solution acts as the cathode while a grounded metal surface acts as the cathode. The two are separated by a 10 – 20 centimeter gap. The formed fibers tend to deposit as a fine meshwork on the anode (generally a piece of aluminum foil); a glass slide and/or a carbon substrate were placed on top of the anode so that fibers could be collected for later observation under the light microscope and/or scanning electron microscope. Flow rates, voltages, and distances are given in the Results section. Polymers (mainly poly(ethylene oxide) (PEO) [MW 200,000, Sigma-Aldrich, St. Louis, MO]) were dissolved from powders overnight in buffer and then combined with protein just before spinning. We spun various combinations of hsCen2, cross-linked and not, and labeled with fluorescein-5-isothiocyanate (FITC 'Isomer I') dye [Invitrogen Corp., Carlsbad, CA] together with PEO. If fibers were formed, we then exposed them to 1-2 mM Ca^{2+} in

aqueous solution and observed any morphological changes with light and fluorescence microscopy.

Covalent cross-linking of hsCen2 was done following the protocol of Fancy and Kodadek (Fancy and Kodadek 1999; Elvin, Carr et al. 2005), which uses a photolysis of the ruthenium(II) tris-bipyridyl dication ($Ru(II)bpy_3^{2+}$) along with ammonium persulfate (APS; $S_20_8^{2-}$) to induce covalent linkages between protein residues. Reactants were added to solutions of purified hsCen2 and exposed to a 350 W halogen lamp for 30 – 180 seconds. The products were then visualized by TEM, as described above, or used in electrospinning experiments.

AI.2. Results

Fibers were formed from a mix of protein and polymer (poly-(ethylene oxide): PEO) via the electrospinning technique. We have spun various combinations of hsCen2 and polymers, as seen in the table below. We have also employed a photo-crosslinking technique which targets tyrosine residues. Since the hsCen2 sequence has one tyrosine near the C-terminal, and since the protein prefers to dimerize in solution (Durussel, Blouquit et al. 2000), it was hoped that the two tyrosines per dimer would each link to a tyrosine on another centrin dimer, thereby linking centrins end-to-end into long fibers. While the cross-linking does pull centrins into larger structures, they do not appear to be fibrous under TEM (Figure 13).

All combinations of protein and polymer shown in the table were able to form fibers. HsCen2 was not able to spin into fibers on its own without a polymeric matrix. It is notable that this spinning was accomplished without some of the harsh solvents normally

used to encourage electrospinning (ethanol, etc), so that the proteins are much more likely to be maintain their native activity. However, none of the electrospun fibers have exhibited contractile capabilities in the presence of calcium.

Centrin in electrospun fibers: **Figure AI.1**

Table AI.1 Components and conditions that produced electrospun fibers.

Protein	[mg/mL]	Modifications	Polymer	[%]	Solvent	Fibers
-	-	-	PEO	20%	PBS	yes
Stalks	-	0.1% saponin, 45 min	PEO	7%	50/50% RB/PBS	yes
hsCen2*	112	-	PEO	20%	PBS	yes
hsCen2*	112	-	PEO	20%	PBS	yes
hsCen2*	84	-	PEO	15%	PBS	yes
hsCen2*	84	10 mM Ca2+	PEO	15%	PBS	yes
GST-hsCen2*	53	Ru + APS + 30s light	PEO	7%	PBS	yes
GST-hsCen2*	53	-	PEO	7%	PBS	yes
hsCen2	55	-	-	-	PBS	no
hsCen2	55	Ru + APS + 30s light	-	-	PBS	no
*hsCen2-GST is FITC-labeled						
Operating conditions: 0.1-0.6 mL/h flow rate, 15-25 kV over 13 cm, 35% humidity						

It may be possible in future experiments to explore centrin's movement capabilities with a number of different fibrous scaffolds, especially if centrin is intelligently coupled to the fibrous backbone. Current candidates are the native fibrous protein, discussed in the next section of this chapter, an engineered backbone protein, or a covalently-linked artificial polymer like PEO. David Tirrell's group at Caltech has some experience with engineering scaffold proteins in order to link motor proteins into organized structures

(e.g., kinesins were linked to a backbone of alternating leucine zippers and elastin domains). The benefits of engineering a backbone in such a manner include precise control of molecular arrangement, as well as the possibility to use proteins with well-characterized mechanical properties (e.g., elastin) (Diehl, Zhang et al. 2006). Finally, it is possible that an artificial polymer backbone may still prove useful, if more direct control of its interaction with spasmin is employed. Covalent linkages of antibodies and anti-microbial peptides to polymeric backbones in electrospun fibers have been achieved by researchers at the Natick Army Soldier Center (Senecal, Mello et al. 2004).

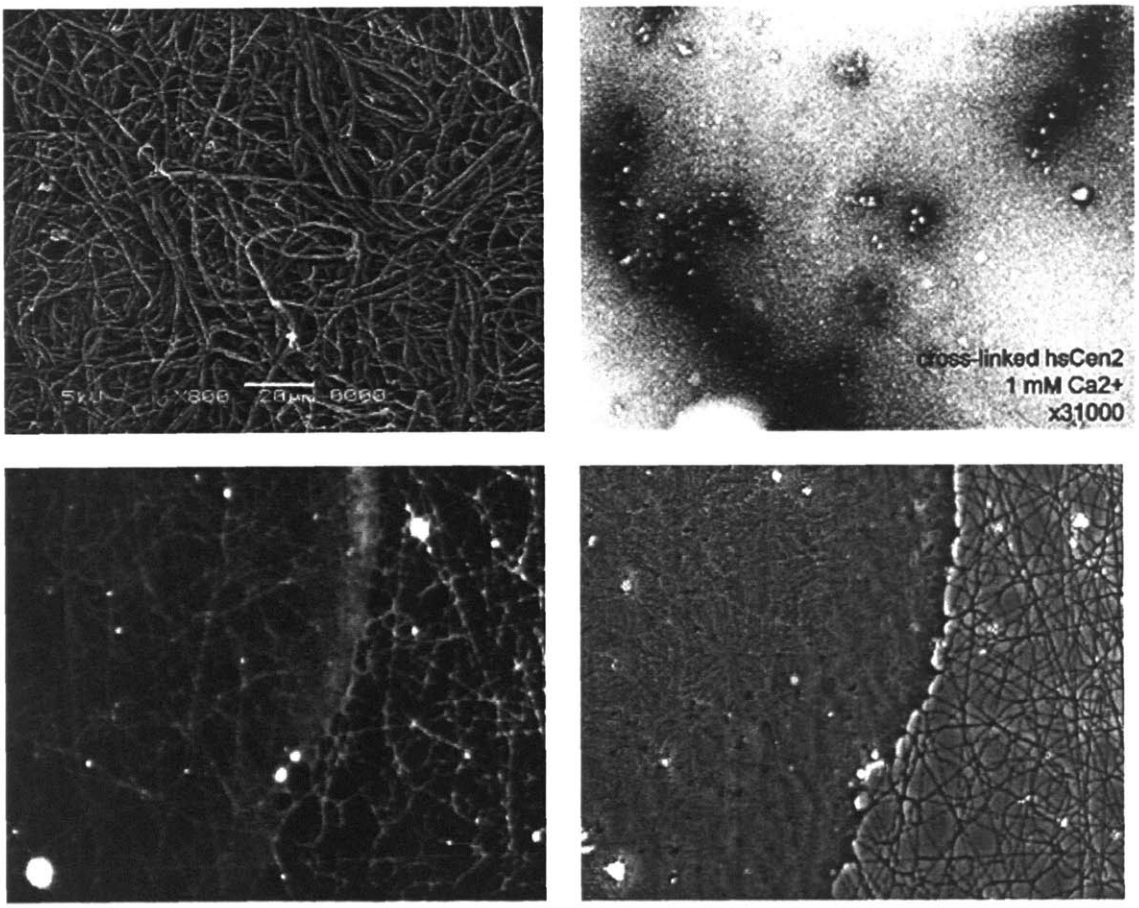

Figure AI.1 **(top left)** 20% PEO in PBS electrospun and visualized at 800X by scanning electron microscopy. **(top right)** Cross-linked hsCen2 plus 1 mM Ca^{2+} visualized at 31000X by transmission electron microscopy. **(bottom)** Cross-linked, FITC-labelled hsCen2 plus 7% PEO in PBS electrospun and visualized at 10X by light microscopy (bottom left: fluorescence; bottom right: phase). A drop of 1 mM Ca^{2+} in 80/20% EtOH/PBS was added to the left side of each image. The calcium does not cause any morphological changes in the fibers at this scale.

Appendix II

AII.1. Discovered Sfi1p homolog sequences in *Tetrahymena thermophila*

TIGR8255564 introns repeats peptide for antibody synthesis

```
                    M  Y  D  D  A  I  T  F  F  Q  K  A  V  Q  L  D    F3
  1 TTATGATAAAAAAAATGTATGATGATGCTATTACATTCTTCTAGAAGGCTGTTTAACTTG 60

    P  K  D  S  W  A  F  G  N  L  G  Y  S  F  M  Q  K  E  M  Y    F3
 61 ATCCTAAAGACAGCTGGGCATTTGGAAACCTGGGATATTCATTTATGCAAAAAGAAATGT 120

    D  D  A  I  T  F  F  Q  K  A  V  Q  L  D  P  R  D  S  W  A    F3
121 ATGATGATGCTATTACATTCTTCTAGAAGGCTGTTTAACTTGATCCTAGAGACAGCTGGG 180

    F  G  N  L  G  Y  S  F  M  K  K  K  M  Y  D  D  A  I  T  F    F3
181 CATTTGGAAATCTGGGATATTCATTTATGAAAAAAAAAATGTATGATGATGCTATTACAT 240

    L  Q  K  A  V  Q  L  D  P  K  D  S  W  A  F  G  N  L  G  Y    F3
241 TCTTGTAGAAGGCTGTTTAACTTGATCCTAAAGACAGCTGGGCATTTGGAAATCTGGGAT 300

    S  F  M  I  K  K  M  Y  D  D  A  I  T  F  F  Q  K  A  V  Q    F3
301 ATTCATTTATGATAAAAAAAATGTATGATGATGCTATTACATTCTTCTAGAAGGCTGTTT 360

    L  D  P  K  D  S  C  A  F  R  C  M  G  Y  S  F  M  K  K  E    F3
361 AACTTGATCCTAAAGACAGCTGCGCATTTAGATGTATGGGATATTCATTTATGAAAAAAG 420

    M  Y  D  D  A  I  T  F  F  Q  K  A  V  Q  L  D  P  R  D  S    F3
421 AAATGTATGATGATGCTATTACATTCTTCTAGAAGGCTGTTTAACTTGATCCTAGAGACA 480

    W  A  F  G  N  L  G  Y  S  F  M  K  K  K  M  Y  D  D  A  I    F3
481 GCTGGGCATTTGGAAATCTGGGATATTCATTTATGAAAAAAAAAATGTATGATGATGCTA 540

    T  F  F  Q  K  A  V  Q  L  D  P  K  D  S  W  A  F  G  N  L    F3
541 TTACATTCTTCTAGAAGGCTGTTTAACTTGATCCTAAAGACAGCTGGGCATTTGGAAATC 600

    G  Y  S  F  M  K  K  K  M  Y  D  D  A  I  T  F  F  Q  K  A    F3
601 TGGGATATTCATTTATGAAAAAAAAAATGTATGATGATGCTATTACATTCTTCTAGAAGG 660

    V  Q  L  D  P  K  D  S  W  A  F  G  K  L  G  Y  S  F  M  Q    F3
661 CTGTTTAACTTGATCCTAAAGACAGCTGGGCATTTGGAAAGCTGGGATATTCATTTATGC 720

    K  Q  M  Y  D  D  A  I  T  F  F  Q  K  A  V  Q  L  D  P  K    F3
721 AAAAATAAATGTATGATGATGCTATTACATTCTTCTAGAAGGCTGTTTAACTTGATCCTA 780

    D  S  W  A  F  G  K  L  G  Y  S  F  M  Q  K  E  M  Y  D  D    F3
781 AAGACAGCTGGGCATTTGGAAAGCTGGGATATTCATTTATGCAAAAAGAAATGTATGATG 840
```

```
      A  I  T  F  S  Q  K  A  V  Q  L  D  P  D                    F3
 841 ATGCTATTACATTCTCCTAGAAGGCTGTTTAACTTGATCCTGATGTTAAAGAAAATCTTT 900

             E  Q  H  F  K  K  K  E  G  I  N  I  Q                F3
 901 TAAATCTAGGAATAGCATTTTAAAAAAAAGGAAGGTATCAACATTCAAGTATATATTTCA 960

      K  C  I  Q  I  D  P  K  L  K  D  C  H  L  Y  L  S  V  D  F   F3
 961 AGAAATGTATATAAATTGATCCAAAACTTAAGGATTGCCATTTATACCTTTCTGTTGATT 1020

      Q  L                                          F  T  T  Q     F3
1021 TTTAGTGTAAAAAAATGTACAAACATGCAATTATATCATTAAAAAAGTGTTTACAACTTA 1080

      S  L  *                                                     F3
1081 ATCCTTATGATAACTATAAACAATAATT                                 1108
```

The final best guess at the protein sequence is shown below, after removing the three most likely introns (18.75%, 19.23%, 18.75%) to create a frameshift with a reasonably placed stop codon:

```
MYDDAITFFQKAVQLDPKDSWAFGNLGYSFMQKE
MYDDAITFFQKAVQLDPRDSWAFGNLGYSFMKKK
MYDDAITFLQKAVQLDPKDSWAFGNLGYSFMIKK
MYDDAITFFQKAVQLDPKDSCAFRCMGYSFMKKE
MYDDAITFFQKAVQLDPRDSWAFGNLGYSFMKKK
MYDDAITFFQKAVQLDPKDSWAFGNLGYSFMKKK
MYDDAITFFQKAVQLDPKDSWAFGKLGYSFMQKQ
MYDDAITFFQKAVQLDPKDSWAFGKLGYSFMQKE
MYDDAITFSQKAVQLDPDEQHFKKKEGINIQKCIQIDPKLKDCHLYLSVDFQLFTTQSL*
purple is C terminus after intron

consensus sequence: MYDDAITFFQKAVQLDPKDSWAFGNLGYSFMKKK
                            L        R  C  RKM     Q E
                                            C      I Q
```

Secondary structure prediction *(H = helix, E = strand, - = no prediction)*

(http://www.cmpharm.ucsf.edu/cgi-bin/nnpredict.pl):

```
----HHHHHHHH---------EE------HH-H-
MYDDAITFFQKAVQLDPKDSWAFGNLGYSFMQKE
---HHHHHHHHH---------------HHHH---
MYDDAITFFQKAVQLDPRDSWAFGNLGYSFMKKK
---HHHHHHHHH---------EE------EHHH-
MYDDAITFLQKAVQLDPKDSWAFGNLGYSFMIKK
---HHHHHHHHH----------EH-H--------
MYDDAITFFQKAVQLDPKDSCAFRCMGYSFMKKE
---HHHHHHHHH---------------HHHH---
MYDDAITFFQKAVQLDPRDSWAFGNLGYSFMKKK
----HHHHHHHH---------EE----HHHH---
MYDDAITFFQKAVQLDPKDSWAFGNLGYSFMKKK
----HHHHHHHH---------HHH----HHH---
MYDDAITFFQKAVQLDPKDSWAFGKLGYSFMQKQ
----HHHHHHHH---------HHH-----HH-H-
MYDDAITFFQKAVQLDPKDSWAFGKLGYSFMQKE
----HHHHHH---------HH--------HE-------------HEE----EEE-----
MYDDAITFSQKAVQLDPDEQHFKKKEGINIQKCIQIDPKLKDCHLYLSVDFQLFTTQSL*
```

The two additional sequences shown below were found, but not used for antibody production.

TIGR8254638

SQQKMISKHSQAFEQLGYL
FNKKEMYDNDAITLIQKADQLDPKDSWEGLSFLKEMQQSL
SLAFGKLGFL
FQKKQMYDDAIKFYQKAFQIDPKNSWAFGKLGYL
FYKKEMYDHAIPFFQKGCLTTQVQLGLS
FLKKEMHAVQLEHKYSWDYH
FKKKCMDDAITFFQKALQIDPKDSWAFRNLGYS
FMKKEIFDDIITFLEIWDIHLKKKFLMI
LLHSFQKAVQLDHKSSWAFGQLGYSRRLFNLIIKAAGHLD
SWILFYKKRNVCHSILLEGCLY
FIKKEMYDDAIPFFQKVVQLDPKNRWAFRNMGNS
FLKKKMYDDAITFFSNTVQLDRTTRTFEQLGLS
ILKKQMYDDAITHLNSWD
YLFKNKCMMMLLFLQKAIQIDPKNSWAF
NLGSQQRMNSKDSQEFGELGYLF
QEKDDHDDDAITLLQETVQLDPKDSQAFRQLGYQ
FLKKQMYDDAITLFQKAIQLDDKDSWAFGKLGYS
FLKKKMYDDAITFFQKAIQLNDKDSWAFGKLGYS
FLKKKMYDDAFTFFQKAAQLDPQDSSAFANLGYL
FYKKEMYDDAITFFQKAVQLDPKCSWAFGRMGYV
FLKREMNDDAISFFQKSVQLDPKDSWAFGQLGYL
FLKKEMYDYAIKFLKKAVQLNPKDSQALGKLGYT
FLKKQMYDYAIKFLKKTVLLYPKDSWALGKLGYS
FLKKEMYDDAITFFQKSIQLNDKDSWAFGKLGYS
FLKKQMYDDAITFFQKAIQLNDKDSWAFGKLGYS
FLKKEMYDDAITFLQKAAQLDPKDSLAFANLGYS
FMKKEMYDDAIKFFQKAVQLDPKCSWAFGRMGYV
FLKKEMNDAAITFFQKTVQLDPKDSWAFEQLGYL
FLQKEMYDYAIKFLKKAVQLDPKVSNAPLNLRMA
FYKKRRYQHSIIYFKKCIQIDPKVMVNHFNLSLD
FEFKKIYKHAIKSSKEGLKNNPQDSKTLQLQKSLKSQI
(4920 intervening bases)
QSKNGEIFQIRARTKQVYGQQYVIQPKNKIINNTCHFGIY
QVMCQFQIMVFYILDIKFQLCHQLRIQYLQLMAQKKISIF
YIHLYSVLLFLLVKSYQIIGK
IYQYQKNDSAIQFYQKVVQLDPKNSWAFKLGF
SFLKRMYDEAIIFFQMAIQLDPKDSWAFGQLGYL
FNEKKKCMKMPLNPYKRLLAVQLDSKTAWHLYSWDIH
FRKKQMFDDGIIFFQNAIQLDPNSRAFGELGFS
FQKKEIYDDSITFQKKAVQIDPKYRWAFGQLDIYLMKKKV

TIGR8254580

Q*LLSKLSRQFQQKYNDYPN
LQLCKKLSIIAHKYMKKCQF
DVSLYLHCDKLKPDIQICKK
FYISSHQYRGKKQ
FAIGLNLLNEKVDPDLQVAKQSFTIADDYMEKQM
FSYGLKGFAWSDKPDLQVAKQFFTIADDYMKKLM
FSYGLNGFAWSDKPDLQVAKQLFTIADDYMKKKM
FSYGLNGFAWSDRPDLQVAKQFFTIADDYMEKQM
FSYGLNGFAWSDKPDLQVAKQFFTIADDYMKKIM
FSYGLNGFAWSDKPDLQVAKQFFTIADDYMQKQM
FSYGLKGFAWSDKPDLQVAKQFFTIADDYMQKQM
FSYGLKGFAWSDKPDLQVAKQLFTIADDYMQKQM
FSYGLRGFAYSDKPDLQVAKQFFTIADDYMKKKM
FSYGMCRFACSDKPDLQVAKQFFTIADDYMQKQM
FSYGLKGFAWSDKPDLQVAKQFFTIADDYRKKIM
FSYGLKGFAWSDKPDLQVAKQFFTIADDYMEKKM
FSYGLNGFAYSNKPDLQVAKQFYYVADDYKLSLQSRDGL
(1921 intervening bases)
EYIKS*NLYREQFIYKFTSVKRKKW
FAIGLNLLNEKVDPDLQVAKQIFTIADDYMEKKT
FSYGLKGFAWSDKPDLQVAKQFFTIADDYMEKKM
FSYGMNGFTWSDKPDLQVAKQFFTIADDYMEKQM
FSYGMNGFTWSDKPDLQVAKQFFTIADDYMEKKM
FSYGLKRFAWRYKPDLQVAKQFFTIADDYMEKKM
FSYGLQGFAYSNKPDLQVVQQFYYVADDYKSSQQ
LIDGLIQYWKSKLTNFFENKISIFNQYYILIQTDFYYNFQ
QFFKTYQYNIYYICSIIFKNLLYIHAIFITP
SPILQI*IIKQLNLFK*